Trim Optimization for an Aircraft with Distributed Electric Propulsion and a Tail Thrust Unit

Guilherme Fernandes Lourenço

Trim Optimization for an Aircraft with Distributed Electric Propulsion and a Tail Thrust Unit

by

Guilherme Fernandes Lourenço

to obtain the degree of Master of Science
at the Delft University of Technology,
to be defended publicly on Wednesday April 22, 2026 at 14:30.

Thesis committee:

	Dr. F. (Fabrizio) Oliviero,	TU Delft, chairperson
	Dr. C. (Carmine) Varriale,	TU Delft, supervisor
	Dr. ir. P. (Pieter-Jan) Proesmans,	TU Delft, external examiner

Place:	TU Delft Faculty of Aerospace Engineering, Delft
Project duration:	April 28, 2025 – April 22, 2026
Student number:	5964121

Cover: Lockheed C-130H Hercules by Paul Nelhams, CC BY-SA 2.0
Style: TU Delft Report Style, modified by Carmine Varriale

TU Delft

Preface

This thesis represents a pivotal moment in my academic journey that started at Instituto Superior Técnico, where I found my fascination for aircraft, and that led me to TU Delft, where I learned what being in the forefront of aviation innovation is really like.

Often times, bringing forth new knowledge that is useful to the engineering community felt like a daunting and solitary task, so I would like to thank my supervisor, Carmine Varriale, for always being available to brainstorm new paths forward when progress came to a standstill and for keeping my hopes up when everything seemed lost. His guidance was essential for this project and I walk away with lessons that will be very useful in my future career.

I want to thank my mother, for all the unconditional support, thoughtful advice and reassurance during the adventure that has been pursuing my master's degree so far away from home, and my father, for sparking my interest in engineering from a young age.

Finally, thank you to all the friends I made in Lisbon and Delft, without whom this university experience wouldn't have been the same. Even though we are now all scattered throughout Europe, all the good memories, moments shared and occasional visits motivated me to keep going and provided much needed breaks from the stressful academic environment.

Guilherme Fernandes Lourenço
Delft, April 2026

Abstract

This thesis presents a trim optimization methodology for aircraft featuring distributed electric propulsion (DEP) systems and horizontal thrust units (HTU). The Unifier C7A-HARW, a 19-passenger hybrid-electric commuter aircraft with 12 wing-mounted propellers and a tail-mounted HTU, serves as the reference configuration. Multiple trim solutions with different types of propulsion systems usage and performance indicators, such as maximum range, endurance or lift-to-drag ratio, are explored through optimization, revealing complex relationships between angle of attack, airspeed, flap deflection, ruddervator deflection, required aerodynamic power and electric power consumed in steady level flight. Some unexpected results demonstrate that maintaining a constant low angle of attack and gradually reducing flap deflection as airspeed increases is desirable for lowering aerodynamic power requirements in trim conditions and that the wing tip propeller has an important role under certain circumstances. Empirical correlations between power requirements, angle of attack, airspeed, flap and ruddervator deflections are established, providing insights into the performance characteristics of DEP aircraft configurations and enabling efficient trim performance predictions useful for conceptual design.

Keywords: Distributed Electric Propulsion, Trim Optimization, Aircraft Performance, Flight Mechanics

Contents

Nomenclature

Abbreviations

Abbreviation	Definition
BEM	Blade Element Momentum Theory
BET	Blade Element Theory
CFD	Computational Fluid Dynamics
NASA	National Aeronautics and Space Administration
DEP	Distributed Electric Propulsion
HTU	Horizontal Thrust Unit
STOL	Short Take-Off and Landing
SRV	Swirl Recovery Vane
UBEMT	Unsteady Blade Element Momentum Theory
VLM	Vortex Lattice Method

Symbols

Symbol	Definition	Unit
a	Axial induction factor	[—]
a_t	Tangential induction factor	[—]
B	Control surface effectiveness matrix	[—]
c	Blade section chord length	[m]
$\overline{c_j}$	Aerodynamic mean chord length for wing section j	[m]
c_d	Blade section drag coefficient	[—]
C_{D_0}	Zero lift drag coefficient	[—]
$C_{D,\ airframe}$	Drag coefficient of the airframe	[—]
C_F	Force coefficients	[—]
c_l	Blade section lift coefficient	[—]
$C_{\ell i}$	Section lift coefficient for wing section i	[—]
C_{L_0}	Lift coefficient at angle of attack of 0 deg	[—]
C_{L_α}	Lift curve slope	[1/rad]
$C_{L,\ airframe}$	Lift coefficient of the airframe	[—]
C_m	Pitching moment coefficient	[—]
C_P	Power coefficient	[—]
c_q	Blade section torque coefficient	[—]
C_Q	Torque coefficient	[—]
c_t	Blade section thrust coefficient	[—]
C_T	Thrust coefficient	[—]
D	Drag	[N]
D_p	Propeller diameter	[m]
dA_i	Differential planform area at control point i	[m^2]
$\mathbf{d}\ell_i$	Directed differential vortex length vector	[m]

Symbol	Definition	Unit
F_x, F_y, F_z	Force components in body axes	[N]
G_i	Dimensionless vortex strength for section i	[—]
i_{DEP}	DEP propeller installation angle	[rad]
$I_{xx}, I_{xz}, I_{zz}, I_{yy}$	Moment of inertia tensor components	[kg.m^2]
J	Advance ratio	[—]
L	Lift	[N]
L/D	Lift to drag ratio	[—]
$\dot{m}$	Mass flow rate	[kg/s]
M_x, M_y, M_z	Moment components in body axes	[N.m]
n	Rotational speed	[rev/s]
N, E, D	Aircraft position in the earth reference frame	[m]
p, q, r	Angular velocities in body axes	[rad/s]
$\dot{p}, \dot{q}, \dot{r}$	Angular accelerations in body axes	[rad/s^2]
P_{elect}	Electric power consumed	[W]
$P_{propulsive}$	Propeller propulsive power	[W]
P_{req}	Required aerodynamic power	[W]
P_{shaft}	Propeller shaft power	[W]
p_s	Pressure	[Pa]
Q	Torque	[N.m]
Q_C	Torque coefficient (alternative definition)	[—]
Q_p	Penalty matrix	[—]
R	Correlation coefficient	[—]
R_d	Actuator disk radius	[m]
r_i	Blade section radial station	[m]
$\mathbf{r}_{i_1 j}$	Vector from node i_1 to control j	[—]
$\mathbf{r}_{i_2 j}$	Vector from node i_2 to control j	[—]
$r_{i_1 j}, r_{i_2 j}$	Magnitudes of $\mathbf{r}_{i_1 j}$ and $\mathbf{r}_{i_2 j}$	[m]
R_p	Propeller radius	[m]
R_s	Streamtube section radius	[m]
S	Wing area	[m^2]
S_d	Actuator disk area	[m^2]
T	Thrust	[N]
T_C	Thrust coefficient (alternative definition)	[—]
u, v, w	Translational velocities in body axes	[m/s]
$\dot{u}, \dot{v}, \dot{w}$	Translational accelerations in body axes	[m/s^2]
$\mathbf{u}_\infty$	Unit vector in freestream direction	[—]
V	Airspeed	[m/s]
v_a	Induced axial velocity	[m/s]
V_d	Velocity at the actuator disk	[m/s]
V_e	Airspeed at the streamtube exit	[m/s]
V_{eff}	Effective velocity	[m/s]
V_{Emax}	Maximum endurance airspeed	[m/s]
V_j	Axial velocity in the slipstream jet	[m/s]
V_{LDmax}	Maximum lift to drag ratio airspeed	[m/s]
V_{n_i}	Component of velocity normal to the camberline	[m/s]
V_{rel}	Relative velocity of a propeller blade section	[m/s]
V_{Rmax}	Maximum range airspeed	[m/s]
V_S	Stall airspeed	[m/s]

Symbol	Definition	Unit
V_∞	Freestream velocity magnitude	[m/s]
$\mathbf{V}_\infty$	Freestream velocity vector	[—]
W	Weight	[N]
w_{ij}	Matrix of the vortex induced velocity strengths	[—]
x_a	Axial position	[m]
$\dot{x}_\mathrm{k}$	Accelerations in body axes array	[m/s^2, rad/s^2]
y_s	Spanwise wing position	[m]
α	Angle of attack	[rad]
α_i	Local angle of attack for wing section	[rad]
β	Propeller blade section pitch angle	[rad]
γ	Flight path angle	[rad]
Γ	Circulation	[m^2/s]
Γ_i	Strength of horseshoe vortex i	[m^2/s]
δ_a	Aileron deflection	[rad]
δ_{el}	Elevator deflection	[rad]
δ_f	Flap deflection	[rad]
δ_HTU	HTU propeller activity factor	[—]
δ_r	Ruddervator deflection	[rad]
δ_{rud}	Rudder deflection	[rad]
δ_T	Thrust setting	[—]
δ_{T_i}	DEP propeller activity factor	[—]
ζ_i	Known variables array	[—]
η	Efficiency	[—]
θ_b	Blade section inflow angle	[rad]
λ	Trim controls array	[—]
$\lambda_\mathrm{lb}, \lambda_\mathrm{ub}$	Trim controls lower and upper bounds	[—]
$\boldsymbol{\nu}_{ij}$	Dimensionless velocity induced at point j by vortex i	[—]
$\boldsymbol{\xi}_i$	Dimensionless spanwise length vector	[—]
ρ	Air density	[kg/m^3]
τ	Flap effectiveness	[—]
ϕ, θ, ψ	Euler angles in body axes	[rad]
Ω	Propeller rotation rate	[rad/s]

List of Figures

List of Tables

Part I

Research Definition

1

Introduction

Emerging novel aircraft configurations featuring wing-mounted distributed propulsion are characterized by strongly coupled aero-propulsive phenomena [1–3]. The coupling is due to the interaction between the propeller slipstreams and the flow around the main and secondary lifting surfaces [4, 5]. This interaction entirely determines the flight performance of these aircraft, making its analysis and optimization significantly more challenging [6].

In a blown-lift aircraft configuration, for example, the propulsion system is distributed along the leading edge of the wing in order to take advantage of the accelerated flow over the wing sections behind the engines. This arrangement generates more lift and energizes the boundary layer, allowing for the reduction of the overall wing size without causing earlier stall onset, which is relevant at lower speeds [7, 8].

Identifying the trim states and controls for such a complex system in various flight conditions is not a trivial problem, as the available degrees of freedom are redundant and also coupled. The possibility to use different thrust settings on each propeller increases the number of trim controls, making the trim problem underdetermined [9, 10]. This creates the conditions for multiple trim solutions to exist for the same flight condition, which can be exploited to optimize the aircraft performance [11–13].

Studies show that the maximum effective lift coefficient of a trimmed aircraft during landing is dependent on the available thrust and, therefore, the lift augmentation potential can be limited by the chosen trimming strategy [14]. Also, it has been reported that the elevator effectiveness can be the limiting factor for trimming at low airspeeds and there is available evidence that the coupling between angle of attack and thrust settings of the distributed propulsion system is one of the most impactful couplings to aerodynamic forces [15].

Another study demonstrates that when trim is being constrained by the elevator deflection, using an array of distributed propulsion propellers with different geometric characteristics may allow trimmed flight at lower airspeeds than before [16].

This raises the question on whether it would be possible to improve trimmed aircraft performance by coupling different available propulsion systems on the same aircraft.

This thesis presents a methodology to explore the trim solution space for aircraft with distributed electric propulsion systems and horizontal thrust units, with particular emphasis on low-speed performance. It also provides simplified empirical relations between the required aerodynamic power and trim variables, which could be used for preliminary design and optimization.

The Unifier C7A-HARW is chosen as the reference aircraft to apply the selected methodology and compare the results. It is a 19-passenger hybrid-electric commuter aircraft featuring a distributed electric propulsion system on the main wing and a horizontal thrust unit behind the tail [17–19].

In Chapter 2, a state-of-the-art review of historical uses of distributed propulsion on aircraft, aero-propulsive interactions and the trim problem is provided.

The research questions that this project intends to answer are formulated in Chapter 3 and the scientific article with all the main information, results analysis and conclusions is in Part II.

In Part III, there are some results that weren't included in Part II, but that are still relevant and useful to have a clearer picture of all the work presented.

Finally, in Part IV, additional result graphs are available and a different approach to aero-propulsive modeling is described, along with some data regarding a failed attempt at capturing aero-propulsive interactions in conditions relevant for low airspeed flight.

2

State-of-the-art Review

2.1. Historic uses of distributed propulsion

Leveraging the benefits of aero-propulsive interactions has been of interest in the aircraft industry since the early 1950s, when there was a need for aircraft capable of landing and taking off in short, damaged or unprepared runways [20, 21].

Early research demonstrated that designing an aircraft with low speed capabilities was paramount to achieving the desired short landing properties, while including reverse thrust or increasing the ground roll friction had a lower beneficial impact on performance [22].

On one hand, the minimum flight speed is often limited by the minimum control speed and, therefore, propulsion augmented aerodynamic control would be needed to allow the pilot to steer the aircraft. On the other hand, a high wing loading would be required to reduce gust sensitivity at these low speeds.

One example of an aircraft where these challenges were identified is the Lockheed C-130 Hercules, shown in Figure 2.1, when lower speeds were achievable by increasing the maximum flap deflection and thrust ratio of the baseline aircraft, but at the cost of low roll response, insufficient directional stability and the need for high control surface deflections in trim, which wasn't deemed safe for operation. Therefore, one of the modifications tested was a boundary-layer control system, where auxiliary compressors were driven by the main engines which delivered additional air flow to the control surfaces leading edges through ducts in the wing and from the wing center to the tail [23].

This solved the C-130 Hercules control effectiveness issue at low speeds, but the internally blown flap concept wasn't widely applied given the added complexity of the propulsion system and aircraft structure, so more focus was placed in externally blown configurations.

The Breguet 940 and its successors, the Breguet 941 and Breguet 941S, shown in Figure 2.2, were part of one of the first family of prototype aircraft developed with STOL capabilities in mind, to be operationally tested.

By using the concept of blown lift with the slipstream of its 4 turbo-prop engine propellers engulfing 90% of the wing span, these aircraft ensured high lift coefficients with deflections of up to 98 deg on their inboard double-slotted flaps and 72 deg on the outboard ones, allowing for a stall speed as low as 25 m/s and a landing distance of 260 m feet over 15 m obstacles, for a gross weight of 16300 kg [25].

For reference, an aircraft of similar size and conventional design such as the Fokker F27 Mk 500 has

Figure 2.1: Lockheed C-130 Hercules. [24]

a landing distance of 251 m at a touchdown speed of 54 m/s and gross weight of 18104 kg [26]. Furthermore, the Breguet 941 featured reverse thrust capabilities on all propellers and, on the outboard propellers, differential propeller blade pitch settings to improve roll and yaw performance and zero thrust blade pitch settings for steeper approach angles.

Figure 2.2: Breguet 941S. [27]

Research efforts were also widely applied to the case of aircraft powered by jet engines and different concepts of harnessing the engine's exhaust jet for a supercirculation and deflected jet effect were tested. An overview of the different concepts of powered lift augmentation can be seen in Figure 2.3.

The principle behind these phenomena is the Coanda effect, where, due to the entrainment of fluid from the regions outside the jet, a low pressure region between the jet and the flap surface makes the jet follow the surface's curvature, with a balance between suction and centrifugal forces, while the outer ambient streamlines are also influenced and deflected, resulting in an increase of the jet volume [28].

One of these concepts is the upper-surface blown flap, where the engines are placed on top of the wing in such a way that the flap is immediately behind the engine nozzle, which showed to have similar lift augmentation performance to other concepts such as the externally blown flap, but with a reduced noise footprint, since the wing acts as a barrier to vertical noise propagation [30].

However, it wasn't integrated into an operational aircraft given the thermal management problems generated by the hot, high pressure exhaust jet and the low thrust-to-weight ratios of the engines.

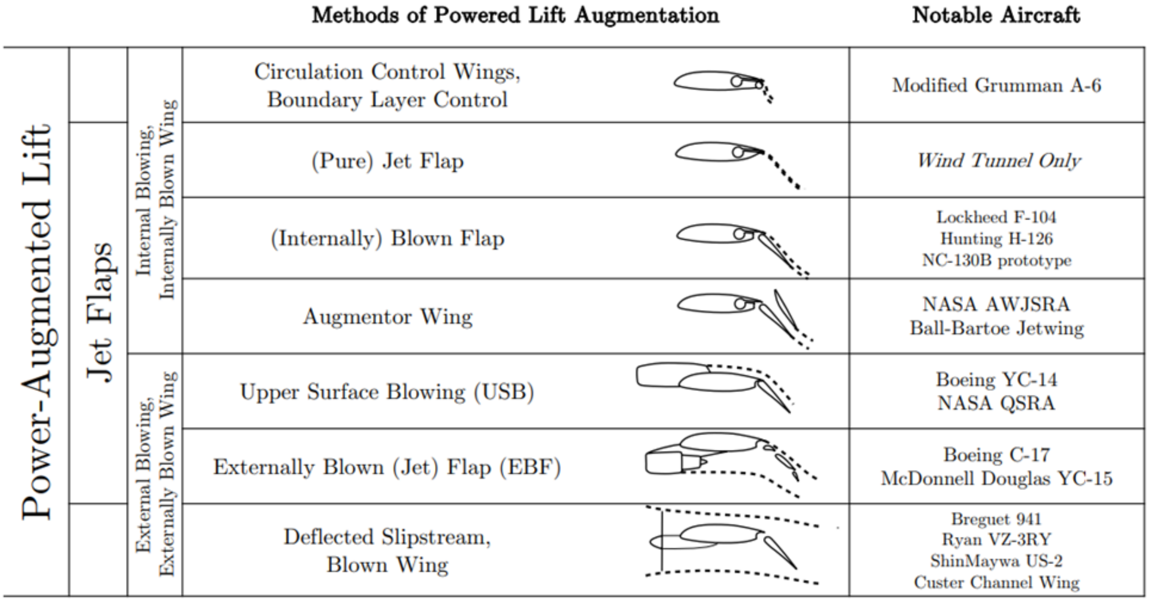

			Methods of Powered Lift Augmentation	Notable Aircraft
Power-Augmented Lift		Internal Blowing, Internally Blown Wing	Circulation Control Wings, Boundary Layer Control	Modified Grumman A-6
	Jet Flaps		(Pure) Jet Flap	*Wind Tunnel Only*
			(Internally) Blown Flap	Lockheed F-104 Hunting H-126 NC-130B prototype
			Augmentor Wing	NASA AWJSRA Ball-Bartoe Jetwing
		External Blowing, Externally Blown Wing	Upper Surface Blowing (USB)	Boeing YC-14 NASA QSRA
			Externally Blown (Jet) Flap (EBF)	Boeing C-17 McDonnell Douglas YC-15
			Deflected Slipstream, Blown Wing	Breguet 941 Ryan VZ-3RY ShinMaywa US-2 Custer Channel Wing

Figure 2.3: Powered lift augmentation concepts and aircraft where they have been applied [29].

Later, the upper-surface blown flap was used in the design of the Boieng YC-14 in the context of the Advanced Medium STOL Transport competition of the United States Air Force. This was only brought into fruition after it was demonstrated that this concept would still be effective in a wing with an aspect ratio of 7, leading edge sweep of 30 deg and a full span trailing edge flap with covered slots equipped with high-bypass turbofan engines, which have a lower temperature, lower pressure and thicker jet than the older engines used in earlier research [31].

Within this United States Air Force aircraft design competition, a different aircraft, the McDonnell Douglas YC-15, featured an under-the-wing externally-blown flap powered lift concept, where the double-slotted flap is designed to be inside the exhaust jet, at all deflection angles and the flap segments are separated by wide slots so that a substantial fraction of the exhaust jets flows through them [32].

In this configuration, it was shown that with increasing flap deflection, the jet flow disperses in the spanwise direction, eventually being distributed over the full flap span length, which, despite reducing the jet turning angle, improves the wing spanwise lift distribution, with a lower induced drag. This design would then serve as a baseline for the development of the Boieng C-17 Globemaster III in the 1980s, with a good STOL performance but longer range in mind [33].

These externally blown jet flap concepts have shown to have similar aerodynamic performance [31], with lift coefficients as high as 9, while conventional flapped aircraft generally have a maximum lift coefficient lower than 3 [34].

From the 1990s onward, the interest in STOL aircraft faded in the context of a more stable global peace panorama with high quality airfields. This created a need for more efficient propulsion systems and airframes in aircraft with long range and high payload capabilities.

In the last decade, the technological advancements in terms of electricity storage systems and fuel cells have allowed the use of electric propulsion systems in aviation.

Electric propulsion provides a wide range of benefits when compared to more commonly used powertrains, since electric motors have high power to weight ratios, high efficiency independent of scale and ambient conditions, lower cooling drag and more compact dimensions.

For example, high-temperature superconductive electric motors reportedly are able to have a specific power of 15 KW/kg and above 99% efficiency [35], which, when compared with traditional turboprop engines with a thermodynamic cycle efficiency of 50%, could improve the powertrain chain energy conversion efficiency by as much as 37% [36].

These characteristics overcome the past limitations associated to increasing the number of engines in commercial aviation and open a door to exploring distributed electric propulsion aircraft designs and their benefit to STOL operations. Different designs have been considered, with some projects already having gone through full-scale prototype testing phase.

One of these is the Electra EL2 aircraft, pictured in Figure 2.4, which uses a hybrid electric distributed propulsion system with 8 propellers distributed along the wing leading edge and also features double-slotted fowler flaps to take advantage of the powered-lift, having achieved speeds as low as 12.8 m/s and landings with 34 m of ground roll [37].

Another aircraft with leading edge distributed propulsion is the NASA Maxwell X-57, which although it wasn't designed with STOL operations in mind, provided important insights in term of distributed propulsion integration, with aerodynamic results including aero-propulsive effects of its 12 high lift propellers being limited to CFD simulations [38].

With a different approach, the ONERA AMPERE conceptual design [39] featured over the wing distributed propulsion which was tested with a scaled wind tunnel model, while the ONERA DRAGON [40] was a purely conceptual design, with its propellers under the wing, shown in Figure 2.5,

Figure 2.4: Electra EL2 [41]

Figure 2.5: ONERA DRAGON [42]

2.2. Isolated propeller

Making an analysis or establishing an hypotheses regarding the implications of propeller-driven propulsion on aircraft performance implies understanding the underlying aerodynamic phenomena during its operation.

A propeller can be seen as a set of rotating wings and, when an isolated propeller is in a flow field, its blades experience a lift and drag force loading which can then be decomposed into axial and tangential force components, imposing a flow motion in these directions [43].

The difference in pressure in the blades' upper and lower surface leads to the formation of blade trailing vortexes in the slipstream that form helixes, which, due to self-induced velocities, undergo a process of roll-up into distinct tip and root vortex systems [44], within a very short distance of the blade trailing edge. This physical behavior is schematized in Figure 2.6.

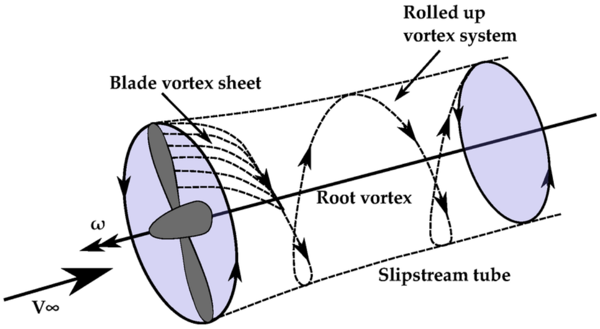

Figure 2.6: Propeller streamtube and vortex system. [45]

The axial increase of the flow's momentum is what generates the thrust force T, which can be calculated with Equation 2.1, where $\dot{m}$ is the air mass flow through the propeller, V_j is the axial flow velocity in the slipstream jet and V_∞ is the freestream flow velocity.

$$T = \dot{m}(V_j - V_\infty) \tag{2.1}$$

It follows that propulsive efficiency can be defined as the ratio of propulsive power $P_{propulsive}$ to a given shaft power P_{shaft}.

$$\eta_{propulsive} = \frac{P_{propulsive}}{P_{shaft}} = \frac{TV_\infty}{P_{shaft}} \tag{2.2}$$

Evaluating and comparing propeller performance requires non-dimensionalization of propeller performance indicators, which can be done with reference to propeller parameters or aircraft parameters [46], the later being more common when analyzing installed propellers.

In Equation 2.3 to Equation 2.8, the expressions to quantify torque Q, advance ratio J, thrust T and power P are shown.

$$J = \frac{V}{nD_p} \tag{2.3}$$

$$C_T = \frac{T}{\rho n^2 D_p^4} \tag{2.4}$$

$$C_Q = \frac{Q}{\rho n^2 D_p^5} \tag{2.5}$$

$$C_P = \frac{P}{\rho n^3 D_p^5} \tag{2.6}$$

$$T_C = \frac{T}{\frac{1}{2}\rho V^2 \pi R_p^2} \tag{2.7}$$

$$Q_C = \frac{Q}{\frac{1}{2}\rho V^2 \pi R_p^3} \tag{2.8}$$

A propeller can either operate on propulsive mode, braking mode or regenerative mode, depending on whether energy is added to the flow or drawn out of it by means of momentum transfer and if thrust is positive or negative, which can be adjusted through blade pitch angle and rotational speed control [47].

In positive thrust propulsive mode, with a positive angle of attack α, as shown in Figure 2.7, there is a total pressure jump and increase of the flow's axial and tangential velocities, which makes the slipstream tube contract, given the principle of conservation of mass.

In regenerative mode or braking mode, there is a negative angle of attack on the blades and the contrary behavior occurs, with an expansion of the slipstream and drop in the total pressure, also in the opposite direction of thrust.

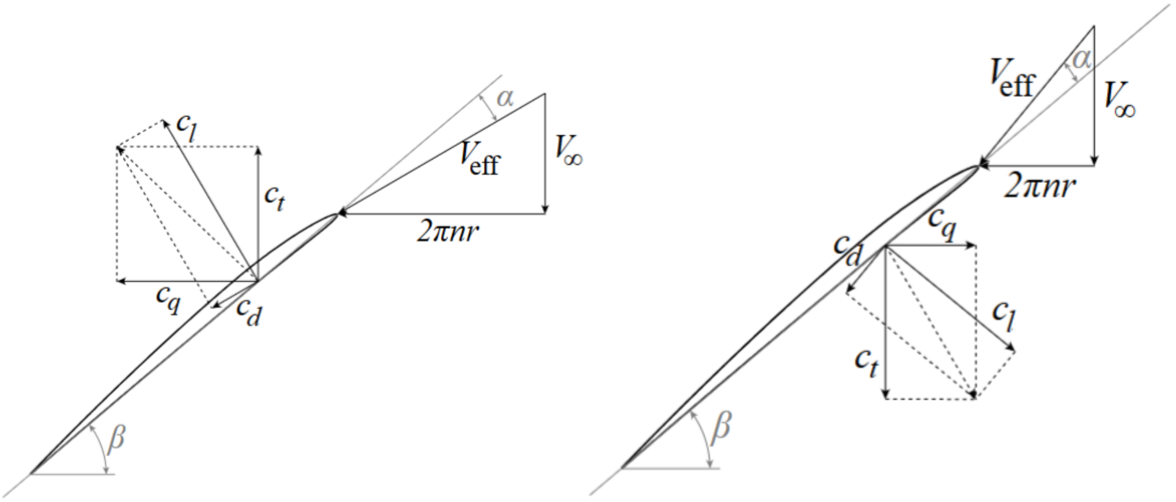

a) Propulsive mode **b)** Regenerative mode

Figure 2.7: Velocity triangles at a fixed-pitch propeller blade section in propulsive and regenerative modes [47].

Moreover, the contraction and expansion of the slipstream that occurs, due to a difference of its static pressure relative to the one outside it, also induces a radial velocity component on the flow, which is either amplified, in regenerative mode, or diminished, in propulsive and braking mode, by the Coriolis effect induced outward radial velocity on the flow, which delays boundary layer separation by increasing the chordwise separation point at higher radial positions [48].

The magnitude of this velocity component is usually small relative to the axial and tangential velocities in the slipstream, so it is often ignored in simplified propeller analyses or is only taken into account through tip corrections [49].

However, its influence on propeller performance can be significant at low advance ratios or high incidence angles [50] and, for example, in contra-rotating propellers, where the aft propeller is in a region of the fore propeller slipstream, which is not fully developed, with radial induced velocities that are stronger than further downstream.

The majority of propellers is designed to maximize performance in propulsive mode, which usually has as consequence an underwhelming performance in regenerative/braking mode.

Wind tunnel tests have been performed on a propeller at different pitch angle settings, freestream flow speeds and advance ratios and it was concluded that a maximum energy harvesting efficiency of 11%, which was limited by operating parameters that are close to the blade's stall conditions [51].

This value of energy harvesting efficiency occurred at low pitch angles and advance ratios, but also resulted in large values of negative thrust. Also, if a low negative thrust is required, higher pitch angles were more beneficial for energy harvesting, albeit at a lower harvesting efficiency.

The main flow mechanisms that result in a loss of propulsive efficiency are swirl, viscous effects and compressibility effects, which consume energy without it being used for thrust generation [52].

In highly loaded propellers, it was found that by decreasing a propeller's advance ratio in half and maintaining thrust coefficient, the propulsive efficiency losses related to tangential flow increased by a factor of four, mostly due to an increase in pressure drag, which is particularly strong near the propeller rotation axis [53].

Furthermore, when blade tip speeds are close to the speed of sound, at which shock waves start forming, experimental results showed a decrease of as much as 25% of thrust coefficient in a fixed pitch propeller, associated with a sharp increase in power coefficient needed, therefore, leading to a significant loss of propulsive efficiency [54].

Efforts to increase propulsive efficiency by reducing swirl related losses were first reported by NASA [55] through the introduction of swirl recovery vanes downstream of the propeller, which redirect the tangential flow in the slipstream into the axial direction and energy that would have been otherwise lost can be used for generating thrust.

In this study, 40% of the swirl was recovered, resulting in a system efficiency increase of around 5% relative to the configuration without the SRV. Similar results have been obtained in more recent research [56], where a 50% decrease in swirl kinetic energy was verified, characterized by a reduction of 95% in the radial positions closer to the propeller axis, but that the additional thrust would only result in a 2% improvement of propulsive efficiency.

Furthermore, compressibility effects can be avoided by limiting the propeller's operating rotational speed, which reduces the local blades' section flow speed, that is highest at the tips. However, reducing the propeller rotational speed may not be feasible for higher flight speeds, so blade shape considerations like sweep and thinner airfoils have been used to delay these undesirable effects [57].

2.3. Propeller-wing interactions

When a propeller is installed upstream of a wing and generates positive thrust, its slipstream will engulf sections of the wing, resulting in changes in its spanwise lift distribution, as the induced velocities in the slipstream will create different inflow characteristics for the wing [58].

If one considers that the slipstream is fully developed at the wing location, then radial velocity components of the slipstream will have a negligible effect on the wing, but the axial and tangential velocity components interference have different effects.

The axial velocity of the slipstream will result in a higher dynamic pressure over the wing, which is non uniform, given that there is a radial variation of the slipstream axial velocity magnitude over the propeller radius, but it is symmetrical relative to the propeller shaft axis.

The slipstream tangential velocity influence on the wing will depend on the rotation direction, as, for example, in an inboard up rotation setting, the angle of attack of the wing section inboard of the propeller axis will increase, and decrease in the outboard wing section, like shown in Figure 2.8, resulting in an anti-symmetrical lift distribution [44].

Similarly to the axial case, the tangential induced velocities also vary radially, which will make the propeller-wing interactions dependent on the vertical position of the propeller.

The region with an induced upwash will have a force vector tilted forward, which has a negative drag component that is essentially a recovery of the swirl back into thrust force. Conversely, the downwashed region has a resultant force vector tilted back, with an increase in drag force. The net combined effect of these propeller-wing interactions will depend on the loading of the wing sections affected, where the aerodynamic performance of highly loaded sections will be more strongly impacted and, as such, having an inboard up rotating propeller will be beneficial, with a net reduction in induced drag, which is the highest closer to the wing tip, where there are steeper loading gradients.

Additionally, this change in wing loading modifies the spanwise vorticity distribution, which, in turn, will have an effect on the inflow conditions over the whole wing and, consequently, when comparing the lift coefficient distribution of the powered wing versus the unpowered case, the impact isn't restricted to the slipstream diameter, but also outside of it.

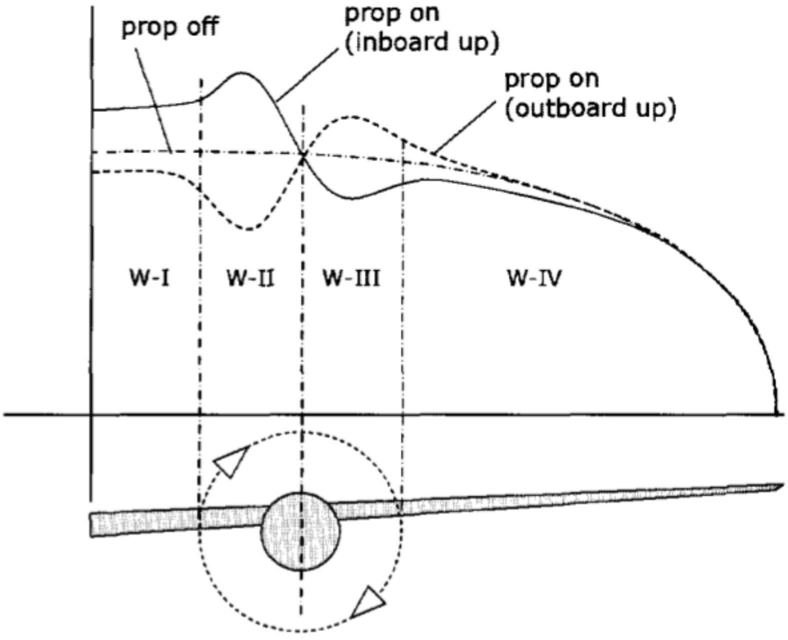

Figure 2.8: Lift distribution in wing regions affected by a propeller slipstream [44].

On another note, if, for example, a propeller is operating in breaking mode, depending on the advance ratio, the slipstream may flow in the contrary direction of the flight, flowing over lifting surfaces from trailing edge to leading edge. As far as it was found, little research on this particular flow condition has been conducted, given the reduced interest in propellers operating in negative thrust until recently.

The wing also has an effect on the upstream propellers, as during operation, the incoming wind vector doesn't always coincide with the propeller's axis [59], due to a misalignment of the propeller with the flight direction, one of the reasons being a non-zero angle of attack of the aircraft.

2.4. Aero-propulsive effects on performance

Despite there being a consensus in the scientific community that aero-propulsive effects can be harnessed to improve an aircraft's performance, it is still not evident what practical implementation details would lead to the best performance possible, with research showing varying levels of improvements with different aircraft geometries and operating points. In particular, there is a lack of knowledge regarding the maximum limits of these beneficial effects, due to the higher complexity of the interactions at more extreme conditions.

Experimental tests with wing-tip propellers on a tapered straight wing without twist and aspect ratio of 6.8 at a different Mach numbers, at both positive and negative thrust settings, demonstrated an unexpected trend at negative thrust [60], where a decrease in lift gradient was seen, but there was an increase of aerodynamic efficiency relative to the wing without the propeller configuration. This was attributed to a reduction in friction drag due to lower dynamic pressure over the section of the wing and a more efficient wing lift distribution, since the untwisted propeller-off configuration wasn't optimal.

Wind tunnel tests showed that a quasi-2D section of a flapped airfoil equipped with propellers along its full span could achieve lift coefficients of over 9.5 at a low-Reynolds number, with a 20 deg flap deflection and a jet momentum excess coefficient of 6.5, equivalent to an actuator disc theory propeller jet velocity 4 times higher than freestream airspeed, which is an increase of around 6 times the maximum achieved lift coefficient of the same geometry without any blowing effects [61].

In another example [62], the take-off performance impact on a distributed propulsion aircraft was studied and it was found that placing leading edge propellers closer to the wing, but in vertically lower position, would increase the maximum lift coefficient by as much as 42%. This was attributed to the wing being engulfed in the propeller slipstreams at higher angles of attack with this propeller positioning.

This scientific article shows that with increasing propeller count there is a larger increase in the maximum lift coefficient until the associated reduction in propeller diameter leads to a very low propeller diameter to wing chord ratio, at which point this trend flattens. Moreover, with smaller propeller diameters, the boost in performance becomes more sensitive to angle of attack changes, as the propeller slipstream size is reduced and less likely to engulf the wing.

Focusing on the spanwise distribution of the propellers, it was found that when adapting a conventional aircraft design into a full distributed propulsion configuration, using 3 larger propellers over the half-wing span would increase the aerodynamic efficiency by 5% and reduce the power consumption by 2.9%, but increasing the number of propellers with a lower diameter would eventually lead to a higher power consumption when compared to the original design [4].

Adding to this, using a partial distributed propulsion approach, with propellers placed in the outboard wing, showed better results, with a single wing-tip propeller configuration being the best. A parameter analysis was done to this configuration and, while the chordwise and vertical positions resulted in opposite effects on the power consumption and aerodynamic efficiency that balanced each other out, a slight inboard position, at spanwise position of 0.95 of the half span and an upward inclination of 3.75 deg of the propeller lead to the optimum performance, with a total improvement of aerodynamic efficiency of 17% and reduction in required power of 5.6%.

A lower number of propellers would be more beneficial for trimmed landing conditions according to some research [14] and, in this case, using 8 propellers could result in a lift gain of 22% when compared to the power-off lift, whereas the 12 and 16 propeller configurations provided a 13% and 19% gain, respectively. These values corresponded to operating the wing tip propeller at moderate negative thrust settings, which allowed more thrust to be distributed among the propellers in the flapped region of the wing, boosting the beneficial effects by 10% relatively to a homogeneous thrust distribution.

Furthermore, it can be shown that increasing the negative incidence of the propellers would lead to a higher apparent angle of attack of the wing, increasing lift, but could also lead to early stall [16] . Additionally, if the total installed power and wing area affected by the propellers slipstream remained constant, the wing lift coefficient also remained approximately constant, but with increasing number of propellers, the total thrust generated decreased.

2.5. Trimming

As discussed, being able to expand an aircraft's flight envelope is the main advantage of distributed propulsion, particularly at low speeds and in failure scenarios through redundancy, so it's relevant to understand how an aircraft is controlled during flight.

Conventional aircraft rely on control surfaces for stability and manoeuvring, the main ones being the elevator, for longitudinal motion, the rudder, for lateral motion, and the ailerons for roll motion.

Complementary to these, there are secondary control surfaces that focus on improving performance, especially at low speed conditions such as the flaps, which augment lift and, at high deflections, increase drag significantly or the slats, that reenergize the boundary layer over the wing and delay flow separation [63].

Moreover, there is a particularly important device which greatly aids pilots or flight control computers by reducing the required input force for a given control surface deflection: the trim tabs [64].

Trim tabs are a usually a plain-flap type surface on the trailing edge of elevator and rudder, but may also be just a bent piece of metal in the case of a simple aircraft that doesn't experience large hinge moments on its tail control surfaces and flies at a mostly constant airspeed. When deflected relative to the main control surface where it is installed, the trim tab generates an aerodynamic force which shifts the neutral position of the main control surface.

This effect is very useful when deflection control inputs are given around a high deflection angle, which would otherwise require the pilot to exert high forces on the stick and subject the components of the control system to strong loads for large periods of time, increasing both pilot and material fatigue.

During flight, these control surfaces help maintain the aircraft at a certain speed and attitude, also known as trimmed flight, in order to sustain a chosen steady rate of climb, rate of descent or be at steady level flight. Under steady level flight conditions, the sum of all moments and forces acting on the aircraft must be zero, therefore maintaining equilibrium.

The general aircraft state system is formulated as follows [9]:

$$g(\dot{x}, x, u_i) = 0 \tag{2.9}$$

where g is a vector of non-linear equations resultant from the 6-degree of freedom equations of motion. x is the vector of aircraft states and u_i is the vector of aircraft inputs, which, for a conventional aircraft are:

$$x = [N, E, D, \phi, \theta, \psi, u, v, w, p, q, r] \tag{2.10}$$

$$u_i = [\delta_T, \delta_a, \delta_{el}, \delta_{rud}] \tag{2.11}$$

Identifying the trim states for a system as complex as an aircraft is not a trivial problem, as there are several degrees of freedom that are often coupled or interact with each other [10].

For example, given the aeroelastic behaviour of an aircraft during flight, structures such as the wing or tail are under a torsion moment which causes them to twist, increasing angle of attack and, therefore also increasing the aerodynamic force. In particular, for the case of the control surfaces, these deformations can lead to a reduction of their control effectiveness or even control reversal [65].

Therefore, Equation 2.9 will be a vector of implicit equations that can, nevertheless, be transformed into explicit equations by imposing a set of constraints or conditions. For the trim problem, a state vector (x,u_i) must be a solution of Equation 2.9 when there are no accelerations, so where the kinematic state variables $x_k = [u, v, w, p, q, r]$ remain constant at their initial values, implying $\dot{x_k} = 0$.

Having said this, the state vector for the trim problem can be seen as a set of known variables ζ_i, determined by the nature of the flight condition studied, and a set of unknown variables which must be determined λ referred to as trim controls.

$$(x, u_i) = (\zeta_i, \lambda) \tag{2.12}$$

Depending on the number of trim controls, the trim problem can be categorized into determined, when there as as many trim controls as equations of motion; overdetermined, if there are less trim controls than equations of motion or underdetermined, if there are more trim controls than equations of motion.

For an aircraft that is free to move in the three-dimensional space, there are 6 degrees of freedom, in the form of a translation motion or rotational motion in each of the 3 different axis directions, and, therefore, there are 6 equations of motion [66].

Considering a body-fixed reference frame and an aircraft symmetrical about the longitudinal plane, the equations of motion are:

$$F_x = m(\dot{u} + qw - rv) \tag{2.13}$$

$$F_y = m(\dot{v} + ru - pw) \tag{2.14}$$

$$F_z = m(\dot{w} + pv - qu) \tag{2.15}$$

$$M_x = I_{xx}\dot{p} - I_{xz}(\dot{r} + qp) - (I_{zz} - I_{yy})rq \tag{2.16}$$

$$M_y = (I_{xx} - I_{zz})rp + I_{xz}(p^2 - r^2) + I_{yy}\dot{q} \tag{2.17}$$

$$M_z = (I_{yy} - I_{xx})qp + I_{xz}(qr - \dot{p}) + I_{zz}\dot{r} \tag{2.18}$$

where the body angular velocities are:

$$p = \dot{\phi} - \sin\theta\dot{\psi} \tag{2.19}$$

$$q = \cos\phi\dot{\theta} + \cos\theta\sin\phi\dot{\psi} \tag{2.20}$$

$$r = -\sin\phi\dot{\theta} + \cos\theta\cos\phi\dot{\psi} \tag{2.21}$$

Novel aircraft designs often result in underdetermined trim problems, as is the case with distributed propulsion aircraft, where the possibility of using differential thrust settings increases the number of trim controls.

The underdetermined trim problem has been studied for blended-wing-body aircraft under no sideslip and crosswind conditions, using three different methods [67] . More insights are given in [10], where a box-wing aircraft is analyzed with the goal of determining trim states with maximum control authority.

One of the methods used is the classic method, where a cost function is minimized with target translational and rotational accelerations of zero such as

$$\begin{aligned} \min_{\boldsymbol{\lambda}} \quad & \mathcal{J} = [\dot{x_k}]^T Q_p [\dot{x_k}] \\ \text{subject to} \quad & \boldsymbol{\lambda}_{\text{lb}} \leq \boldsymbol{\lambda} \leq \boldsymbol{\lambda}_{\text{ub}} \end{aligned} \tag{2.22}$$

where Q_p is the penalty matrix, a diagonal matrix that controls the importance of each acceleration component for the minimization.

If a solution exists, this minimization quickly leads to a trim solution if given a good initial guess, however, it may not be the most aerodynamically efficient one. Therefore, a common modification done is including the drag force in the objective function to find the trim states with minimum drag:

$$\begin{aligned} \min_{\boldsymbol{\lambda}} \quad & \mathcal{J} = D \\ \text{subject to} \quad & \boldsymbol{\lambda}_{\text{lb}} \leq \boldsymbol{\lambda} \leq \boldsymbol{\lambda}_{\text{ub}} \\ & \dot{x_k} = 0 \end{aligned} \tag{2.23}$$

The third method consists of looking at the pilot input variables included in the trim controls not as deflections, but as the moments or forces they generate. In this case, the equations of motion are used to determine the required force and moments for trim and, through Direct Control Allocation, they are translated into deflections by exploring the attainable moment set which relates deflections to the resultant chosen dimensionless moment or force coefficients ΔC_F. The minimization problem can be formulated as:

$$\begin{aligned} \min_{\boldsymbol{\lambda}} \quad & \mathcal{J} = \|\Delta C_F - B\lambda\| \\ \text{subject to} \quad & \boldsymbol{\lambda}_{\text{lb}} \leq \boldsymbol{\lambda} \leq \boldsymbol{\lambda}_{\text{ub}} \end{aligned} \tag{2.24}$$

where B is the effectiveness matrix of the control surfaces composed by each linear control derivative.

This method has the advantage of not scaling the trim controls with the number of control surfaces and could also be adapted to minimize drag.

The classic trimming method has been used with a restrictive set of constraints to study the changes of the maximum lift coefficient for a distributed propulsion aircraft during landing, by considering one thrust trimming scenario at a constant angle of attack and another at a constant effective lift coefficient determined by the certification requirements for large aircraft [14]. It was concluded that the maximum effective lift coefficient was dependent on the available thrust, as the lifting boosting potential was limited by the thrust trimming strategy chosen.

Also, the handling qualities and low-speed trimmed performance of distributed electric propulsion aircraft have been studied [15]. To do so, a low-speed trim point was identified and the flight parameters were varied around that trim point. Then, the force coefficient responses were approximated with linear fits, for single variable influence, and polynomial fits, for coupled effects sensitivity studies.

It was found that the throttle setting and angle of attack coupling was the most influential to the aerodynamic force coefficients, with the inboard engines having the strongest influence for lift generation. When it comes to lateral movement analysis, an unexpected result was shown, with the thrust setting of the second most outboard engine having the most influence on the roll and yaw moments, instead of the engine closer to the tip, even though it has a shorter moment arm.

Additionally, the propeller-wing interactions with homogeneous thrust settings showed that, at the minimum speed, lower angles of attack were needed, but a higher thrust setting was required when compared to the case without propeller-wing interactions considered. The minimum speed was defined by the stall on the elevator, which had to be deflected to its maximum to counteract the strong nose-down pitching moment generated by the propeller-wing system.

Delving further into this topic, multi-disciplinary design optimization on the Maxwell X-57 aircraft design demonstrated that, by using propellers with different diameters and thrust settings along a section of the wing without any gaps between propellers, it would be possible to further reduce the trimmed stall speed by 3.2% using a 8 propeller configuration when the elevator had been limited by a maximum deflection, or, if the elevator deflection had a higher limit, the trimmed stall speed could be reduced by 6.3% with a 10-propeller configuration [16], as shown in Figure 2.9.

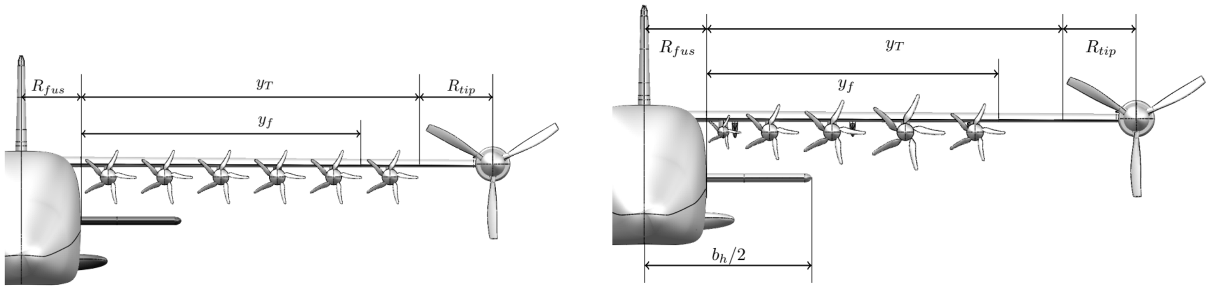

a) Original NASA X-57 Maxwell, with 12 identical propellers.

b) Optimized design with 10 propellers.

Figure 2.9: Original and optimized DEP system geometry [16].

In these optimized designs, there is one propeller which is larger than the rest and, therefore, it has the largest contribution to aircraft thrust and lift generation through aero-propulsive interactions, making it more critical when considering engine failure situations.

2.6. UNIFIER19 project

The UNIFIER19 - Community Friendly Miniliner project [17, 18] was started in the European Union with the goal of designing an environmentally friendly 19-passenger hybrid-electric commuter aircraft, with which it would be possible to establish a wider transport network by making use of small airports and unprepared runways. Out of this project resulted the Unifier C7A-HARW aircraft design.

This aircraft features a tapered high aspect ratio wing without leading edge sweep and a slight negative dihedral angle, attached to the upper part of the fuselage. Also, there is a v-tail aft of the main wing.

The control surfaces consist of a flap and aileron on each half of the main wing and a ruddervator on each side of the tail.

As shown in Figure 2.10, the propulsion system is composed by a leading edge distributed electric propulsion system (DEP) of 12 fixed pitch foldable high-lift propellers on the main wing and a horizontal thrust unit (HTU), which is a variable pitch propeller mounted on the rear of the fuselage.

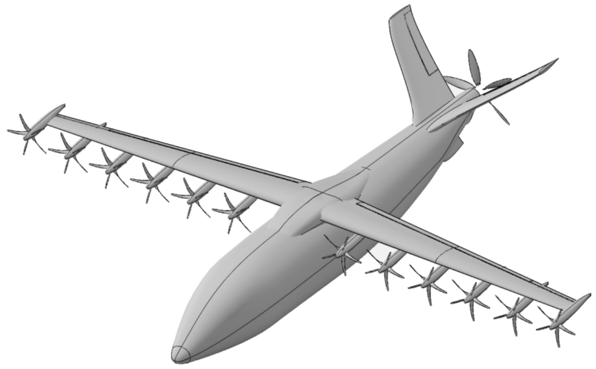

Figure 2.10: Unifier C7A-HARW - OpenVSP model geometry [68].

In order to simulate flight dynamics and test control laws for distributed electric propulsion aircraft, a Simulink model of the Unifier C7A-HARW was developed [69].

The aero-propulsive interactions are calculated by dividing the geometric model into several segments, which are then analyzed separately with FlightStream.

FlightStream is a panel-method aerodynamic solver that incorporates an integral boundary layer to icorporate viscous effects into the otherwise invisicid method, viscous-coupling equations to model the thickening and decambering effect of the boundary layer and advanced boundary conditions for propeller simulation.

This segmentation enables obtaining results considering local flow conditions, while maintaining the computational time low considering the highly coupled effects here present.

However, it leads to the neglect of wing-tail, wing-fuselage and tail-fuselage interactions, out of which the most significant is the wing's downwash on the tail. To correct this, the wing downwash is calculated at the tail position and included into the tail simulations.

The result of all the simulations is a multi-dimensional look-up table that can be used and interpolated to determine the different forces and moments acting on the aircraft, which can then be summed to determine the total value relative to a reference point such as the center of mass.

A relevant aspect to mention is that, while the aircraft states and control surface deflections are inputted with their absolute values, the propulsive thrust settings are not.

On one hand, the DEP thrust settings are controlled through an activity factor [0,1], where 0 corresponds to propellers generating no thrust and 1 to propellers generating their maximum thrust force of 800 N.

This thrust force request is transformed into an RPM request value through the lookup tables, which will be subject to the electric motor inertial effects and only after will it become the true propeller RPM value and corresponding true thrust force, which will have an impact on the wing's local flow.

On the other hand, the HTU can operate on braking mode, generating negative thrust. Therefore, the activity factor limits for the HTU [-0.5, 1.5] is a range scaled by 0.001 relative to the minimum and maximum thrust values of the HTU propeller, whose limits may not be attainable for a given airspeed, due to the motor's operating power limits.

Since the HTU propeller has variable pitch, there are different RPM-pitch combinations that would result in the same thrust value, so the RPM value that consumes the least amount of power for a given thrust value was chosen to build the look-up tables.

All in all, the process works by, given an initial aircraft state and control inputs, calculating the local angles of attack and airspeed of the main wing segments and interpolating the forces and moments of those segments with the lookup tables. This is followed by determining what the induced angle of attack and airspeed on the tail.

Next, the local conditions of the tail segments are calculated and, after combined with the induced values caused by the main wing, are used with the look-up tables to determine the forces and moments on the tail.

Lastly, contributions from the fuselage and other non-lifting bodies are added to the total force and moments results. These final results can then be inputted into the equations of motion to determine the aircraft accelerations, for example.

3

Research Proposal

With a large number of propellers, the possibility of using differential thrust settings with electric motors opens up an unknown number of combinations for optimal performance that is interesting to study.

Furthermore, in trimmed steady flight, both longitudinal and lateral equilibrium must be maintained. A given thrust setting may lead to the generation of enough lift to compensate the aircraft weight, but it may be lower than the drag force, therefore not being longitudinally in equilibrium.

On the other hand, one of the most relevant operational problems that specifically affects these aircraft is how to the maintain the required lift force for vertical equilibrium, while also maintaining a low enough speed that allows it to land in short runways. This occurs because the lift force generated is highly coupled with the throttle setting of the propulsion system, resulting in an undesirably high thrust force that prevents lower speeds. One possible aircraft design solution is to include propellers operating in breaking mode, with negative thrust that counteracts the high thrust of the high lift propellers.

One example of such design is the Unifier C7A-HARW, which features a tail-mounted dual-purpose propeller that can be used in propulsive mode during cruise and breaking mode during landing and a distributed electric propulsion system along the main wing's leading edge.

As explored in Chapter 2, there has been research done on aircraft with distributed propulsion that identified a strong nose-down pitching moment as a limiting factor for reducing the minimum speed. Exploring the coupling between the DEP system and the HTU may reduce this effect.

Having said that, this thesis project aims to answer the following research questions:

Research Questions

1. How can the use of the installed propellers, control surfaces and flight conditions be combined to optimize performance indicators?
2. How can the relationship between performance indicators and trim controls be expressed analytically?

Part II

Scientific Article

Trim Optimization for Aircraft with Distributed Electric Propulsion and a Tail Thrust Unit

Guilherme Fernandes Lourenço

Faculty of Aerospace Engineering, Delft University of Technology

Abstract

This paper presents a trim optimization methodology for aircraft featuring distributed electric propulsion (DEP) systems and horizontal thrust units (HTU). The Unifier C7A-HARW, a 19-passenger hybrid-electric commuter aircraft with 12 wing-mounted propellers and a tail-mounted HTU, serves as the reference configuration. Multiple trim solutions with different types of propulsion systems usage and performance indicators, such as maximum range, endurance or lift-to-drag ratio, are explored through optimization, revealing complex relationships between angle of attack, airspeed, flap deflection, ruddervator deflection, required aerodynamic power and electric power consumed in steady level flight. Some unexpected results demonstrate that maintaining a constant low angle of attack and gradually reducing flap deflection as airspeed increases is desirable for lowering aerodynamic power requirements in trim conditions and that the wing tip propeller has an important role under certain circumstances. Empirical correlations between power requirements, angle of attack, airspeed, flap and ruddervator deflections are established, providing insights into the performance characteristics of DEP aircraft configurations and enabling efficient trim performance predictions useful for conceptual design.

Keywords: Distributed Electric Propulsion, Trim Optimization, Aircraft Performance, Flight Mechanics

Nomenclature

Symbols and Abbreviations

α	Angle of attack
δ_{HTU}	HTU propeller activity factor
δ_a	Aileron deflection
δ_f	Flap deflection
δ_r	Ruddervator deflection
δ_{T_i}	DEP propeller activity factor
$\dot{p}, \dot{q}, \dot{r}$	Angular accelerations in body axes
$\dot{u}, \dot{v}, \dot{w}$	Translational accelerations in body axes
$\dot{x}_{\text{k}}$	Accelerations in body axes array
η	Efficiency
γ	Flight path angle
λ	Trim controls array
ρ	Air density
τ	Flap effectiveness
θ	Pitch angle
C_m	Pitching moment coefficient
$C_{D,\ airframe}$	Drag coefficient of the airframe
C_{D_0}	Zero lift drag coefficient
$C_{L,\ airframe}$	Lift coefficient of the airframe
C_{L_0}	Lift coefficient at an angle of attack of 0 deg
C_{L_α}	Lift curve slope
D	Drag
E_{spec}	Specific endurance
i_{DEP}	DEP propeller installation angle
k	Induced drag factor
L	Lift
L/D	Lift to drag ratio
P_{elect}	Electric power consumed
P_{req}	Required aerodynamic power
P_{shaft}	Propeller shaft mechanical power
R_{spec}	Specific range
S	Wing area
V	Airspeed
V_S	Stall airspeed
V_{Emax}	Maximum endurance airspeed
V_{LDmax}	Maximum lift to drag ratio airspeed
V_{Rmax}	Maximum range airspeed
W	Weight
CFD	Computational Fluid Dynamics

DEP	Distributed Electric Propulsion
HTU	Horizontal Thrust Unit

Subscripts

lb, ub	Lower and upper bounds
norm	Normalized
envelope	All configurations and flight conditions

1 Introduction

Emerging novel aircraft configurations featuring wing-mounted distributed propulsion are characterized by strongly coupled aero-propulsive phenomena [1, 2, 3]. The coupling is due to the interaction between the propeller slipstreams and the flow around the main and secondary lifting surfaces [4, 5]. This interaction entirely determines the flight performance of these aircraft, making its analysis and optimization significantly more challenging [6].

In a blown-lift aircraft configuration, for example, the propulsion system is distributed along the leading edge of the wing in order to take advantage of the accelerated flow over the wing sections behind the engines. This arrangement generates more lift and energizes the boundary layer, allowing for the reduction of the overall wing size without causing earlier stall onset, which is relevant at lower speeds [7, 8].

Identifying the trim states and controls for such a complex system in various flight conditions is not a trivial problem, as the available degrees of freedom are redundant and also coupled. The possibility to use different thrust settings on each propeller increases the number of trim controls, making the trim problem underdetermined [9, 10]. This creates the conditions for multiple trim solutions to exist for the same flight condition, which can be exploited to optimize the aircraft performance [11, 12, 13].

Studies show that the maximum effective lift coefficient of a trimmed aircraft during landing is dependent on the available thrust and, therefore, the lift augmentation potential can be limited by the chosen trimming strategy [14]. Also, it has been reported that the elevator effectiveness can be the limiting factor for trimming at low airspeeds and there is available evidence that the coupling between angle of attack and thrust settings of the distributed propulsion system is one of the most impactful couplings to aerodynamic forces [15].

Another study demonstrates that when trim is being constrained by the elevator deflection, using an array of distributed propulsion propellers with different geometric characteristics may allow trimmed flight at lower airspeeds than before [16].

This raises the question on whether it would be possible to improve trimmed aircraft performance by coupling different available propulsion systems on the same aircraft.

This paper presents a methodology to explore the trim solution space for aircraft with distributed electric propulsion systems and horizontal thrust units, with particular emphasis on low-speed performance. It also provides simplified empirical relations between the required aerodynamic power P_{req} and trim variables, which could be used for preliminary design and optimization.

The Unifier C7A-HARW is chosen as the reference aircraft to apply the selected methodology and compare the results. It is a 19-passenger hybrid-electric commuter aircraft featuring a distributed electric propulsion system on the main wing and a horizontal thrust unit behind the tail [17, 18, 19].

The next Section 2 provides more details about the flight mechanics' simulation model used. In Section 3, the trim problem is described, along with the test cases considered and the empirical analytical expression derivation process. All the results and findings for the different propulsion configurations simulated are analyzed in Section 4. As a final point, in Section 5, conclusions are presented and some possibilities for future research are given.

2 Reference Aircraft

The aircraft design that is used in this study is the Unifier19 C7A-HARW, represented in Figure 1.

It features a tapered high aspect ratio wing without leading edge sweep and a slight negative dihedral angle, attached to the upper part of the fuselage. Aft of the main wing, there is a v-tail.

The control surfaces consist of a flap and aileron on each half of the main wing and a ruddervator on each side of the tail.

The propulsion system is composed by a leading edge distributed electric propulsion system (DEP) of 12 fixed pitch foldable high-lift propellers on the main wing, with a tilt angle of -5 deg relative to the wing reference frame, and a horizontal thrust unit (HTU), which is a variable pitch propeller mounted on the rear of the fuselage.

It is designed so that, during takeoff, the DEP provides additional thrust and, through the aero-propulsive interactions with the airframe, boosts lift generation, allowing shorter takeoff distances. However, during cruise the DEP propellers are folded to reduce drag and only the HTU provides thrust. In landing phase, the DEP propellers are activated again to improve low-speed performance.

In order to simulate flight dynamics and test control laws for distributed electric propulsion aircraft, a six-degrees-of-freedom rigid body model of the Unifier C7A-HARW was developed and implemented in MATLAB Simulink [20], which is used in this work.

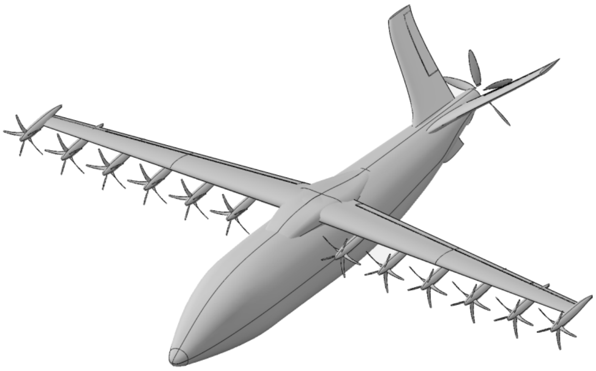

Figure 1: Geometry of the Unifier C7A-HARW in OpenVSP [17].

2.1 Aero-propulsive Modelling

The aero-propulsive forces are calculated from pre-computed databases, which were obtained from multi-fidelity CFD simulations.

The wing and tail surfaces are split into sections, for which the aerodynamic coefficients and downwash effects are tabulated as a function of the local flight and control parameters, allowing for the simulation of a wide range of operating conditions and capturing the coupling effects without an exponentially high computational cost.

It is important to emphasize that the only aero-propulsive interactions accounted for in the model are the DEP-wing interaction and the wing-tail downwash effect. Therefore, any interaction with the fuselage or between segments of the same component are not considered.

All the segment forces and moments can then be summed to determine their total values relative to a reference point such as the center of mass and, subsequently, determine the aircraft's accelerations with the equations of motion.

As inputs, the model receives thrust "activity factors" for each DEP propeller and the HTU. Each propeller is set to generate a maximum of 800 N of thrust force and any input lower than 0.8 N is set to zero thrust force and without considering any mechanical limitation. On the other hand, the HTU is able to generate both positive and negative thrust force, from -5000 N to 15000 N, bounds which are not always attainable depending on the airspeed, due to the motor's operating power limits. While each DEP propeller activity factor has a range of [0,1], from no thrust force to maximum thrust force, the HTU propeller activity range is [-0.5, 1.5], equivalent to a scaling by 10^{-4} of the requested thrust force.

Since the HTU propeller has variable pitch, the propeller performance database is computed considering the most efficient RPM for a given thrust request.

Furthermore, the absolute values for the deflections of the control surfaces and the initial flight conditions are required inputs.

The reference geometric and mass parameter values used for the simulations are shown in Table 1.

Table 1: Geometric and mass parameters of the Unifier C7A-HARW [20].

Parameter	**Value**
Mass	7438.0 kg
Center of Mass Position	(-8.32, 0, -0.20) m
Wing Area	29.98 m^2
Wing Span	20.11 m
Wing Chord	1.43 m

3 Methodology

The research presented in this paper focuses on the longitudinal-symmetric flight condition, as shown in Figure 2, where there is no lateral movement and all control surface deflections and thrust settings are symmetrical about the longitudinal plane. Consequently, the number of DEP thrust settings is reduced from 12 to 6 and both the flaps and ruddervators deflections from 2 to 1. Furthermore, standard sea level conditions are assumed.

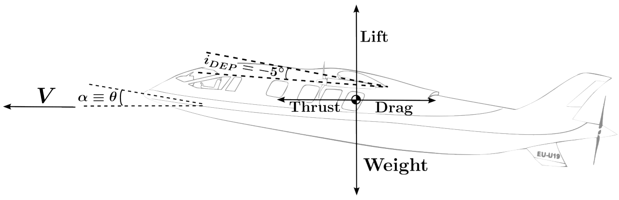

Figure 2: Aircraft point mass force diagram in trimmed level flight.

3.1 Aero-propulsive interaction model evaluation

First, to evaluate the aero-propulsive interactions captured by the flight mechanics model, a parameter sweep of flight conditions, control surfaces and thrust settings on the untrimmed aircraft is done. The values used are represented in Table 2.

The simulations done focus on obtaining results to determine the effect of the relationship between the DEP activity factor and the aircraft angle of attack

Table 2: Parameter sweep values for wing-DEP aero-propulsive model analysis, with δ_r = 0 deg, δ_a = 0 deg, $\delta_{T_{\text{HTU}}}$ = 0.

Variable	Minimum Value	Maximum Value	Step
V (m/s)	33	80	—
α (deg)	-15	20	1 deg
δ_f (deg)	0	25	—
δ_{T_i}	0	1	0.1

on the wing performance, at low and high airspeeds and with low and high flap deflections.

Some control parameters, namely the ruddervator deflection, aileron deflection and HTU activity factor are set to zero, as the model doesn't include any aerodynamic effects caused by the HTU or ruddervator on the wing and the aileron is fixed for simplicity, given the longitudinal flight condition.

3.2 Trim Problem

Two different trim problem formulations are explored to determine the equilibrium conditions in level flight (Equation 1).

$$\gamma = 0 \iff \theta - \alpha = 0 \iff \theta = \alpha \tag{1}$$

In both formulations, $\dot{x}_\text{k}$ represents the array of body-axis translational and rotational accelerations (Equation 2) and $\boldsymbol{\lambda}$ is the array of decision variables, also called trim controls (Equation 3), that the trim optimizer varies to search for trim conditions. The ailerons deflections are again set to 0 deg.

$$\dot{x}_\text{k} = [\dot{u}, \dot{v}, \dot{w}, \dot{p}, \dot{q}, \dot{r}]^T \tag{2}$$

$$\boldsymbol{\lambda} = [V, \alpha, \delta_f, \delta_r, \delta_{T_i}, \delta_{T_{\text{HTU}}}]^T \quad \text{with } i = 1, ..., 6 \tag{3}$$

To begin with, the airspeed is minimized, therefore being the objective function itself, while subject to steady level flight constraints (Equation 1 and Equation 4). This results in the minimum speed obtainable by the aircraft in steady level flight, given the available control surfaces deflections and propeller activity factors, displayed in Table 3.

$$\begin{aligned} \min_{\boldsymbol{\lambda}} \quad & \mathcal{J} = V \\ \text{subject to} \quad & \dot{x}_\text{k} = 0 \\ & \boldsymbol{\lambda}_\text{lb} \leq \boldsymbol{\lambda} \leq \boldsymbol{\lambda}_\text{ub} \end{aligned} \tag{4}$$

Next, the classic trim problem is used for a trim condition search at a given fixed airspeed. Here, the objective function being minimized is the sum of the squared translational and rotational accelerations (Equation 5).

$$\begin{aligned} \min_{\boldsymbol{\lambda}} \quad & \mathcal{J} = \dot{x}_\text{k}^T \dot{x}_\text{k} \\ \text{subject to} \quad & \boldsymbol{\lambda}_\text{lb} \leq \boldsymbol{\lambda} \leq \boldsymbol{\lambda}_\text{ub} \end{aligned} \tag{5}$$

Table 3: Trim control bounds.

Parameter	Minimum Value	Maximum Value
V (m/s)	0	89
α (deg)	-15	20
δ_f (deg)	0	25
δ_r (deg)	-30	15
δ_{T_i}	0	1
$\delta_{T_{\text{HTU}}}$	-0.5	1.5

To explore the solution space thoroughly, each optimization problem is run 500 times with random initial guesses, as multiple trim solutions may exist for the same flight condition. Out of these solutions, there can be some aircraft states that are not converged solutions of the trim problem and are simply the last function evaluation done before the maximum number of function evaluations was reached.

This is common when, for example, the optimizer is exploring a domain region with very steep gradients, causing it to eventually break the steady level flight constraint. Therefore, only aircraft states that meet the criteria of $\dot{x}_k^T \dot{x}_k <= 10^{-3}$ are considered.

The optimization problems are solved with MATLAB's `fmincon` and the solver settings used are shown in Table 4.

Table 4: Solver settings for the `fmincon` function.

Parameter	Value
`Algorithm`	`sqp`
`TolFun`	1×10^{-10}
`TolX`	1×10^{-10}
`FinDiffType`	`central`
`DiffMinChange`	1×10^{-10}
`DiffMaxChange`	5×10^{-1}

All trim control values are normalized before being inputted into the optimizer (Equation 6), to ensure a smooth optimization procedure that isn't numerically ill-conditioned, guaranteeing gradients that are all in the same magnitude scale.

$$\lambda_{i_\text{norm}} = \frac{\lambda_i - \lambda_{\text{lb},i}}{\lambda_{\text{ub},i} - \lambda_{\text{lb},i}} \tag{6}$$

3.3 Test Cases

Three propulsion systems usage combinations are studied in trim condition, to understand how the trim controls change given different propulsive constraints. Each test case is presented in Table 5.

The most general case is when both the HTU and the DEP are active and without any set constraints beyond their own operating limits. The second and third cases consider either only the DEP or only the HTU active.

Table 5: Test cases' fixed and free trim controls (i = 1,...,6).

Case	Trim Problem Objective	Free Trim Controls	Fixed Trim Controls
HTU and DEP	Minimize V	$[V, \alpha, \delta_f, \delta_r, \delta_{T_i}, \delta_{T_{\mathrm{HTU}}}]$	–
	Trim Condition Search	$[\alpha, \delta_f, \delta_r, \delta_{T_i}, \delta_{T_{\mathrm{HTU}}}]$	V
Only DEP	Minimize V	$[V, \alpha, \delta_f, \delta_r, \delta_{T_i}]$	$\delta_{T_{\mathrm{HTU}}} = 0$
	Trim Condition Search	$[\alpha, \delta_f, \delta_r, \delta_{T_i}]$	$[V, \delta_{T_{\mathrm{HTU}}} = 0]$
Only HTU	Minimize V	$[V, \alpha, \delta_f, \delta_r, \delta_{T_{\mathrm{HTU}}}]$	$\delta_{T_i} = 0$
	Trim Condition Search	$[\alpha, \delta_f, \delta_r, \delta_{T_{\mathrm{HTU}}}]$	$[V, \delta_{T_i} = 0]$

Additionally, in order to look at the implications of DEP spanwise thrust distribution on performance, the case that considers only the DEP active is further scrutinized with prescribed DEP thrust distributions: rectangular, trapezoidal and elliptical.

For this, an activity factor sweep of the most inboard propeller activity factor is done using $\delta_{T_1} = \{0, 0.05, 0.1, 0.2, ..., 1\}$.

In this instance, the optimizer searches for the activity factor of the most outboard propeller and the remaining thrust settings become defined by the fixed thrust distribution.

For the trapezoidal distribution case, all slopes for the trapezoid leg are possible, whereas for the elliptical distribution, the thrust value for the most inboard propeller is always the highest.

3.4 Performance Indicators

Relevant aircraft performance indicators, such as specific range, specific endurance and lift-to-drag ratio are all obtained from the numerical results of the simulations, using Equation 7 to Equation 11. The values of the electric motors and power-controller efficiencies are 0.95 and 0.97, respectively [18].

$$\begin{aligned} P_{elect} &= P_{HTU_{elect}} + P_{DEP_{elect}} = \\ &= \eta_{motor} \cdot \eta_{power-controller} \cdot (P_{HTU_{shaft}} + P_{DEP_{shaft}}) \end{aligned} \tag{7}$$

$$P_{req} = V \cdot D \tag{8}$$

$$R_{spec} = \frac{V}{P_{elect}} \tag{9}$$

$$E_{spec} = \frac{1}{P_{elect}} \tag{10}$$

$$\mathrm{L/D} = \frac{\mathrm{L}}{\mathrm{D}} \tag{11}$$

3.5 Analytical Expression Derivation

A least squares regression fit was applied to airframe trim controls, P_{req} and $C_{L,\ airframe}$ to determine analytical expressions that allow their calculation, given the airspeed and/or another trim control value.

All the regression fits are done using MATLAB's `fit`, with a prescribed equation type, based on some longitudinal equilibrium equations and standard aerodynamic approximations.

4 Results

4.1 Wing Aero-Propulsive Effects

The values for the wing lift coefficient of the untrimmed aircraft for a selection of airspeeds, angles of attack, flap deflections and DEP activity factors are shown in Figure 3 to Figure 6. Also, in Table 6, a comparison of the wing lift coefficient value change resultant from a DEP activity increase from 0 to 1 is displayed.

Looking at the low airspeed case of 33 m/s, in Figure 3 and Figure 4, it is possible to see that, for the entire range of angles of attack and when DEP activity factor increases, at the maximum flap deflection of 25 deg there is a higher lift coefficient increase when compared to the minimum flap deflection of 0 deg. This was expected, as increasing the DEP activity factor leads to a higher dynamic pressure at the wing and increasing flap deflection results in a higher effective wing camber, which redirects the airflow with a more downward angle.

Furthermore, the magnitude of this lift boost, in the linear region of the lift coefficient curve, is more pronounced at lower positive and more negative angles of attack when compared to the change at higher angles of attack, such as the maximum lift angle of attack. In particular, in the lower end of the linear lift regime, a flap deflection of 25 deg, leads to a lift increase of more than 300% when compared to the flap deflected at 0 deg, whereas at the maximum lift angle of attack, increasing the flap deflection doesn't have a significant impact on the lift boost, being only 8% higher.

This may be explained by the fact that, at low angles of attack, where lift force is also lower, the wing can more efficiently accelerate the flow than at higher angles of attack, where it is already generating a lot of lift and the additional increase of dynamic pressure by the propeller slipstream is not able to pull more air into the wing's influence. At negative angles of attack, this can further be explained by the less negative effective angle of attack the wing experiences due to the propeller slipstream adding an upwards velocity component to the local flow.

The slope of the linear regime of the lift curve becomes steeper by 15% when the DEP activity factor goes from 0 to 1, for both flap deflections, demonstrating a higher sensitivity to angle of attack changes.

The only change to the maximum lift angle of attack is due to the flap deflection increase, which reduces it from 13 deg to 12 deg, as is expected given that, with a flap, the adverse pressure gradient experience by the flow is stronger and, therefore, leads to earlier stall. However, one unexpected result is that this reference parameter remains the same for any

Table 6: Wing lift coefficient change as DEP activity factor increases from 0 to 1, for different airspeeds, angles of attack and flap deflection combinations.

V	α	δ_f	C_L at $\delta_{T_i} = 0$	C_L at $\delta_{T_i} = 1$	Change
33	-15	0	-0.61	-0.43	+42.0%
33	-15	25	0.40	0.96	+138.1%
33	13	0	1.70	2.24	+31.9%
33	12	25	2.58	3.47	+34.4%
80	-15	0	-0.61	-0.57	+5.7%
80	-15	25	0.40	0.51	+25.2%
80	13	0	1.70	1.80	+5.1%
80	12	25	2.58	2.75	+6.4%

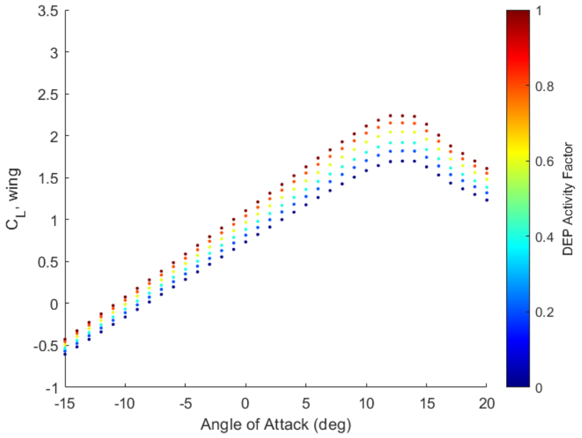

Figure 3: Wing lift coefficient as a function of angle of attack and DEP activity factor at $V = 33$ m/s, $\delta_f = 0$ deg.

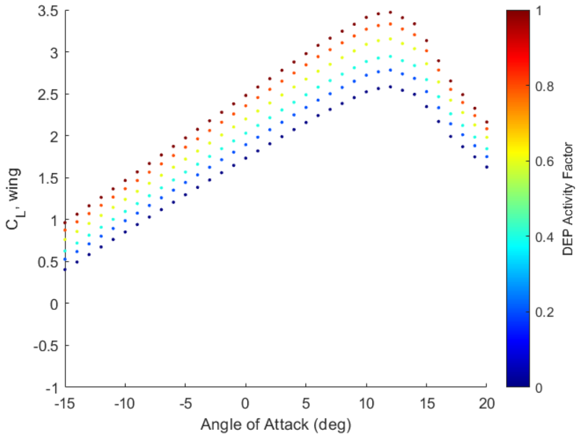

Figure 4: Wing lift coefficient as a function of angle of attack and DEP activity factor at $V = 33$ m/s, $\delta_f = 25$ deg.

DEP setting, which is likely due to limitations of the multi-fidelity CFD simulations' aerodynamics models used to generate the aerodynamic database, that don't model the boundary layer with enough detail to detect the interaction between it and the propeller slipstream.

When it comes to the high airspeed case of 80 m/s, in Figure 5 and Figure 6, the magnitude of lift of the boost effect of DEP is significantly reduced when

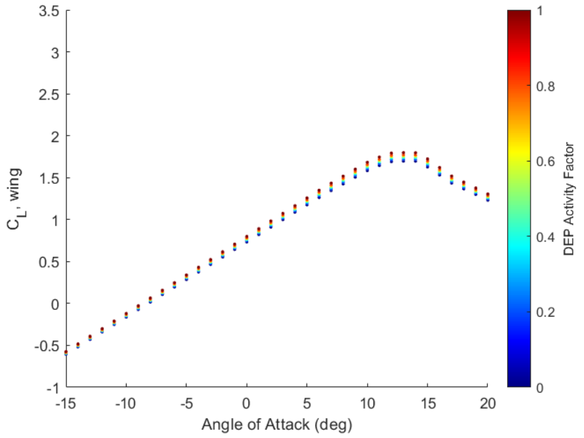

Figure 5: Wing lift coefficient as a function of angle of attack and DEP activity factor at $V = 80$ m/s, $\delta_f = 0$ deg.

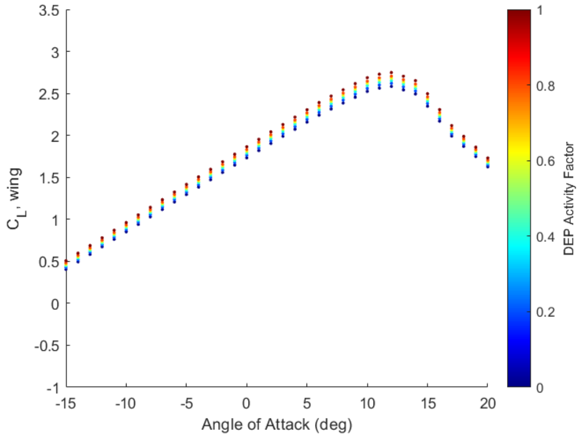

Figure 6: Wing lift coefficient as a function of angle of attack and DEP activity factor at $V = 80$ m/s, $\delta_f = 25$ deg.

compared to the cases at lower airspeeds and the linear slope of the curve is now less than 3% steeper for both flap deflections when the DEP activity factor goes from 0 to 1. This is due to the high airflow momentum that is already present at these high airspeeds and, therefore, the rotational speed limitations of the propellers lead to operation at high advance ratios, where propeller efficiency is reduced.

The high flap deflection beneficial effect to lift at low angles of attack seen before at an airspeed of 33 m/s is still verified at 80 m/s, but it is even smaller than the value obtained at low airspeed and low flap deflection. On the other hand, low flap deflections lead to similarly small changes on lift coefficient, whether the angle of attack is low or high.

This shows that at high airspeeds, the change in effective angle of attack due to the propeller slipstream is insignificant and that at high airspeed and high lift coefficient, the airflow doesn't feel the flap deflection effect.

The wing drag coefficient of the untrimmed aircraft wing for a range of angles of attack, at different airspeeds, flap deflections and DEP activity factors is shown in Figure 7 to Figure 10.

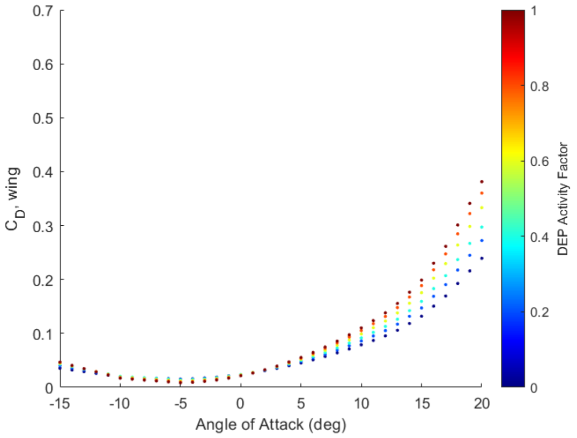

Figure 7: Wing drag coefficient as a function of angle of attack and DEP activity factor at $V = 33$ m/s, $\delta_f = 0$ deg.

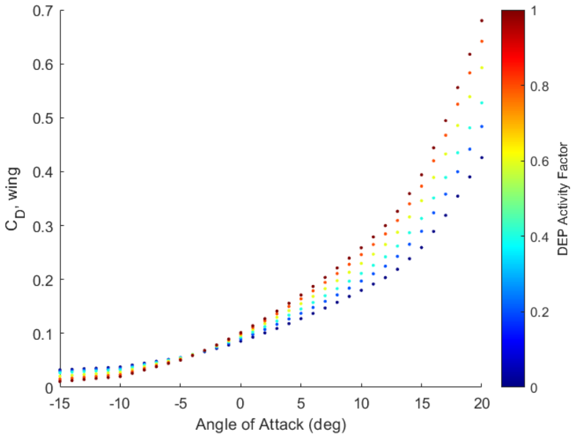

Figure 8: Wing drag coefficient as a function of angle of attack and DEP activity factor at $V = 33$ m/s, $\delta_f = 25$ deg.

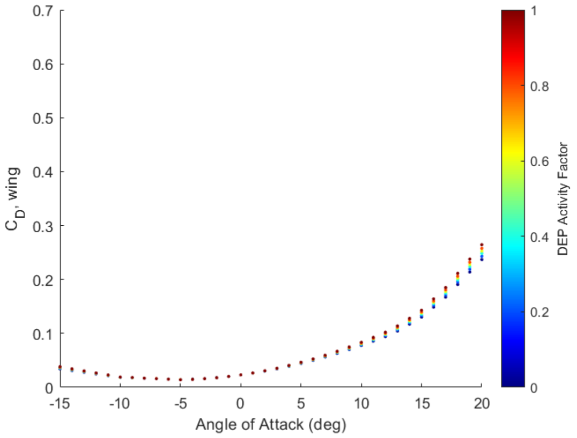

Figure 9: Wing drag coefficient as a function of angle of attack and DEP activity factor at $V = 80$ m/s, $\delta_f = 0$ deg.

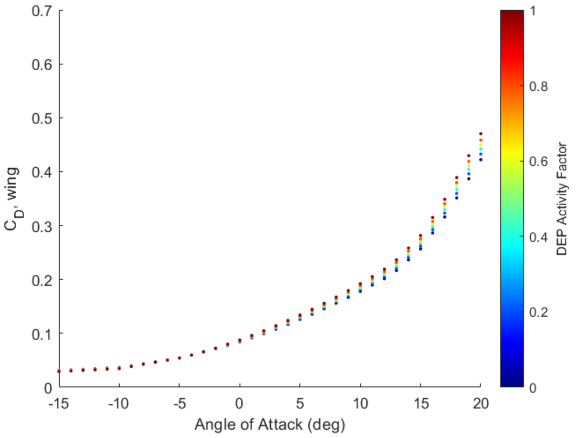

Figure 10: Wing drag coefficient as a function of angle of attack and DEP activity factor at $V = 80$ m/s, $\delta_f = 25$ deg.

One of the parameters worthy to analyze is the minimum drag angle of attack, which is seen to be always obtained at a DEP activity factor of 1 and is independent of airspeed.

For configurations with a flap deflection of 0 deg, the minimum drag angle of attack is -5 deg, whereas for a flap deflection of 25 deg, it is -15 deg. This happens because the camber effect of the flap deflection changes the lift coefficient at which the minimum drag is obtained.

Moreover, the fact that, at 0 deg flap deflection the minimum drag angle of attack is -5 deg and that increasing the DEP activity factor around this value results in a decrease of the drag coefficient, implies that the DEP installation angle of -5 deg has an important impact, as with higher slipstream axial speeds, the local airflow is more closely aligned with the wing, reducing drag. While previously it was verified that a boost in lift generation also occurs, it seems likely to be mostly due to higher dynamic pressure and what should be an increase in drag due to a stronger induced drag component is offset by a lower pressure drag due to the local angle of attack being closer to 0 deg.

At high flap deflections, this drag coefficient decrease is more noticeable, which strengthens this justification, since the performance of the flaps is much more sensitive to the flow alignment with the wing.

Identically to what was seen for the lift coefficient, the effect of DEP activity factor on drag coefficient is weaker at high airspeeds than at low airspeeds, given that the lift boost and, therefore, the added induced drag is lower.

The pitching moment coefficient of the untrimmed aircraft wing, whose reference point is at the wing leading edge, is shown in Figure 11 to Figure 14 for different airspeeds, flap deflections and DEP activity factors.

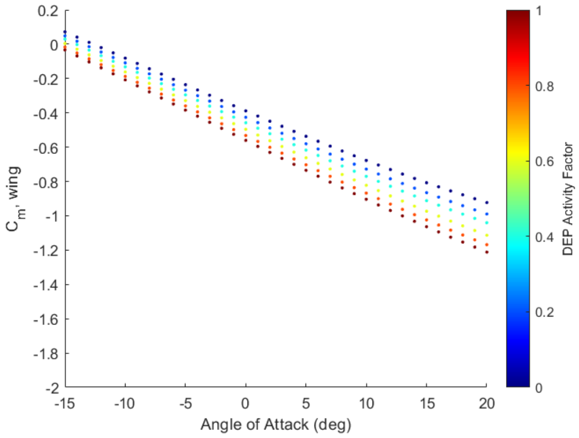

Figure 11: Wing pitching moment coefficient as a function of angle of attack and DEP activity factor at $V = 33$ m/s, $\delta_f = 0$ deg.

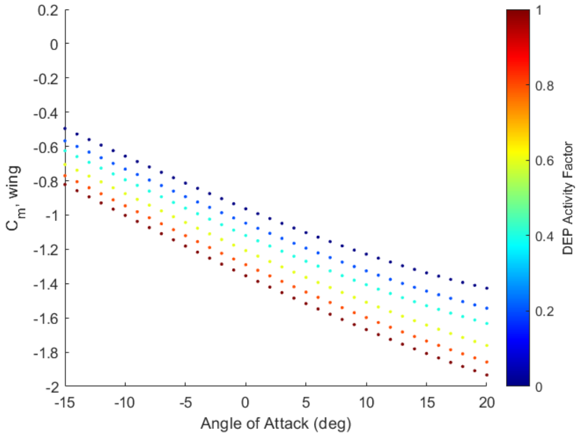

Figure 12: Wing pitching moment coefficient as a function of angle of attack and DEP activity factor at $V = 33$ m/s, $\delta_f = 25$ deg.

For all cases, an increase in DEP activity factor leads to more negative pitching moment coefficient which is due to the increase in the force generated by the wing. Additionally, it also results in more negative slopes due to the increased circulation that increases the effective wing camber.

It is also possible to see that the wing at low airspeeds has a more nose-down tendency than at high speeds, in part due to the thicker boundary layer that occurs at lower Reynolds numbers, which results in an effective wing shape with different pitching moment characteristics.

For high flap deflections, the curves shift down, having more negative pitching moment coefficients than the flap deflection of 0 deg, which can be explained by the fact that deflecting the flap brings the center of pressure closer to the rear of the wing.

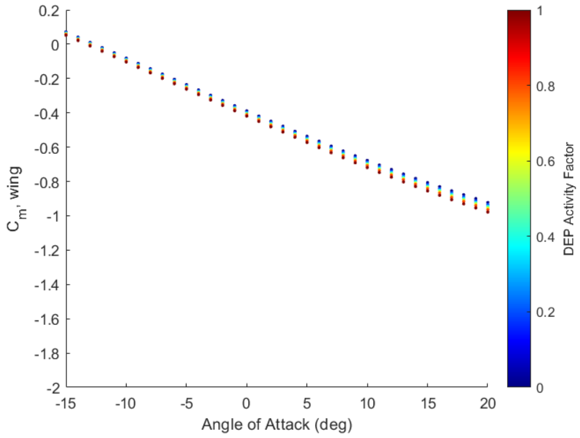

Figure 13: Wing pitching moment coefficient as a function of angle of attack and DEP activity factor at $V = 80$ m/s, $\delta_f = 0$ deg.

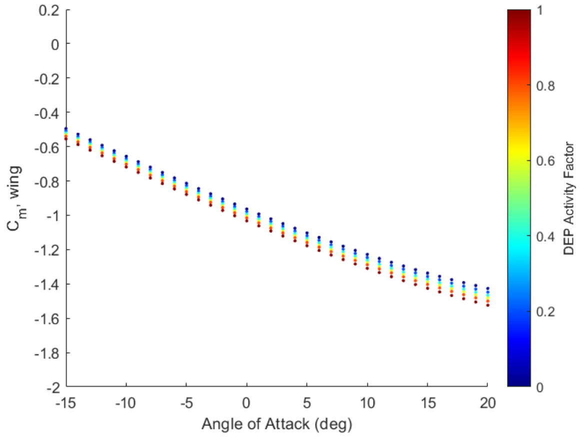

Figure 14: Wing pitching moment coefficient as a function of angle of attack and DEP activity factor at $V = 80$ m/s, $\delta_f = 25$ deg.

4.2 Trimmed Aircraft

4.2.1 Minimum Trim Airspeed

The minimum trim airspeeds and the trim control values for each of the propulsion configurations obtained for the different test cases are organized in Table 7.

Comparing the results, it is possible to verify that the minimum trim airspeed using only DEP is 11.5% lower than when only using the HTU. Furthermore, using both HTU and DEP reduces the minimum trim airspeed by just 0.6% relative to the case using only DEP.

This suggests that using DEP is essential to reducing the minimum airspeed possible at trim conditions, but coupling DEP and HTU has little effect.

One thing to notice is that the flap is always deflected at the maximum of 25 deg and the angle of attack is always around 12 deg, which are the wing trim con-

Table 7: Range of values for angle of attack, flap deflection, ruddervator deflection, half span DEP activity factor distribution and HTU activity factor at the minimum trim airspeed for the different propulsion configurations studied.

Case	Minimum Trim Airspeed (m/s)	α (deg)	δ_f (deg)	δ_r (deg)	δ_{T_i} (wing tip to root)	$\delta_{T_{\text{HTU}}}$
Only HTU	38.3	12	25	-10.1	—	0.68
Only DEP	33.9	12	25	[-16.6, -15.7]	[0, 0.21],[0.28, 0.64],[0.86, 1],1,1,1	—
HTU and DEP	33.7	[11.8, 12]	25	[-17.8, -16]	[0.04,1],1,1,1,1,1	[-0.25, -0.09]

trols for maximum lift. Furthermore, the ruddervator deflection is not being limited by its bounds.

Secondly, when it comes to the propulsion trim controls for when only the HTU is on, the trim problem has a unique solution. On the other hand, for both the case when the DEP is operating alone and when DEP is coupled with the HTU, there are multiple trim control settings for trim possible.

From this data, it's possible to conclude that the HTU only case is limited to the aerodynamic and airframe trim controls that result in the highest lift possible, with the HTU mainly counteracting the resultant drag force.

For the DEP only case, the 3 most inboard propellers are operating at the maximum activity factor of 1 and the 3 most outboard propellers operate in a lower range of activity factors, which get closer to 0 as the propellers are placed closer to the wing tip.

Coupling the DEP and the HTU brings the number of propellers operating at maximum activity factor to 5, with only the propeller near the wingtip operating at activity factors from almost 0 all the way to 1. Additionally, for this propulsion configuration, the HTU is always operating in the negative propeller thrust regime, but is never limited by its operating bounds.

If the DEP only case had all propellers operating at the maximum activity factor, it would have resulted in the desirable maximum lift generation, but, instead, more inboard propellers that affect wing sections with a larger surface area and that include flaps are prioritized. This can be explained by the need to maintain the horizontal equilibrium, since, in this propulsion configuration, further increasing the activity factors would result in a much higher aircraft thrust without the same drag increase.

Once the DEP and the HTU are coupled, almost all the propellers go to maximum activity factor for maximum lift generation, since it is now possible to counteract the excess aircraft thrust generated by the DEP with negative aircraft thrust provided by the HTU. There is the exception of the propeller that is closest to the wingtip, which has a wide operational range of activity factors for trim, some of them being very close to 0.

This result may be explained by the fact that the wing tip propeller influences a small wing surface, with half of the propeller slipstream going beyond the wing tip and, therefore, has little lift boosting potential, with any additional aircraft thrust coming from it needing to be opposed by a more negative HTU activity factor without any benefits.

In addition to that, the different DEP activity factor distributions is what leads to the multiple possible ruddervator deflections for trim. While opposing the negative pitching moment of the wing, the ruddervators generate more lift with less negative deflections when the collective DEP activity factors are slightly lower and the wing also generates slightly lower lift force.

Having said this, it is clear that the reason why coupling the HTU with the DEP is not helpful in reducing the minimum trim airspeed significantly relatively to the DEP only configuration is because the HTU acts mainly as a drag generator and, despite allowing the wing-DEP system to have a better performance, the lift force increase is insignificant for the minimum trim speed, which is inversely proportional to the square root of the maximum lift coefficient.

4.2.2 Test Case 1: HTU and DEP Active

For the aircraft to be trimmed, the lift force must be equal in magnitude to the weight and, therefore, constant.

However, in Figure 15, the airframe lift coefficient for each airspeed is not constant and has a slight negative slope. Particularly at low speeds, where trim is achieved at high angles of attack, the points form a more evident curvature downwards.

Consequently, the origin of the missing lift force has to be the propulsion system. The percentage of the total lift force that is generated by the propellers is displayed in Figure 16, where a negative percentage indicates a contribution in the direction contrary to lift.

Trimming the aircraft at low airspeeds requires higher angles of attack, whereas doing it a high airspeeds requires negative angles of attack. This indicates that the aircraft's lifting surfaces are over sized for level flight at high airspeeds over 73 m/s and that it should be possible to reduce the wing area if the aircraft design was optimized for flight at these conditions, but that would come with the cost of reducing low airspeed performance.

While trimming between -13 deg and 13 deg shows that the propulsion contribution to lift has a linearly

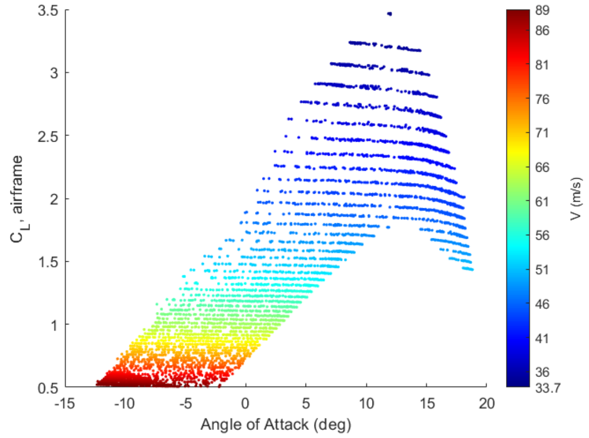

Figure 15: Trimmed airframe lift coefficient as a function of angle of attack and airspeed.

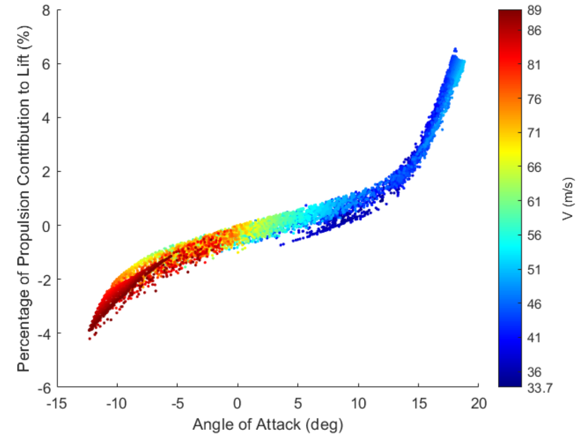

Figure 16: Percentage of total lift force generated by the propulsion system at trimmed conditions, as a function of angle of attack and airspeed.

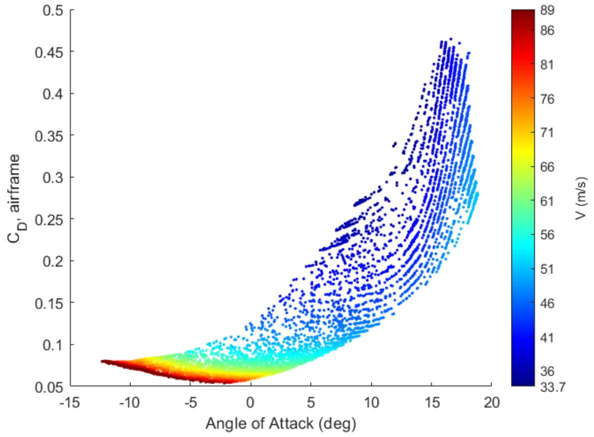

Figure 17: Trimmed airframe drag coefficient as a function of angle of attack and airspeed.

positive trend, trimming at high angles of attack above 13 deg makes this contribution to lift quickly rise and a maximum of 6.5% is achieved.

This happens because at these high angles of attack the airframe drag coefficient quickly rises, as seen in Figure 17, requiring a significant increase of propeller thrust to maintain the horizontal equilibrium, which also leads to a stronger vertical component of the propeller thrust contributing to lift.

To better understand how the different trim controls affect drag and energy consumption, in Figure 18 to Figure 21, P_{req} at trim as a function of airspeed is represented along with a color bar showing the variation in P_{elect} and the trim controls. Additionally, some reference airspeeds are represented.

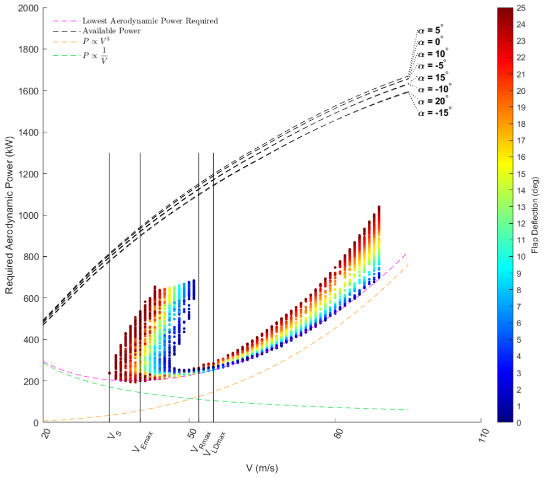

Figure 18: Required aerodynamic power and flap deflection in trim as a function of airspeed.

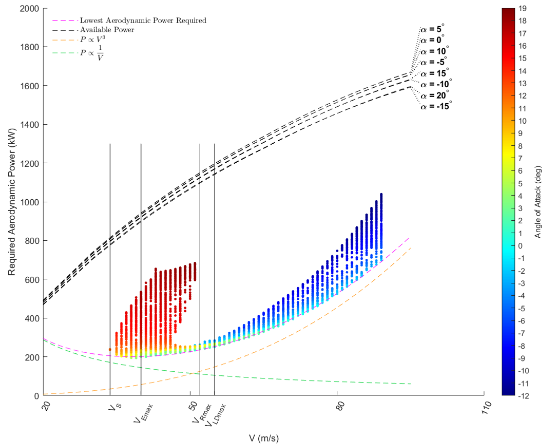

Figure 19: Required aerodynamic power and angle of attack in trim as a function of airspeed.

The first thing to note is that the trim solutions are never restricted by the available power.

In Figure 18, the flap deflection at high airspeeds goes from its minimum of 0 deg, for the lowest P_{req}, to the maximum of 25 deg for the highest P_{req}.

The range of possible P_{req} for trim becomes narrower as airspeed decreases and, at 50 m/s, trim is possible

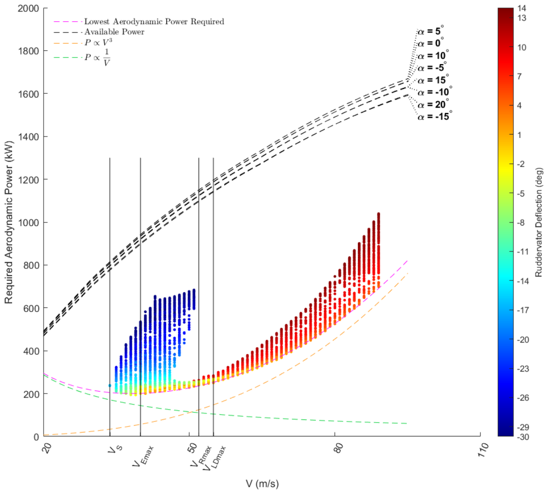

Figure 20: Required aerodynamic power and ruddervator deflection in trim as a function of airspeed.

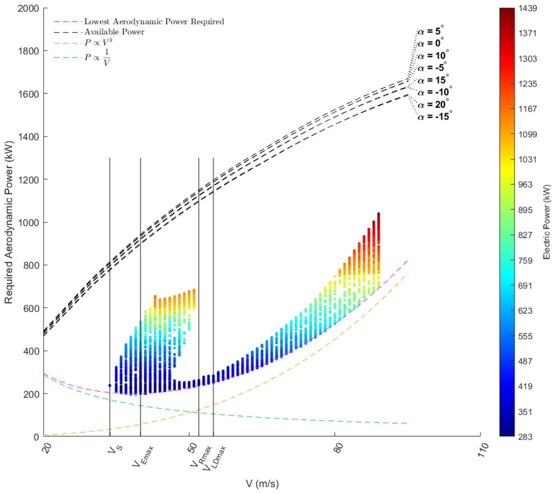

Figure 21: Required aerodynamic power and electric power consumed in trim as a function of airspeed.

for both the maximum and minimum flap deflections with roughly the same P_{req}.

Looking further into these trim points with the same P_{req}, the one with the maximum flap deflection has a negative angle of attack and the DEP system is producing more thrust force than the HTU, contrary to the trim point with the minimum flap deflection, which has a positive angle of attack and the HTU is producing more thrust than the DEP.

In practical terms, flying at negative angles of attack should be avoided for passenger comfort, and using DEP to compensate for an aerodynamically bad airframe configuration is more energetically expensive.

As airspeed decreases from 50 m/s, the lowest P_{req} is now obtained at high flap deflections up to the maximum flap deflection of 25 deg.

At low airspeeds the range of possible P_{req} for trim is now very wide, with intermediate P_{req} having a lower flap deflection than the lowest P_{req}, but increasing again for high drag trim points.

Relating the flap deflection with angle of attack, one can look at the colors of Figure 19 and compare it with the colors of Figure 18. It can be seen that for a given P_{req}, despite having different flap deflections, the angle of attack of the trim points remains approximately constant at two different regimes, a high airspeed regime, with mostly negative angles of attack, and a low airspeed regime, with positive angles of attack.

For high airspeeds, high flap deflections are coupled with very negative angles of attack and low flap deflections need slightly negative angles of attack that become slightly positive angles of attack as airspeed decreases.

On the other hand, for low airspeeds, high flap deflections for the lower P_{req} trim points generally work with a low positive angle of attack, but these become very high positive angles of attack quickly as the stall airspeed is approached. Having said that, high positive angles of attack required higher P_{req} for trimming at low airspeeds.

In what concerns the ruddervator deflection, shown in Figure 20 and comparing it with Figure 19, it has an inverse relationship with angle of attack, where negative angles of attack require positive ruddervator deflections and positive angles of attack are coupled with negative ruddervator deflections for trimming.

Focusing on Figure 21, it's possible to see that, in general, as P_{req} increases, so does P_{elect}. However, the lowest P_{req} for the different airspeeds curve doesn't coincide with the lowest P_{elect} curve. This is particularly noticeable at an airspeed of 39 m/s or 69 m/s, where there are brighter colored points below darker blue colored points.

As expected, for each airspeed there is a different combination of airframe trim controls for the lowest P_{req}, as seen in the colors of Figure 18 to Figure 20. These airframe trim controls are explicitly displayed in Figure 22 and Figure 23 where some trends can be identified.

For very low airspeeds, from the trim stall speed of 33.7 m/s to 43 m/s, the trim problem solution found by the optimizer maintains the flap deflection approximately constant at around its maximum deflection of 25 deg with rapidly decreasing angle of attack as the airspeed increases. For airspeeds between 44 m/s and 67 m/s, the angle of attack remains approximately constant, in the range around $[0, 2]$ deg, with flap deflection linearly decreasing from the maximum deflection of 25 deg to the minimum deflection of 0 deg. For airspeeds higher than 68 m/s, the flap deflection is always kept around the

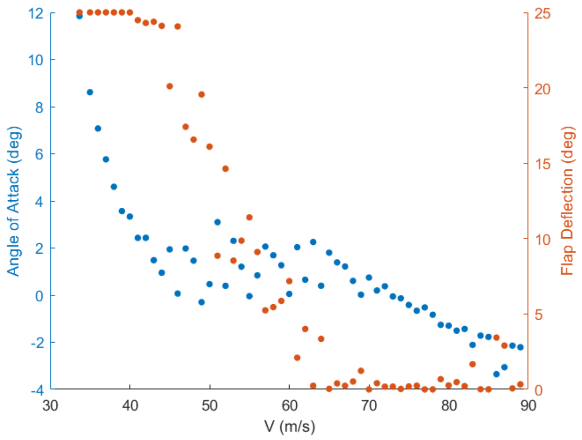

Figure 22: Angle of attack and flap deflection at the lowest required aerodynamic power in trim as a function of airspeed.

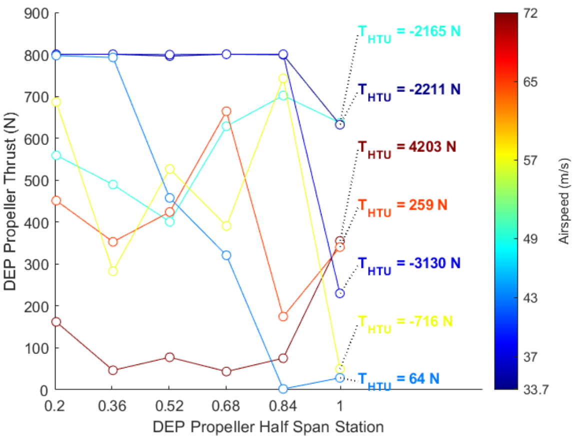

Figure 24: DEP thrust distribution and HTU thrust for the lowest required aerodynamic power at selected airspeeds.

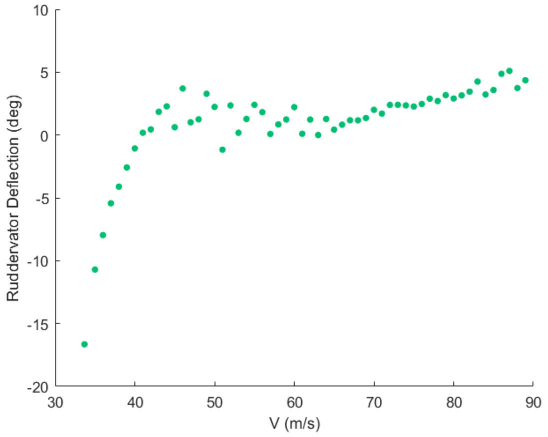

Figure 23: Ruddervator deflection at the lowest required aerodynamic power in trim as a function of airspeed.

minimum of 0 degrees, with angle of attack slowly decreasing linearly.

The ruddervator deflection maintains an inverse trend to angle of attack, for all airspeeds.

The reason behind these trim control combinations seems to be that flying at an angle of attack as close to 0 as possible, considering the other trim control bounds, is the ideal scenario for low drag generation, with flap and ruddervator deflection then adapting to this angle of attack to trim the aircraft.

By looking at Figure 24, it's possible to see why the lowest P_{req} trim points don't coincide with the lowest P_{elect} points for all given airspeeds. When there isn't an excess of aircraft thrust due to DEP, meaning that the HTU is providing a positive thrust contribution, the DEP thrust is high at the most inboard propellers and generally lower at the outboard propellers, but, at the propeller closer to the tip, there is a sudden jump in propeller thrust.

This can be explained by the fact that when the aero-propulsive interactions at the inner propellers result in the required lift generation of the wing for vertical equilibrium and there is still a need for more aircraft thrust for horizontal equilibrium, the DEP tip propeller acts more as a thrust generator than a lift booster, and the propeller slipstream airflow that engulfs the tip of the wing reduces the impact of the wing tip vortices on induced drag, therefore reducing P_{req} at a higher P_{elect} cost.

Additionally, it can be seen that, in general, the majority of the propellers, with the exception of the wing tip propeller, have a relatively constant thrust setting if the average of the peaks and vales in the spanwise thrust distribution is considered.

If one considers the lowest P_{elect} at each airspeed, Figure 25 to Figure 27 show that, compared to the lowest P_{req} trim points, there are lower ruddervator deflections, with higher angles of attack and lower flap deflections that are prioritized for lift generation, coupled with DEP producing lower propeller thrust that is then compensated by higher HTU propeller thrust. This was expected as the HTU is optimized to operate at its most efficient RPM, whereas the DEP is optimized in order to have high slipstream axial velocities.

In this case, the angle of attack always shows a somewhat linearly decreasing trend as airspeed increases.

Now analyzing the reference airspeeds compiled in Table 8, we can can compare the trim controls for the different trim points at each airspeed. The goal of this analysis is to, firstly, determine how each performance indicator is affected by the chosen propulsion system usage combination and, secondly, what the airframe trim controls are for the best performance indicators values.

It's important to remember that for parameters such as range or endurance, there are always different aero-propulsive interactions that may result in very

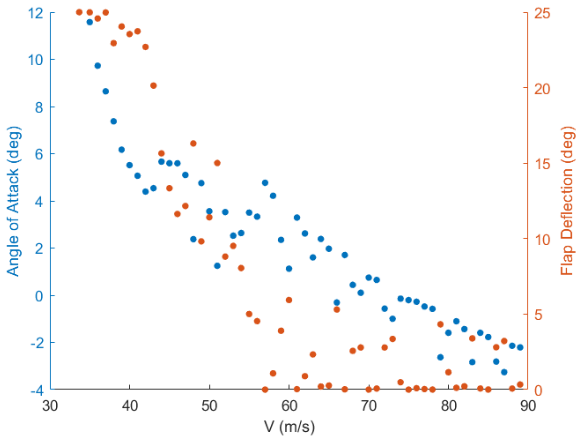

Figure 25: Angle of attack and flap deflection at the lowest electric power consumption in trim as a function of airspeed.

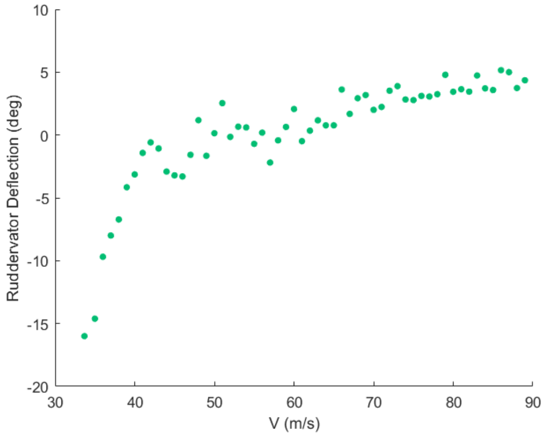

Figure 26: Ruddervator deflection at the lowest electric power consumption in trim as a function of airspeed.

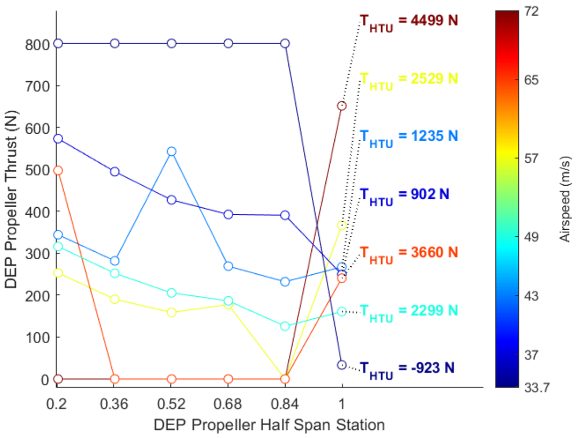

Figure 27: DEP thrust distribution and HTU thrust for the lowest electric power consumption in trim at selected airspeeds.

similar specific range and specific endurance for two or more completely different airspeeds. Therefore,

Table 8: Reference performance indicator airspeeds for the trimmed aircraft.

Parameter	Airspeed
Maximum Range	52 m/s
Maximum Endurance	40 m/s
Maximum Lift-to-Drag Ratio	55 m/s

a comparison between the best trim point for each parameter that has a neutral or positive angle of attack is compared with other trim points at that same airspeed.

Starting with the maximum range airspeed of 52 m/s, it's expected that this airspeed is the highest airspeed at which the required propeller thrust settings for the DEP and the HTU for trim, results in a very low power consumption.

This is corroborated by Table 9, where the trim controls and propeller efficiencies for the three trim points with the highest specific range found at 52 m/s are shown. The DEP propellers at trim point 1, are either turned off, consuming no electric power, or are operating at maximum efficiency, which corresponds to an advance ratio around 1.75, as seen in Figure 28.

Furthermore, trim point 1's HTU is operating with higher efficiency than trim points 2 and 3.

Additionally, the airframe trim controls show low positive angles of attack and an intermediate flap deflection, with ruddervator deflections close to 0 deg.

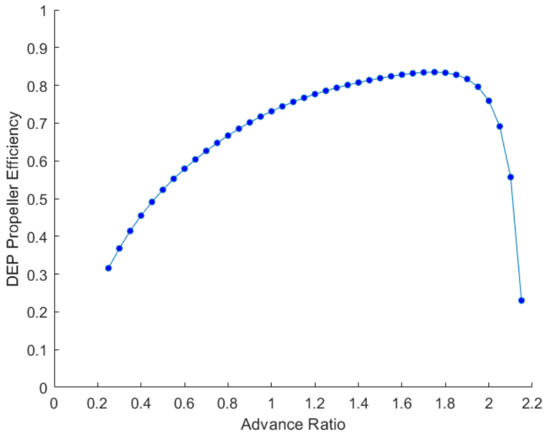

Figure 28: DEP propeller efficiency as a function of advance ratio.

When in comes to the maximum endurance trim airspeed, in Table 10 are shown the trim controls and the propellers efficiency.

Despite trim points 2 and 3 having the same P_{elect}, trim point 3 has DEP operating at a slightly lower efficiency and the HTU at a significantly lower efficiency than trim point 2, which stems for the fact that,

Table 9: Specific range, angle of attack, flap deflection and ruddervator deflection, half span DEP activity factor, propeller efficiency distributions and HTU activity factor and propeller efficiency at the maximum range airspeed for for three trim points with the highest specific range.

Trim Point	Specific Range	α (deg)	δ_f (deg)	δ_r (deg)	δ_{T_i} (wing tip to root)	$\delta_{T_{\text{HTU}}}$	DEP η (wing tip to root)	HTU η
1	0.165 m/(s.kW)	3.5	8.8	-0.2	0.38, 0, 0.31, 0.29, 0, 0.45	0.25	0.83, OFF, 0.83, 0.83, OFF, 0.83	0.86
2	0.163 m/(s.kW)	3.6	7.5	-1	0, 0, 0.32, 0.48, 0.53, 0.58	0.16	OFF, OFF, 0.83, 0.83, 0.83, 0.83	0.84
3	0.162 m/(s.kW)	2.8	9.5	0.1	0.29, 0.37, 0.78, 0.33, 0, 0.70	0.07	0.83, 0.83, 0.82, 0.83, OFF, 0.83	0.74

Table 10: Electric power consumed, angle of attack, flap deflection and ruddervator deflection, half span DEP activity factor, propeller efficiency distributions and HTU activity factor and propeller efficiency at the maximum endurance airspeed for three trim points with the highest specific endurance.

Trim Point	Electric Power	α (deg)	δ_f (deg)	δ_r (deg)	δ_{T_i} (wing tip to root)	$\delta_{T_{\text{HTU}}}$	DEP η (wing tip to root)	HTU η
1	283 kW	5.5	23.5	-3.1	0.2, 0.25, 0.38, 0.30, 0.40, 0.97	0.13	0.83, 0.83, 0.83 0.83, 0.83, 0.79	0.80
2	287 kW	5.9	24.4	-2.7	0.43, 0.08, 0.16, 0.31, 0.54, 0.56	0.21	0.83, 0.75, 0.82, 0.83, 0.82, 0.82	0.81
3	287 kW	4.3	25.0	-1.1	0.07, 0.37, 0.58, 0.74, 1, 0.41	0.02	0.73, 0.83, 0.81, 0.80 0.79, 0.83	0.49

Table 11: Lift-to-drag ratio, angle of attack, flap deflection, ruddervator deflection, half span DEP activity factor distribution and HTU activity factor at the maximum airframe lift-to-drag ratio airspeed for three trim points with the highest lift-to-drag ratio.

Trim Point	Lift-to-Drag Ratio	α (deg)	δ_f (deg)	δ_r (deg)	δ_{T_i} (wing tip to root)	$\delta_{T_{\text{HTU}}}$
1	20.6	0	11.4	2.4	0, 0.95, 0.86, 0.87, 0.97, 0.64	-0.23
2	20.3	0.9	9.9	1.6	0.90, 0.62, 0.27, 0.72, 0.73, 0.65	-0.16
3	20.2	1.3	9	1.3	0.58, 0.52, 0.61, 0.85, 0.41, 0.68	-0.12

for example, the HTU at trim point 3 is operating at a thrust setting 13 times lower than the HTU at trim point 2 and, therefore, even with a lower efficiency, the absolute wasted electric power is also lower. This remains true for the comparison between trim points 1 and 2, where the HTU at trim point 1 has a thrust setting that is half of the HTU thrust setting at trim point 2.

In this case, the angle of attack remains at low positive values, with very high flap deflections around the maximum deflection possible and slightly negative ruddervator deflections.

The maximum lift-to-drag ratio airspeed is 55 m/s, and the trim controls for the three points with the highest lift-to-drag ratio are shown in Table 11.

It is clear that low positive angle of attack coupled with an intermediate flap deflection and a low positive ruddervator deflection is required to achieve very high airframe lift-to-drag ratios.

Furthermore, very high DEP thrust settings coupled with a negative HTU thrust setting are required for trim under this condition.

4.2.3 Test Case 2: Only DEP Active

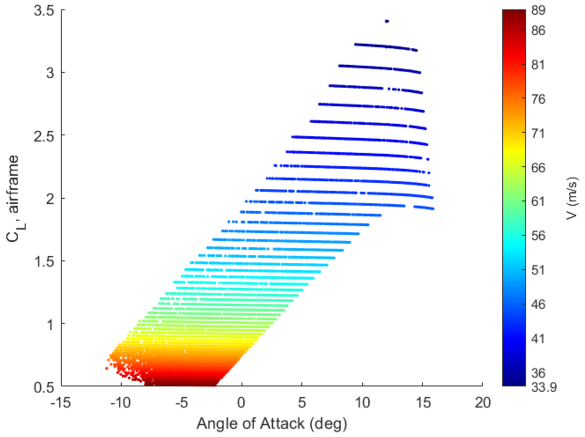

Figure 29: Trimmed airframe lift coefficient as a function of angle of attack and airspeed.

In Figure 29, the lift coefficient for the trimmed airframe using only the DEP for different airspeeds and the respective trim angle of attack is shown.

Comparing it to the trim problem using both HTU and DEP case previously analyzed, the possible angles of attack for trim are now limited to a maximum of 16 deg, the angle of attack where the curve of the airframe lift coefficient started exhibiting a more noticeable downward curvature when the HTU and DEP were coupled, being lower than the 18 deg previously seen.

Additionally, at high airspeeds, trimming is not possible at angles of attack as negative as seen before. For example, at an airspeed of 89 m/s, the aircraft was trimmable at an angle of attack of -12 deg using HTU and DEP, but can only go down to -8 deg when using only DEP.

The drag coefficient of the airframe shown in Figure 30 retains similar values as Figure 17, which is expected, since the HTU doesn't interact with the airframe. The only difference is due to the trim angle of attack range being smaller.

There is a noticeable difference when in comes to the percentage of lift force generated by the propulsion

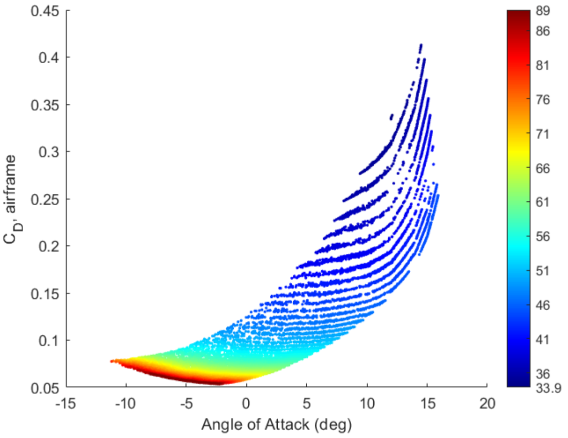

Figure 30: Trimmed airframe drag coefficient as a function of angle of attack and airspeed.

system, shown in Figure 31. At low positive trim angles of attack, between 0 and 6 deg, the range of percentages for a given angle of attack and airspeed is very narrow, whereas, when HTU was also used, it could span a percentage range width of around 1% of the total aircraft lift.

This was expected, because given the DEP propellers' installation angle of -5 deg, at an angle of attack of 5 deg, DEP has no contribution towards lift and, as the trim angle of attack increases or decreases, the DEP contribution to lift becomes more positive or negative, respectively. Additionally, for moderate to high airspeeds and a given angle of attack, when the airspeed increases, so does the DEP contribution to lift, as more propeller thrust generation is required for trim, in particular for the horizontal equilibrium. A similar explanation can be given for low airspeeds, where decreasing airspeed increases the propulsion contribution to lift, as it requires more propeller thrust generation, but now to maintain vertical equilibrium.

Moreover, for a given airspeed the propulsion contribution to lift curves are better defined with only using DEP, whereas when HTU and DEP are used, the trim points are more scattered.

Without the possibility of coupling thrust generation with the HTU, the possible variations of the trim controls in trim are more restricted, and therefore, the angle of attack and the DEP thrust value, that lead to a contribution to total aircraft lift at trim form a clearer curve.

Finally, a maximum of 2.5% of propulsion contribution to lift can be reached, less than half of that achieved when also using HTU.

The first difference relative to the DEP and HTU case is that now, when only DEP is used, the trim solutions are being constrained by the available power, as can be seen in, for example, Figure 32, for flight at low airspeeds and very high airspeeds, when there are high P_{req}. More specifically, for low airspeeds, this happens for any flap deflection at very high angles of attack and very negative ruddervator deflections and, for high airspeeds, it prevents trim from being achieved at very high flap and ruddervator deflections and very negative angles of attack.

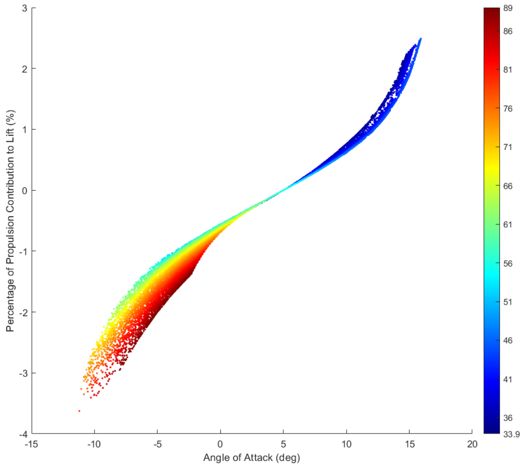

Figure 31: Percentage of lift force generated by the propulsion system at trimmed conditions, as a function of angle of attack and airspeed.

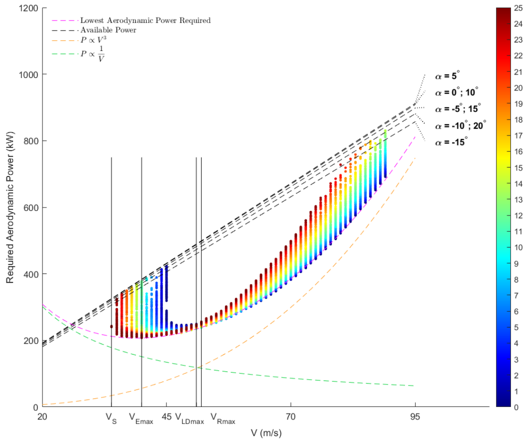

Figure 32: Required aerodynamic power and flap deflection in trim as a function of airspeed.

This shows that the reduction in the trim angle of attack range when using only DEP versus both DEP and HTU that was previously found is due to limits in available power.

The range of airspeeds where the lowest P_{req} trim points are not being constrained by flap deflection is the same in either the DEP and HTU case or the only DEP case, as seen in Figure 33. However, the angle of attack at these airspeeds stabilizes between 2 and 3 deg in comparison to between 0 and 2 deg that occurred with the HTU and DEP case.

This is because, without the HTU to help maintain horizontal equilibrium, using only DEP requires higher angles of attack at the lowest P_{req}, since the DEP lift boost effect is being limited by the requirement of maintaining the horizontal equilibrium, which doesn't allow increasing DEP thrust that would improve wing performance. Additionally, the ruddervator maintains the inverse trend behavior to angle of attack.

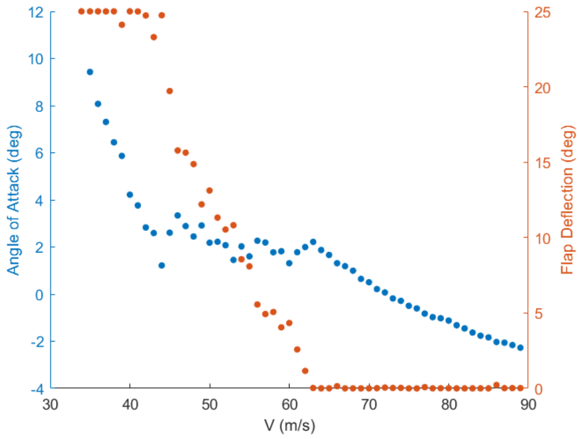

Figure 33: Flap deflection and angle of attack at the lowest required aerodynamic power in trim as a function of airspeed.

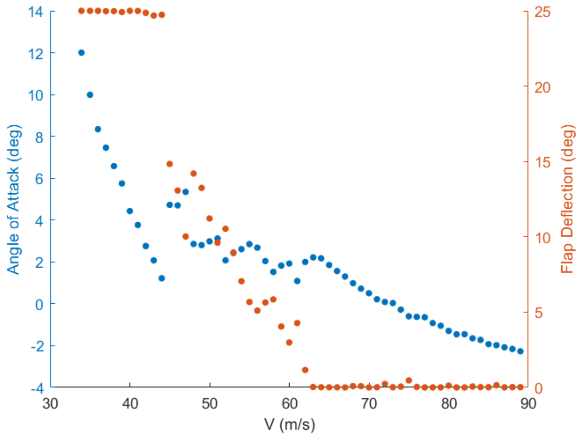

Figure 34: Angle of attack and flap deflection at the lowest electric power consumption in trim as a function of airspeed.

When it comes to the trim controls of the trim points for minimum P_{elect}, in Figure 34, there is a less chaotic distribution of points than the DEP and HTU case. This was expected, because, as also analyzed before, in the only DEP case, the thrust settings are much more correlated to P_{req} than in the DEP and HTU case, where more varied thrust settings and propeller efficiency combinations and are possible.

There is a significant offset in trim controls values from 44 m/s to 45 m/s. Up to 44 m/s, the flap is at the maximum deflection and the angle of attack decreases linearly. As also seen in the case using DEP and HTU, there is still a slight linearly decreasing trend for angles of attack between 45 m/s and 62 m/s, but it is much more reduced, as it is still influenced by P_{req}, which explains the offset on the trim controls.

The DEP half wing span thrust distribution for the lowest P_{req} and for the lowest P_{elect} at some airspeeds are shown in Figure 35 and Figure 36, respectively.

For the lowest P_{req}, the DEP thrust distribution using only DEP now shows a general linearly decreasing thrust distribution with wing spanwise station, when in the case using DEP and HTU it was constant. Also, the wing tip propeller maintains the same sudden jump in thrust setting relative to more inboard propellers seen in the previous test case.

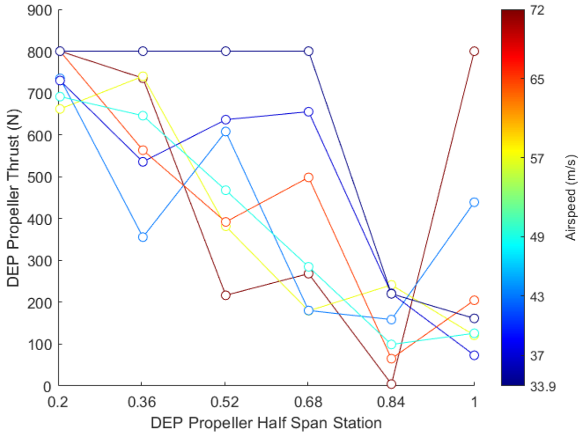

Figure 35: DEP thrust distribution for the lowest required aerodynamic power at selected airspeeds.

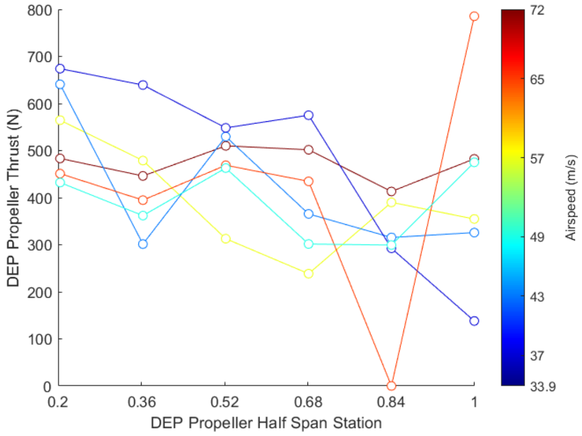

Figure 36: DEP thrust distribution for the lowest electric power consumption in trim at selected airspeeds.

However, in what concerns the lowest P_{elect}, the inboard propellers show a general constant thrust distribution with spanwise position as had already been seen in the DEP and HTU case.

Next, and as was done for the previous test case, a comparison between the best trim point for each reference airspeed is compared with other trim points at that same airspeed. The reference airspeeds' values for the only DEP active case are in Table 12.

Table 12: Reference performance indicators airspeeds for the trimmed aircraft.

Parameter	Airspeed
Maximum Range	52 m/s
Maximum Endurance	40 m/s
Maximum Lift-to-Drag Ratio	51 m/s

The first thing of note is that the maximum range airspeed and maximum endurance airspeed are the same as the HTU and DEP case. However, the maximum lift-to-drag ratio airspeed is 55 m/s when only using DEP, higher than the 51 m/s verified for the DEP and HTU case.

Beginning with the maximum range airspeed, it's possible to see that the trim points in Table 13 have low positive angles of attack with an intermediate flap deflection and ruddervator deflections close to 0 deg. Comparing it with the DEP and HTU case, we see that using only DEP results in a maximum specific range 4% larger and the angle of attack is slightly lower by 1 deg, with double the flap deflection angle and similar ruddervator deflection.

The DEP thrust distribution at maximum range airspeed doesn't showcase any clear trend for the only DEP case, but the propellers are operating at maximum efficiency.

In Table 14 with the maximum endurance airspeed trim points, the airframe has the maximum flap deflection of 25 deg, with low positive angles of attack and low negative ruddervator deflections. The minimum P_{elect} is 2% lower than the HTU and DEP case, with angles of attack lower by around 1 deg, similarly high flap deflections and slighlty less negative ruddervator deflections.

Once again, the DEP thrust distribution doesn't show a clear trend and the propellers are operating at a slightly lower efficiency than their maximum.

Now focusing on the maximum lift-to-drag ratio airspeed trim points of Table 15, low positive angles of attack that are 1 to 2 deg higher than those when using DEP and HTU are required, with similar intermediate flap deflections and very low ruddervator deflections, even closer to neutral deflection than the DEP and HTU case. The maximum lift-to-drag ratio obtained at trim using only DEP is 22% lower than when using HTU and DEP, demonstrating how important coupling HTU and DEP is for the lift-to-drag ratio. Again, the DEP thrust distribution doesn't have a clear trend.

To further analyze thrust distribution trends when only DEP is used, different thrust distributions were prescribed to the trim problem.

The comparison between the only DEP case with free thrust distribution and the ones with a rectangular, a trapezoidal and an elliptical thrust distributions, for the best trim points of each performance indicator, can be seen in Figure 37 to Figure 39. Two types of free thrust distributions are shown: one with the best absolute value for the performance indications and another with the best performance indicator value out of the free thrust distributions that don't exhibit sharp changes in thrust values, labeled as "smooth".

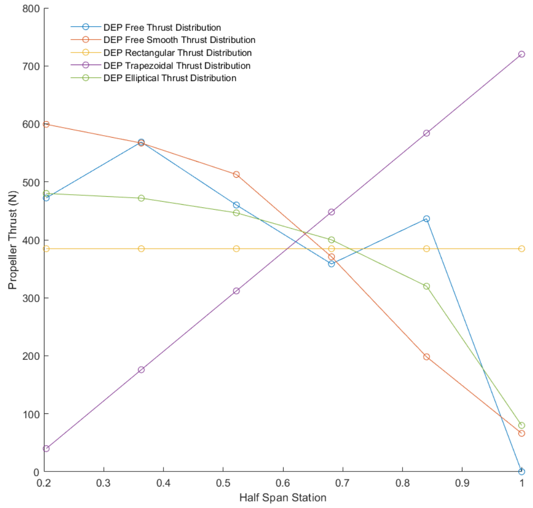

Figure 37: DEP thrust distribution of the trim points with the highest specific range, at the maximum range airspeed, for different prescribed and free thrust distribution shapes.

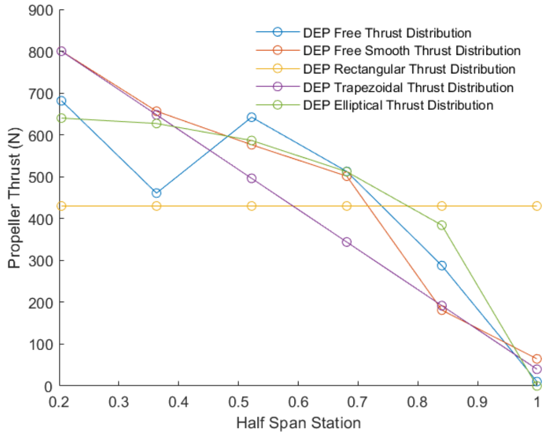

Figure 38: DEP thrust distribution of the trim points with the highest specific endurance, at the maximum endurance airspeed, for different prescribed and free thrust distribution shapes.

For all reference parameters, the free thrust distribution more closely resembles the elliptical thrust

Table 13: Specific range, angle of attack, flap deflection, ruddervator deflection and half span DEP activity factor and propeller efficiencies distributions at the maximum range airspeed for for three trim points with the highest range factor.

Trim Point	Range Factor	α (deg)	δ_f (deg)	δ_r (deg)	δ_{T_i} (wing tip to root)	DEP η (wing tip to root)
1	0.168 m/(s.kW)	2.1	10.5	0.7	0, 0.55, 0.45, 0.58, 0.71, 0.59	OFF, 0.83, 0.83, 0.83, 0.83, 0.83
2	0.167 m/(s.kW)	2.3	10.3	0.4	0.48, 0.45, 0.15, 0.72, 0.43, 0.64	0.83, 0.83, 0.77, 0.83, 0.83, 0.83
3	0.167 m/(s.kW)	2.2	10.7	0.9	0.33, 0.66, 0.60, 0.29, 0.60, 0.40	0.83, 0.83, 0.83, 0.83, 0.83, 0.83

Table 14: Electric power consumed, angle of attack, flap deflection, ruddervator deflection and half span DEP activity factor and propeller efficiencies distributions at the maximum endurance airspeed for for three trim points with the lowest electric power consumption.

Trim Point	Electric Power	α (deg)	δ_f (deg)	δ_r (deg)	δ_{T_i} (wing tip to root)	DEP η (wing tip to root)
1	277 kW	4.4	25	-1.9	0.27, 0.42, 0.37, 0.65, 0.72, 0.83	0.83, 0.83, 0.83, 0.81, 0.81, 0.80
2	278 kW	4.6	25	-1.8	0.26, 0.39, 0.58, 0.72, 0.61, 0.72	0.83, 0.83, 0.81, 0.81, 0.81, 0.80
3	279 kW	4.8	25	-2	0.43, 0.53, 0.49, 0.67, 0.46, 0.71	0.83, 0.82, 0.82, 0.81, 0.82, 0.81

Table 15: Lift-to-drag ratio, angle of attack, flap deflection and ruddervator deflection at the maximum airframe lift-to-drag ratio airspeed for for three trim points with the highest lift-to-drag ratio.

Trim Point	Lift-to-Drag Ratio	α (deg)	δ_f (deg)	δ_r (deg)	δ_{T_i} (wing tip to root)
1	16.0	2.2	11.3	0.3	0, 0.49, 0.67, 0, 0.83, 0.88
2	15.9	2.8	10.0	-0.2	0.24, 0.12, 0.81, 0.51, 0.62, 0.57
3	15.9	2.1	11.7	0.6	0.29, 0, 0.37, 0.91, 0.52, 0.76

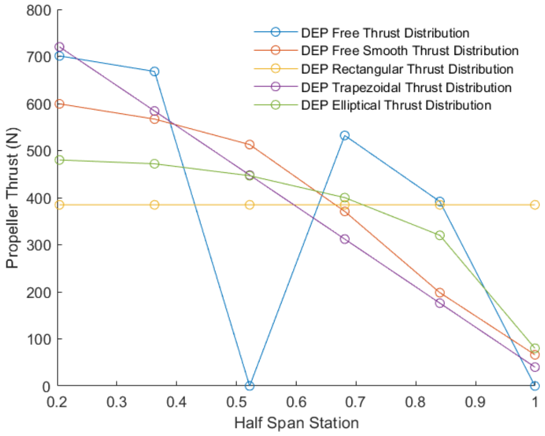

Figure 39: DEP thrust distribution of the trim points with the highest lift to drag ratio, at the maximum lift to drag ratio airspeed, for different prescribed and free thrust distribution shapes.

distribution than the trapezoidal or the rectangular one. Furthermore, looking at the free smooth thrust distribution, there are higher thrust settings in the inboard propellers than the elliptical distribution and lower ones in the more outboard propellers.

Regarding the trapezoidal thrust distribution, for the maximum range trim point, the maximum thrust is produced at the outboard propeller, whereas for the maximum endurance and maximum lift-to-drag ratio it occurs at the most inboard propeller.

By looking closely at Figure 40, it is possible to see that there are different trim points with a specific range only a little smaller that had the maximum thrust at the inboard propeller, with the same thrust values, but now flipped.

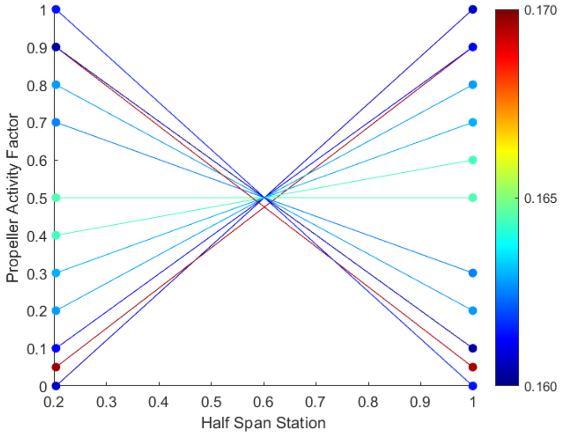

Figure 40: Possible DEP trapezoidal thrust distributions in trim conditions and respective specific range values, at the maximum range airspeed.

This indicates that trimming an aircraft for maximum range may be done with a trapezoidal thrust distribution with either the maximum thrust being at the most inboard or outboard propeller with minor differences, however, if it is at the most outboard propeller, it is likely that the effect of the propeller slipstream on the wing tip vortices is what minimally increases range.

Additionally, there are very similar trapezoidal thrust distributions that result in both the highest and the lowest specific range.

The trim condition where the lowest specific range occurs has an angle of attack of 0.7 deg and a flap deflected at 13.5 deg, whereas the trim condition with

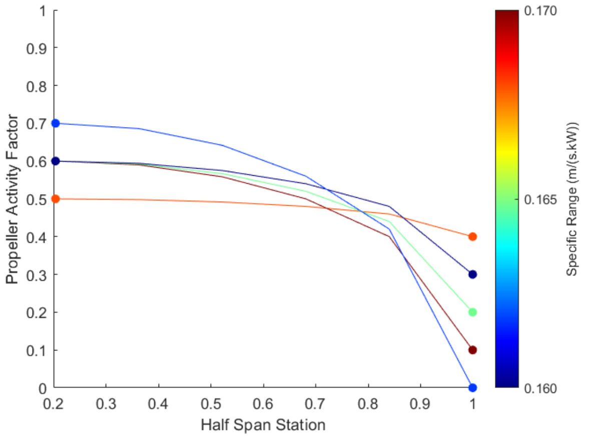

Figure 41: DEP elliptical thrust distributions in trim conditions and respective specific range values, at the maximum range airspeed.

the highest specific range has an angle of attack of 4.3 deg and a flap deflection of 5 deg.

This shows that prioritizing higher angles of attack instead of flap deflection, for similar DEP thrust distributions increases the range of the aircraft.

In Figure 41, there are the spanwise thrust distributions with a prescribed elliptical shape in trim.

Some thrust distributions have the same activity factor at the most inboard propeller, however, they have different tip propeller activity factors.

Having said that, it can be observed that the specific range decreases as the tip propeller activity factor increases, with the same most inboard propeller activity factor.

4.2.4 Test Case 3 - Only HTU Active

Similarly to what was already seen in the DEP only case, the available power is preventing the aircraft using only the HTU from being trimmed at very high angles of attack at low airspeeds and at very negative angles of attack for high airspeeds. This can be further confirmed by looking at, for example, Figure 42, where P_{req} as a function of airspeed is represented and where it is visible that for high P_{req}, in the airspeed ranges of [44, 51] m/s and [80, 89] m/s, the trim solution is being constrained by the available power.

When it comes to the propulsion contribution to the total aircraft lift shown in Figure 43, a maximum of 5.5% is obtained. This is lower than the 6.5% reached when using HTU and DEP, but higher than the 2.5% when using only DEP. Furthermore, the most negative lift contribution is -2.5%, less negative that the -4% when using HTU and DEP and than the -3.5% contribution to lift when using only DEP.

When only HTU is used, there isn't any contribution from the propulsion to lift at 0 deg of angle of attack.

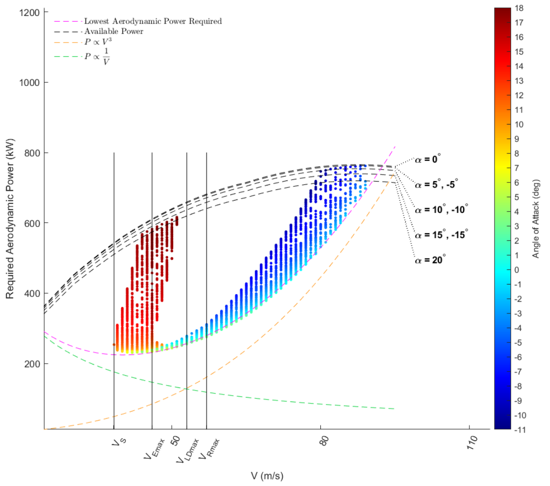

Figure 42: Required aerodynamic power and angle of attack in trim as a function of airspeed.

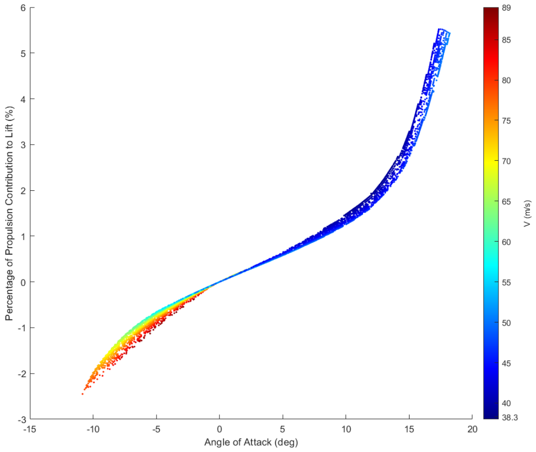

Figure 43: Percentage of total lift force generated by the propulsion system at trimmed conditions, as a function of angle of attack and airspeed.

As the trim angle of attack becomes negative, for higher airspeeds, there is a negative contribution to lift, that is concentrated into a smaller area than when compared to the only DEP case or the HTU and DEP case, as the HTU is aligned with the aircraft axis, whereas the only DEP case's DEP installation angle of -5 deg would lead to a stronger negative contribution.

To focus on the lowest P_{req} for each airspeed, the trim controls for this condition are compiled in Figure 44, Figure 45 and Figure 46.

Looking at the angle of attack and flap deflection in Figure 44, one can see that at low airspeeds, it is desirable to maintain a constant angle of attack and decrease flap deflection as airspeed increases, but for moderate to high airspeeds, maintaining a certain flap deflection for a range of airspeeds while decreas-

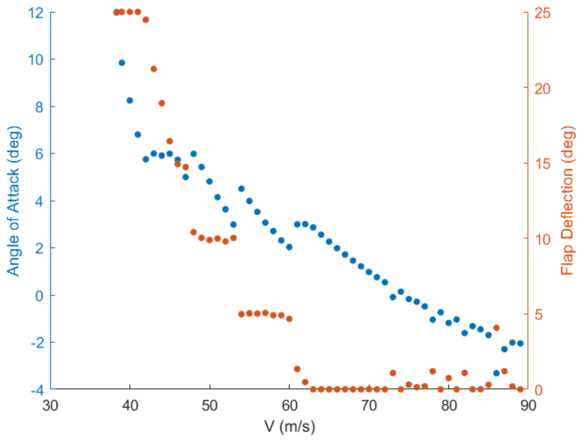

Figure 44: Angle of attack and flap deflection at the lowest required aerodynamic power in trim as a function of airspeed.

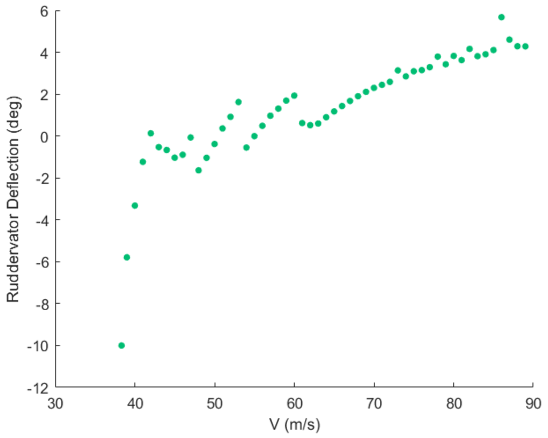

Figure 45: Ruddervator deflection at the lowest required aerodynamic power in trim as a function of airspeed.

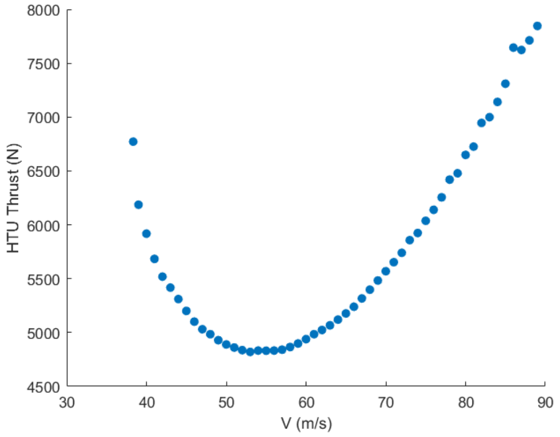

Figure 46: HTU thrust at the lowest required aerodynamic power in trim as a function of airspeed.

ing angle of attack is necessary. As already verified for other cases, the ruddervator has an inverse trend behavior to that of the angle of attack.

The HTU thrust in trim as a function of airspeed curve in Figure 46 is, as expected, similar to what the drag curve would look like, high at very low airspeeds where high angles of attack and flap deflections result in high induced drag values and also at very high airspeeds, where there is higher parasite drag.

When considering the minimum P_{elect}, the trim controls are almost identical to those obtained for the lowest P_{req}. This is expected as the HTU doesn't interact with the airframe and therefore, it's mainly constrained by the drag force of the airframe.

Analysing Table 16, the airspeeds for reference parameters show that both the maximum range and maximum endurance airspeeds for the only HTU case are higher than the DEP and HTU case, but the maximum lift-to-drag ratio airspeed is lower.

Table 16: Reference performance indicators airspeeds for the trimmed aircraft.

Parameter	Airspeed
Maximum Range	57 m/s
Maximum Endurance	46 m/s
Maximum Lift-to-Drag Ratio	53 m/s

Looking at the three best trim points for each parameter in Table 17 to Table 19, it is clear that the three points are essentially just small variations of the same trim solution.

The maximum specific range for the only HTU case is 2% lower than the DEP and HTU case, has a low positive angle of attack with low flap deflection and a rudder deflection around 1 deg. The HTU is operating at an intermediate positive thrust setting.

For the maximum endurance, there is a low positive angle of attack, intermediate flap deflection and slightly negative ruddervator deflection, close to -1 deg and the HTU is at an intermediate positive thrust setting. The maximum endurance using only HTU is 11% lower than when using DEP an HTU.

Finally, the maximum lift-to-drag ratio for the only HTU case is 27% lower than in the DEP and HTU case, and required a low positive angle of attack, intermediate flap deflection, low positive ruddervator deflection and the HTU operates at an intermediate positive thrust setting.

4.3 Equations for performance indicators and trim controls

The general equations that represent a trim control value, $C_{L,\ airframe}$ or P_{req} when given an airspeed and another trim control value are shown in Table 20.

The first thing to take into consideration is that, for a given airspeed and dependent trim control value,

Table 17: Specific range, angle of attack, flap deflection, ruddervator deflection, HTU activity factor and HTU efficiency at the maximum range airspeed for three trim points with the highest specific range.

Trim Point	Specific Range	α (deg)	δ_f (deg)	δ_r (deg)	$\delta_{T_{\mathrm{HTU}}}$	HTU η
1	0.162 m/(s.kW)	3.1	5.1	1.0	0.48	0.85
2	0.162 m/(s.kW)	3.13	4.9	0.9	0.48	0.85
3	0.162 m/(s.kW)	3.16	4.8	0.9	0.48	0.85

Table 18: Electric power consumed, angle of attack, flap deflection, ruddervator deflection, HTU activity factor and HTU efficiency at the maximum endurance airspeed for three trim points with the highest specific endurance.

Trim Point	Electric Power	α (deg)	δ_f (deg)	δ_r (deg)	$\delta_{T_{\mathrm{HTU}}}$	HTU η
1	315 kW	5.7	15	-0.8	0.51	0.81
2	315 kW	5.7	14.9	-0.9	0.51	0.81
3	315 kW	5.6	15.1	-0.8	0.51	0.81

Table 19: Lift to drag ratio, angle of attack, flap deflection, ruddervator deflection, HTU activity factor and HTU efficiency at the maximum airframe lift to drag ratio airspeed for three trim points with the highest lift to drag ratio.

Trim Point	Lift-to-Drag Ratio	α (deg)	δ_f (deg)	δ_r (deg)	$\delta_{T_{\mathrm{HTU}}}$	HTU η
1	15.1	3	10	1.6	0.48	0.84
2	15.1	3	10	1.6	0.48	0.84
3	15.1	3.1	9.7	1.4	0.48	0.84

Table 20: Least squares regression fit function types.

Independent Variable	**Dependent Variable**	**Function Type**
Low P_{req}	V, δ_f	$(a_1\delta_f + b_1)V^3 + \frac{(a_2\delta_f^2 + b_2\delta_f + c_2)}{V} + (a_3\delta_f^2 + b_3\delta_f + c_3)V$
α, with low P_{req}	V, δ_f	$\frac{a_1\delta_f + b_1}{V^2} + a_2\delta_f + a_3$

there will likely be more than one point for the independent trim control, airframe P_{req}. If these points are close to one another, it results in a good least squares regression fit.

However, when there is a wide range of independent variable values for the same dependent variables' values, the fit will not have a good correlation with the actual trim points. Therefore, when this happens, only a portion of the trim data points are used for the fitting.

The function type that gives $\alpha(V, \delta_f)$ of trim points with low P_{req} was based on the lift coefficient equation considering flap lift effectiveness [21]. If one considers the contribution of the propeller forces towards lift to be negligible, the derivation is shown in Equation 12.

$$\begin{aligned} C_L &= \frac{2W}{\rho S V^2} \iff \\ \iff \frac{2W}{\rho S V^2} &= C_{L_0} + C_{L_\alpha}\alpha + C_{L_\alpha}\tau\delta_f \iff \\ \iff \alpha &= \frac{2W}{C_{L_\alpha}\rho S V^2} - \tau\delta_f - \frac{C_{L_0}}{C_{L_\alpha}} \iff \\ \iff \alpha &= \frac{k_1}{V^2} + k_2\delta_f + k_3 \end{aligned} \tag{12}$$

When determining $\alpha(V, \delta_f)$, the dataset used are the trim points with a P_{req} that is within a margin of 10 % of the minimum P_{req} trim point at the same airspeed. The values of the coefficients of this regression fit curve are dependent on flap deflection and, to determine the expressions for the coefficients, different polynomials were tested and, by trial an error, the best one was selected for each coefficient. The regression fit and trim points are plotted in Figure 47.

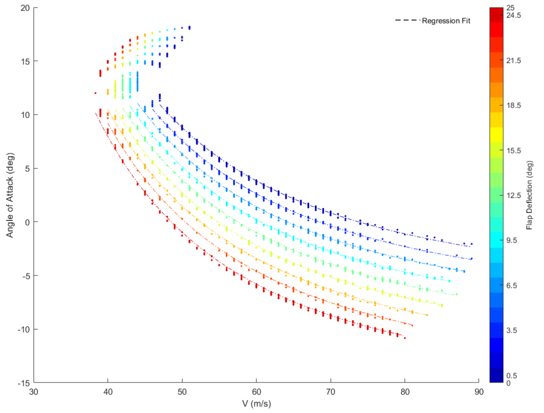

Figure 47: Least squares regression fit of angle of attack as a function of airspeed and flap deflection, when using DEP and HTU.

On the other hand, it is interesting to look at the trend of airframe C_L as a function of the angle of attack that is as close as possible to 0 deg, for which

Equation 13 can be used to express for airframe C_L only as a function of α that is the closest to 0 deg for each airspeed.

$$C_L = C_{L_0} + C_{L_\alpha} \alpha \tag{13}$$

In Figure 48, the angle of attack that is closest to 0 deg for each airspeed is represented and, in Figure 49, the airframe C_L as a function of those angles of attack is shown.

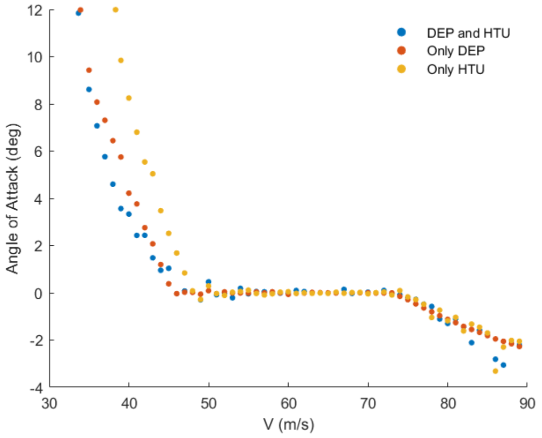

Figure 48: Angle of attack that is closest to 0 deg in trim, as a function of airspeed.

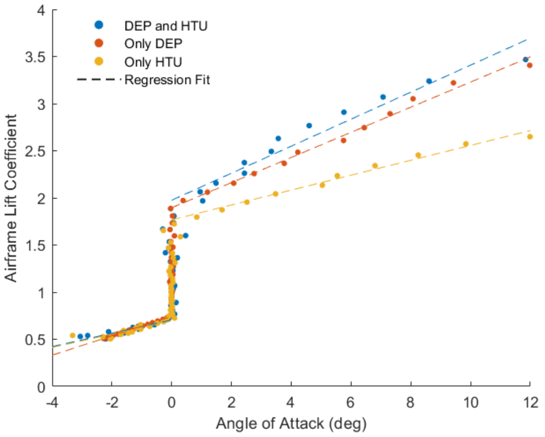

Figure 49: Least squares regression fit of airframe lift coefficient as a function of the angle of attack that is closest to 0 at each airspeed.

From the results in Figure 48, it can be seen that the aircraft can be trimmed at α close to 0 deg for airspeeds around 46 to 74 m/s. A similar result had already been seen for the trim points with minimum P_{req}, which also had neutral to low positive angles of attack at this airspeed range. For both higher and lower airspeeds than this V range, α decreases linearly as airspeed increases, which had previously been seen to be due to a flap deflection bound constraint.

Looking at Figure 49, its is possible to see that the slope of the linear trend of $C_{L,\ airframe}$ is different when comparing positive with negative angles of attack and also when comparing the three propulsion system usage combinations. The values obtained for C_{L_α} and C_{L_0} are compiled in Table 21.

The value of C_{L_α} for the lower airspeed range, that has positive angles of attack, is the highest when using DEP and HTU, closely followed by the one at the case using only DEP and the only HTU case's C_{L_α} is almost half of that of the DEP and HTU case. This is expected, as for low V, the lift boost effect of DEP at each angle of attack is very significant and is stronger when DEP is coupled with the HTU.

For high airspeeds, when HTU is available, it is the main thrust generator, and if DEP is also active, it is operating at low to moderate thrust settings. This, together with the low lift boost potential of DEP at high airspeeds, results in the same C_{L_α} for both the DEP and HTU case and the only HTU case. For the only DEP case, C_{L_α} is 45% higher than the two other test cases, mainly due to the fact that DEP is operating at high activity factors, leading to stronger aero-propulsive interactions.

When it comes to C_{L_0}, it has similar trends to what was verified for C_{L_α} and the explanations given are also valid for this parameter.

For the low $P_{req}(V,\ \delta_f)$, one can start with the parabolic drag polar assumption [22], which results in P_{req} being proportional to the sum of a cubed airspeed term and a inverse of airspeed term, as shown in Equation 14. However, at low airspeeds, where there are high angles of attack, this assumption starts breaking down, so an additional linear term was added to the function type to improve the correlation of the fit with the data points.

$$\begin{aligned} P_{req} &= \frac{1}{2}\rho V^3 S \cdot (C_{D_0} + k\ C_L^2) = \\ &= \frac{1}{2}\rho V^3 S \cdot C_{D_0} + \frac{k\ W^2}{\frac{1}{2}\rho V S} \iff \\ &\iff P_{req} = a_1 V^3 + \frac{a_2}{V} \end{aligned} \tag{14}$$

In Figure 50, the regression fit of low $P_{req}(V, \delta_f)$ is superimposed on the trim points of the HTU and DEP test case, for some independent trim control pairs. Despite only displaying one test case graph, the regression fit equations are valid for all the propulsion system usage combinations studied.

One can also look at the curve that represents the minimum P_{req} in trim and compare it with the values of P_{req} for the clean aircraft. For the test case of using DEP and HTU, these values can be compared in Table 22, resulting from a least squares regression fit of

Table 21: C_{L_α} and C_{L_0} for the trim points with the angle of attack closest to 0 deg at each airspeed, for the different propulsion system usage combinations.

	DEP and HTU			**Only DEP**			**Only HTU**		
***V* (m/s)**	[33.7, 46]	[47, 72]	[73, 89]	[33.9, 45]	[46, 73]	[74, 89]	[38.3, 48]	[49, 74]	[75,89]
C_{L_α}	0.143	–	0.071	0.133	–	0.103	0.079	–	0.071
C_{L_0}	1.975	[0.77, 1.97]	0.705	1.895	[0.75, 1.89]	0.742	1.767	[0.77, 1.72]	0.696

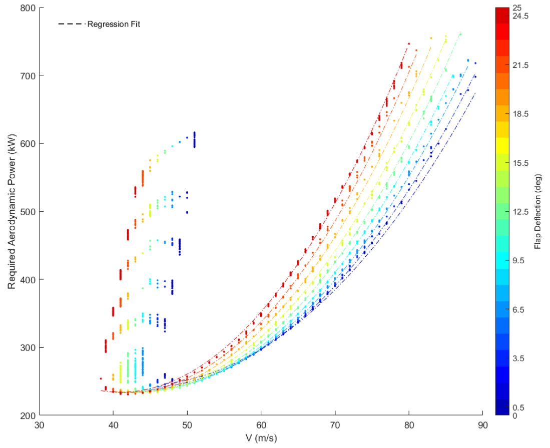

Figure 50: Least squares regression fit of low required aerodynamic power as a function of airspeed and flap deflection, when using DEP and HTU.

the data points shown in Figure 51, using Equation 14 as the equation type.

Each trim configuration has its own C_{D_0} and k value for an assumed approximation of a parabolic drag polar. If the whole airspeed envelope is considered, results show a great fit of a parabolic drag polar for these trim points with the lowest P_{req}, but now the constants $C_{D_{0},envelope}$ and $k_{envelope}$ represent mean values of their equivalents for each individual configuration.

Table 22: $C_{D_{0},envelope}$ and $k_{envelope}$ for the clean aircraft and the trimmed aircraft aerodynamically optimized configurations using DEP and HTU.

	Clean Aircraft	Trimmed Aircraft	Change
$C_{D_{0},envelope}$	$5.43 \cdot 10^{-2}$	$4.83 \cdot 10^{-2}$	-11%
$k_{envelope}$	$4.30 \cdot 10^{-3}$	$1.99 \cdot 10^{-2}$	+363%

Trimming the aircraft results in a slight reduction of $C_{D_{0},envelope}$ and a massive increase of $k_{envelope}$.

Even though this equation fit results in coefficients which are essentially independent of configuration, it's unusual for a trimmed aircraft to have a lower value of profile drag C_{D_0} than the clean aircraft configuration, since the deflection of the trim surfaces leads to higher pressure drag. However, the profile drag contribution to total drag is more significant at high airspeeds, and, since at these airspeeds the trim control surfaces have small deflections, this reduction could be due to a stronger reduction of skin friction drag due to the aero-propulsive interactions on the wing, which may result in a thinner boundary layer. Despite this possibility, it is not possible to confirm since the simulation data doesn't provide the different drag coefficient components, and is likely just a result of the least squares regression fit.

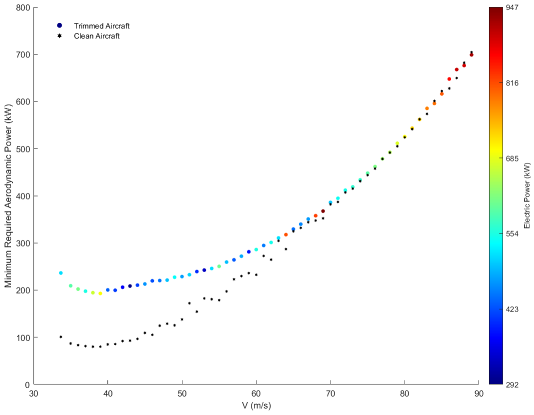

Figure 51: Minimum required aerodynamic power and respective required electric power in trim as a function of airspeed for the trimmed aircraft and the required aerodynamic power for the clean aircraft at the same angle of attack as the trimmed aircraft.

The difference in the induced drag factor $k_{envelope}$ shows that trimming the aircraft at lower speeds has a strong impact on drag. As lift generation becomes more critical with lower airspeeds, the spanwise lift distribution of the lifting surfaces, such as the wing, gets further away from the most efficient elliptical lift distribution than the clean aircraft, as shown in Figure 52, therefore leading to faster induced drag coefficient rise for the same lift coefficient variation.

The values of the coefficient of the least squares regression fit for minimum P_{req} as a function of airspeed, when using only DEP are shown in Table 23. The equivalent values for the only HTU case are also shown in Table 24.

Table 23: $C_{D_0,\ envelope}$ and $k_{envelope}$ for the clean aircraft and the trimmed aircraft aerodynamically optimized configurations using only DEP.

	Clean Aircraft	Trimmed Aircraft	Change
$C_{D_0,\ envelope}$	$5.40 \cdot 10^{-2}$	$4.75 \cdot 10^{-2}$	-12%
$k_{envelope}$	$5.80 \cdot 10^{-3}$	$2.09 \cdot 10^{-2}$	+260%

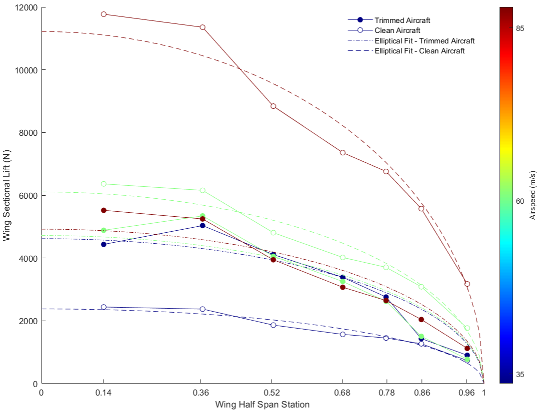

Figure 52: Spanwise lift distribution of the wing for the lowest required aerodynamic power for the trimmed aircraft and the clean aircraft at selected airspeeds.

Table 24: $C_{D_0,envelope}$ and $k_{envelope}$ for the clean aircraft and the trimmed aircraft aerodynamically optimized configurations using only HTU.

	Clean Aircraft	Trimmed Aircraft	Change
$C_{D_0,envelope}$	$5.23 \cdot 10^{-2}$	$4.74 \cdot 10^{-2}$	-8%
$k_{envelope}$	$1.10 \cdot 10^{-2}$	$2.32 \cdot 10^{-2}$	+111%

For both cases where only one of the propulsion systems is used, the trend is similar to that of the DEP and HTU case.

5 Conclusions and Recommendations

The trim condition in longitudinal flight of the Unifier C7A-HARW aircraft, with a wing leading edge distributed electric propulsion system and a tail thrust unit, was studied with the objective of performance optimization.

The effect of coupling both propulsion systems on the possible trimming strategies, as well as the effect of each individual propulsion system operating by itself, was considered and characterized in terms of performance indicators.

Results show that using a DEP system is essential to reducing the minimum trim airspeed, while coupling DEP with the HTU has an insignificant improvement in performance regarding this parameter.

The importance of DEP and uselessness of the HTU was also verified when looking at maximum endurance that always had intermediate to high flap deflections with low to intermediate positive angles of attack and low negative ruddervator deflections.

To reduce electric power consumption, trimming should be done using the HTU as the main thrust generator, when available, together with low positive angles of attack, flap and ruddervator deflections. These airframe trim controls remain valid for maximum range, with the chosen propulsion system usage combination strategy mainly affecting the flap deflection value required.

The maximum lift-to-drag ratio significantly increased when coupling the HTU with DEP, due to allowing higher DEP thrust settings. To achieve high lift-to drag ratios, low positive angles of attack and ruddervator deflections were required, with intermediate flap deflections.

An analysis on the spanwise DEP thrust distribution showed that multiple thrust distributions are possible for trimming the aircraft. Having said this, an approximately rectangular DEP spanwise thrust distribution, where the wing tip propeller provided a slightly higher thrust force than the other propellers, reduced electric power consumption.

Also, it was demonstrated that it is possible to derive analytical expressions that can be used in conceptual aircraft design and that are based on the equilibrium equations and common assumptions such as the parabolic drag polar to calculate a trim control value as a function of other trim controls.

Future research may go over the propulsion system sizing of the Unifier C7A-HARW to make coupling of HTU and DEP more beneficial to performance at low airspeeds relative to only using DEP, as it currently seems oversized for this goal. More efforts should be put into doing a similar study for aircraft with different geometries and considering, for example, engine failure scenarios and the impact on other flight conditions that include lateral movement.

Finally, trimming scenarios with other optimization objectives can be analyzed, such as ones that involve the wing bending moment in order to try to find the best DEP spanwise thrust distribution.

References

[1] Alex M. Stoll et al. “Drag Reduction Through Distributed Electric Propulsion”. In: *14th AIAA Aviation Technology, Integration, and Operations Conference* (2014). DOI: `10.2514/6.2014-2851`.

[2] Racheal M. Erhard, Matthew A. Clarke, and Juan J. Alonso. “A Low-Cost Aero-Propulsive Analysis of Distributed Electric Propulsion Aircraft”. In: *AIAA Scitech 2021 Forum* (Jan. 2021). DOI: `10.2514/6.2021-1200`.

[3] Christopher Courtin et al. “A Performance Comparison of eSTOL and eVTOL Aircraft”. In: *AIAA AVIATION 2021 FORUM* (2021). DOI: `10.2514/6.2021-3220`.

[4] Michael Schollenberger et al. "Aerodynamic interactions between distributed propellers and the wing of an electric commuter aircraft at cruise conditions". In: *CEAS Aeronautical Journal* 15 (2024), pp. 255–267. DOI: 10.1007/s13272-023-00706-6.

[5] Reynard de Vries et al. "Experimental Investigation of Over-the-Wing Propeller–Boundary-Layer Interaction". In: *AIAA Journal* 59.6 (2021), pp. 2169–2182. DOI: 10.2514/1.J059770.

[6] Justin S. Gray and Joaquim R. R. A. Martins. "Coupled aeropropulsive design optimisation of a boundary-layer ingestion propulsor". In: *The Aeronautical Journal* 123 (2019), pp. 121–137. DOI: 10.1017/aer.2018.120.

[7] Karen A. Deere et al. "Computational Analysis of a Wing Designed for the X-57 Distributed Electric Propulsion Aircraft". In: *35th AIAA Applied Aerodynamics Conference* (June 2017). DOI: 10.2514/6.2017-3923.

[8] Murilo A. Gallani, Luiz Carlos S. Góes, and Luiz Augusto R. Nerosky. "Implementation of Distributed Electric Propulsion on a General Aviation Aircraft". In: *32nd ICAS Congress* (Sept. 2021). URL: https://www.icas.org/icas_archive/ICAS2020/data/papers/ICAS2020_1025_paper.pdf.

[9] Agostino De Marco, Eugene Duke, and Jon Berndt. "A General Solution to the Aircraft Trim Problem". In: *AIAA Modeling and Simulation Technologies Conference and Exhibit*. DOI: 10.2514/6.2007-6703.

[10] Carmine Varriale and Mark Voskuijl. "A trim problem formulation for maximum control authority using the Attainable Moment Set geometry". In: *CEAS Aeronautical Journal* 13.1 (Nov. 2021), pp. 251–266. ISSN: 1869-5590. DOI: 10.1007/s13272-021-00560-4.

[11] Thymen Woldhuis, Salvatore Asaro, and Xuerui Wang. "Online Data-Driven Optimization of Aerodynamic Performance for an Unconventional Morphing Aircraft". In: *AIAA SCITECH 2025 Forum* (Jan. 2025). DOI: 10.2514/6.2025-2804.

[12] Carlo E. D. Riboldi, Stefano Cacciola, and Lorenzo Ceffa. "Studying and Optimizing the Take-Off Performance of Three-Surface Aircraft". In: *Aerospace* 9.3 (2022). ISSN: 2226-4310. DOI: 10.3390/aerospace9030139.

[13] Ben Moulton, Christian Bolander, and Douglas F. Hunsaker. "Evaluation of Stability and Controllability of the Multiple Trim Solutions for a Bio-Inspired Rotating Empennage Fighter Aircraft". In: *AIAA SCITECH 2025 Forum* (Jan. 2025). DOI: 10.2514/6.2025-0662.

[14] Dennis Keller. "Numerical study on lift augmentation via distributed propulsion for a propeller-driven regional transport aircraft in landing configuration". In: *CEAS Aeronautical Journal* (2025). DOI: 10.1007/s13272-025-00863-w.

[15] David Planas, Carsten Döll, and Philippe Pastor. "Handling Qualities of a Distributed Electric Propulsion Aircraft". In: *International Council of the Aeronautical Sciences* (2022). URL: https://hal.science/hal-03980312v1.

[16] David Planas et al. "Design optimization for improved HQ and performance of a DEP aircraft". In: *AIAA AVIATION 2023 Forum* (2023). DOI: 10.2514/6.2023-4049.

[17] UNIFIER19 Consortium. *D2.2 Final Concurrent Design Report*. Deliverable. UNIFIER19, 2021. URL: https://unifier19.eu/www.unifier19.eu/wp-content/uploads/2021/07/D2.2_Final_concurrent_design_report_Open.pdf (visited on 01/07/2025).

[18] UNIFIER19 Consortium. *D3.3.: Conceptual design report including LCA - open*. Deliverable. UNIFIER19, 2022. DOI: 10.3030/864901. (Visited on 01/07/2025).

[19] Lorenzo Trainelli et al. "Methodologies for the initial design studies of an innovative community-friendly miniliner". In: *IOP Conference Series: Materials Science and Engineering* 1024.1 (Jan. 2021), p. 012109. ISSN: 1757-899X. DOI: 10.1088/1757-899x/1024/1/012109.

[20] Johannes S.E. Soikkeli. *Unifier C7A-HARW Flight Dynamics Simulator on Github*. 2024. URL: https://github.com/soikkelij/unifier_fds.

[21] John De Young. "Theoretical Symmetric Span Loading Due to Flap Deflection for Wings of Arbitrary Plan Form at Subsonic Speeds". In: *NACA Rep. 1071* (1952). URL: https://ntrs.nasa.gov/citations/19930092116.

[22] Lance W. Traub. "Camber Effects on Minimum Power and Thrust Relations for Propeller Aircraft". In: *Journal of Aircraft* 53.1 (2016), pp. 299–304. DOI: 10.2514/1.C033491.

Appendix - Regression Fit Coefficient Values

Table 25: Values of the regression fit coefficients obtained, for each propulsion system usage combination studied.

	HTU and DEP			Only DEP			Only HTU		
Coefficient	**a**	**b**	**c**	**a**	**b**	**c**	**a**	**b**	**c**
Low P_{req} (V, δ_f)	$a_1 : 2.79 \cdot 10^{-5}$ $a_2 : -8.106$ $a_3 : 4.88 \cdot 10^{-3}$	$b_1 : 1.01 \cdot 10^{-3}$ $b_2 : 156.5$ $b_3 : -0.1716$	— $c_2 : 9.9 \cdot 10^3$ $c_3 : -1.423$	$a_1 : 2.53 \cdot 10^{-5}$ $a_2 : -6.648$ $a_3 : 4.25 \cdot 10^{-3}$	$b_1 : 1.02 \cdot 10^{-3}$ $b_2 : 114.3$ $b_3 : -0.1487$	— $c_2 : 9.7 \cdot 10^3$ $c_3 : -1.483$	$a_1 : 3.04 \cdot 10^{-5}$ $a_2 : -4.31$ $a_3 : 3.22 \cdot 10^{-3}$	$b_1 : 9.04 \cdot 10^{-4}$ $b_2 : 130.3$ $b_3 : -0.1581$	— $c_2 : 8.85 \cdot 10^3$ $c_3 : -0.7464$
α, with low P_{req}, (V, δ_f)	$a_1 : -201.7$ $a_2 : -0.3679$ $a_3 : -7.291$	$b_1 : 3.99 \cdot 10^4$ — —	— — —	$a_1 : -234.9$ $a_2 : -0.3718$ $a_3 : -7.277$	$b_1 : 3.90 \cdot 10^4$ — —	— — —	$a_1 : -41.38$ $a_2 : -0.3897$ $a_3 : -7.272$	$b_1 : 4.07 \cdot 10^4$ — —	— — —

Part III

Additional Material

4

Results

In this chapter, additional results that weren't included in the results section of Part II are presented.

4.1. Equations for performance indicators and trim controls

In addition to the low P_{req} and α with low P_{req} expressions as a function of (V, δ_f) shown in Part II, it is also possible to obtain equations to represent the remaining trim controls as a function of (V, α). All the analytical expressions found to represent trim controls and P_{req} are shown in Table 4.1 and the respective coefficients are displayed in Table 4.2.

Table 4.1: Least squares regression fit function types.

Independent Variable	**Dependent Variable**	**Function Type**
Low P_{req}	V, δ_f	$(a_1\delta_f + b_1)V^3 + \frac{(a_2\delta_f^2+b_2\delta_f+c_2)}{V} + (a_3\delta_f^2 + b_3\delta_f + c_3)V$
Low P_{req}	V, α	$(a_1V^2 + b_1V + c_1)e^{(a_2V+b_2)\alpha} + (a_3V + b_3)\alpha^2 + (a_4V^2 + b_4V + c_4)\alpha + (a_5V^2 + b_5V + c_5)$
δ_f	V, α	$(a_1V^2 + b_1V + c_1)e^{(a_2V+b_2)\alpha} + (a_3V + b_3)\alpha^2 + (a_4V^2 + b_4V + c_4)\alpha + (a_5V^2 + b_5V + c_5)$
δ_r	V, α	$(a_1V + b_1)e^{(a_2V+b_2)\alpha} + (a_4V + b_4)\alpha + (a_5V + b_5)$
α, with low P_{req}	V, δ_f	$\frac{a_1\delta_f+b_1}{V^2} + a_2\delta_f + a_3$

Table 4.2: Values of the regression fit coefficients obtained, for each propulsion system usage combination studied.

	DEP and HTU			**Only DEP**			**Only HTU**		
Coefficient	**a**	**b**	**c**	**a**	**b**	**c**	**a**	**b**	**c**
Low P_{req} (V, δ_f)	$a_1 : 2.79 \cdot 10^{-5}$ $a_2 : -8.106$ $a_3 : 4.88 \cdot 10^{-3}$	$b_1 : 1.01 \cdot 10^{-3}$ $b_2 : 156.5$ $b_3 : -0.1716$	— $c_2 : 9.9 \cdot 10^3$ $c_3 : -1.423$	$a_1 : 2.53 \cdot 10^{-5}$ $a_2 : -6.648$ $a_3 : 4.25 \cdot 10^{-3}$	$b_1 : 1.02 \cdot 10^{-3}$ $b_2 : 114.3$ $b_3 : -0.1487$	— $c_2 : 9.7 \cdot 10^3$ $c_3 : -1.483$	$a_1 : 3.04 \cdot 10^{-5}$ $a_2 : -4.31$ $a_3 : 3.22 \cdot 10^{-3}$	$b_1 : 9.04 \cdot 10^{-4}$ $b_2 : 130.3$ $b_3 : -0.1581$	— $c_2 : 8.85 \cdot 10^3$ $c_3 : -0.7464$
Low P_{req} (V, α)	$a_1 : 7.52 \cdot 10^{-4}$ $a_2 : -4.65 \cdot 10^{-3}$ $a_3 : 4.71 \cdot 10^{-2}$ $a_4 : -1.05 \cdot 10^{-3}$ $a_5 : 0.2060$	$b_1 : -5.98 \cdot 10^{-3}$ $b_2 : 0.5235$ $b_3 : -2.273$ $b_4 : 4.61 \cdot 10^{-3}$ $b_5 : -17.87$	$c_1 : 0.5687$ — — $c_4 : -0.4434$ $c_5 : 622.8$	$a_1 : 6.65 \cdot 10^{-3}$ $a_2 : -8.62 \cdot 10^{-3}$ $a_3 : 5.16 \cdot 10^{-2}$ $a_4 : 7.95 \cdot 10^{-3}$ $a_5 : 0.2078$	$b_1 : -0.2798$ $b_2 : 0.6384$ $b_3 : -2.461$ $b_4 : -0.8921$ $b_5 : -18.07$	$c_1 : 3.366$ — — $c_4 : 21.61$ $c_5 : 615.0$	$a_1 : 2.94 \cdot 10^{-3}$ $a_2 : -6.07 \cdot 10^{-3}$ $a_3 : 4.21 \cdot 10^{-2}$ $a_4 : 1.04 \cdot 10^{-3}$ $a_5 : 0.1907$	$b_1 : -0.1848$ $b_2 : 0.6048$ $b_3 : -2.116$ $b_4 : -0.3386$ $b_5 : -16.34$	$c_1 : 3.66$ — — $c_4 : 11.45$ $c_5 : 593.2$
$\delta_f(V, \alpha)$	$a_1 : -2.17 \cdot 10^{-4}$ $a_2 : -5.07 \cdot 10^{-3}$ $a_3 : 4.55 \cdot 10^{-4}$ $a_4 : 7.42 \cdot 10^{-4}$ $a_5 : 0.0140$	$b_1 : 0.0245$ $b_2 : 0.5330$ $b_3 : -0.0310$ $b_4 : -0.1034$ $b_5 : -2.522$	$c_1 : -0.5188$ — — $c_4 : 1.058$ $c_5 : 109.4$	$a_1 : 2.09 \cdot 10^{-3}$ $a_2 : 4.41 \cdot 10^{-3}$ $a_3 : 8.64 \cdot 10^{-4}$ $a_4 : 9.68 \cdot 10^{-4}$ $a_5 : 0.0131$	$b_1 : -0.2064$ $b_2 : 0.0679$ $b_3 : -0.1011$ $b_4 : -0.1495$ $b_5 : -2.464$	$c_1 : 5.406$ — — $c_4 : 2.858$ $c_5 : 108.6$	$a_1 : 5.55 \cdot 10^{-4}$ $a_2 : -3.15 \cdot 10^{-3}$ $a_3 : 1.24 \cdot 10^{-3}$ $a_4 : 1.09 \cdot 10^{-3}$ $a_5 : 0.0145$	$b_1 : -0.0522$ $b_2 : 0.4296$ $b_3 : -0.1058$ $b_4 : -0.1574$ $b_5 : -2.671$	$c_1 : 1.496$ — — $c_4 : 2.918$ $c_5 : 117.5$
$\delta_r(V, \alpha)$	$a_1 : 7.04 \cdot 10^{-3}$ $a_2 : -2.22 \cdot 10^{-3}$ $a_4 : 9.86 \cdot 10^{-4}$ $a_5 : -0.0639$	$b_1 : -0.7684$ $b_2 : 0.3018$ $b_4 : -1.087$ $b_5 : 7.532$	— — — —	$a_1 : 4.09 \cdot 10^{-3}$ $a_2 : -1.39 \cdot 10^{-3}$ $a_4 : 5.00 \cdot 10^{-3}$ $a_5 : -0.0522$	$b_1 : -0.3169$ $b_2 : 0.3419$ $b_4 : -1.354$ $b_5 : 5.858$	— — — —	$a_1 : -0.0468$ $a_2 : -3.59 \cdot 10^{-3}$ $a_4 : -5.18 \cdot 10^{-3}$ $a_5 : -0.0376$	$b_1 : 0.9373$ $b_2 : 0.3250$ $b_4 : -0.5474$ $b_5 : 8.280$	— — — —
α, with low P_{req}, (V,δ_f)	$a_1 : -201.7$ $a_2 : -0.3679$ $a_3 : -7.291$	$b_1 : 3.99 \cdot 10^4$ — —	— — —	$a_1 : -234.9$ $a_2 : -0.3718$ $a_3 : -7.277$	$b_1 : 3.90 \cdot 10^4$ — —	— — —	$a_1 : -41.38$ $a_2 : -0.3897$ $a_3 : -7.272$	$b_1 : 4.07 \cdot 10^4$ — —	— — —

The resulting fits were superimposed onto the trim points and displayed in Section 4.1.1 to Section 4.1.3. On the right of each regression fit graph, there is a graph with the correlation coefficient R^2 of each fit as a function of one of the independent variables.

The results show that when the angle of attack is used as dependent variable, the trim points form clear curves, whereas when the flap deflection is used as a dependent variable, there is a wider range of values for the independent variable, given the same dependent variable combinations.

Both P_{req} and δ_f, when expressed in terms of α for a given V, form an exponential curve at low airspeeds and a quadratic curve at moderate to high airspeeds, as seen in Figure 4.1 and Figure 4.3, for example. Therefore, the function type chosen to fit this data points is a composite curve with an exponential arc and a parabolic arc.

The values of the coefficients of this composite curve are then dependent on the airspeed and, to determine the expressions for the coefficients, different polynomials were tested and, by trial an error, the best one was selected for each coefficient.

The same procedure was applied to the ruddervator deflection, but since it demonstrates an exponential trend at low airspeeds and a linear trend at moderate to high airspeeds, for a given airspeed and range of angle of attack, a composite curve with an exponential arc and a linear segment was used, as seen in Figure 4.5.

All fits have a global coefficient of determination R^2 very close to 1. However, if one fixes a value of the independent trim control represented in the color bars, and uses the obtained equations, there is a varying value of R^2.

This is particularly evident in Figure 4.3, where low airspeed regression fits don't overlap with the trim points as well as high airspeed regression fits. The reason behind this is the lack of points in regions that are constrained by the flap deflection bounds, for example. Having said this, if the same fit function type was used, but with data divided into two distinct airspeed intervals with 51 m/s as the divider airspeed, the coefficient of determination for all individual airspeeds would be very close to 1 for both airspeed intervals, but the regression fit coefficients will be different for each airspeed interval.

Also, when δ_f is used as one of the independent variables, such as in Figure 4.8, there are some flap deflections for which there is a very low correlation coefficient R^2, which is due to the fact that the trim points for a given (V, δ_f) are more spread. This dispersion is a consequence of the simulation strategy used: the aircraft model was simulated at fixed airspeeds rather than fixed flap deflections. Consequently, the trim points had to be grouped into flap deflection "bins" with a width of 1 deg for fitting, leading to increased variance within each group.

4.1.1. Test Case 1: DEP and HTU

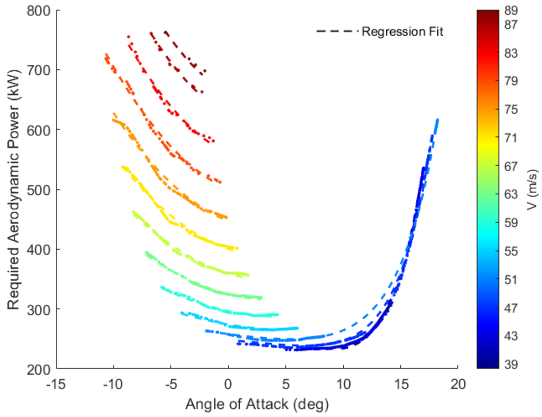

Figure 4.1: Least squares regression fit of low required aerodynamic power as a function of airspeed and angle of attack with DEP and HTU.

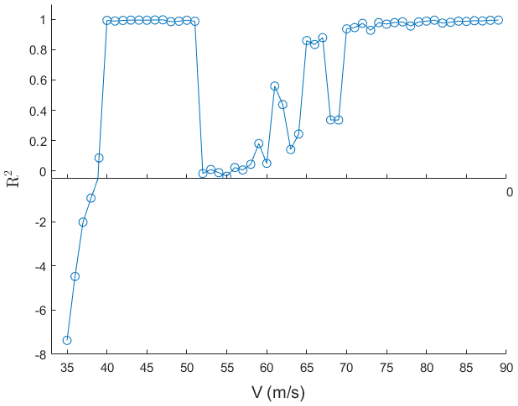

Figure 4.2: Least squares regression fit R^2 for $P_{req}(V, \alpha)$.

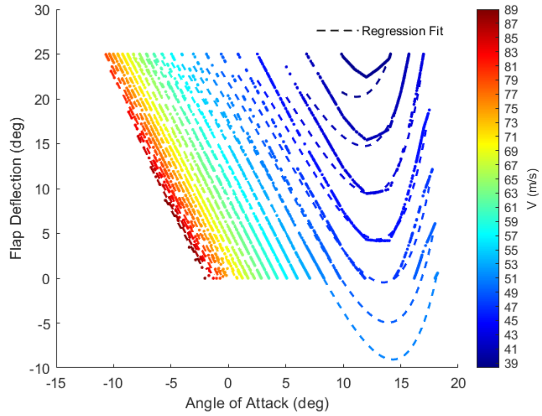

Figure 4.3: Least squares regression fit of flap deflection as a function of airspeed and angle of attack with DEP and HTU.

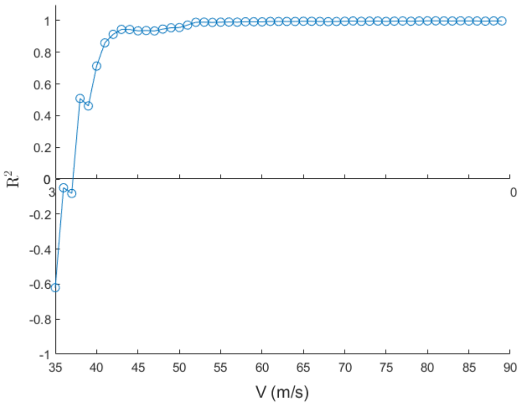

Figure 4.4: Least squares regression fit R^2 for $\delta_f(V, \alpha)$.

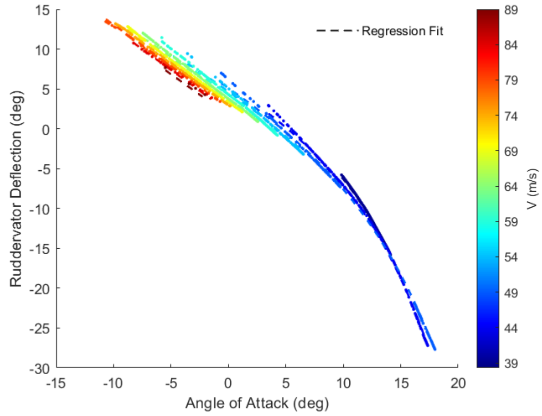

Figure 4.5: Least squares regression fit of ruddervator deflection as a function of airspeed and angle of attack with DEP and HTU.

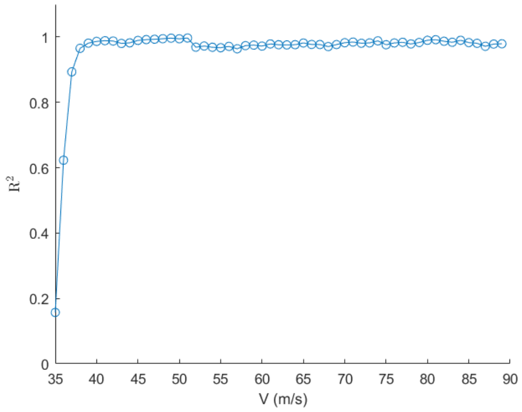

Figure 4.6: Least squares regression fit R^2 for $\delta_r(V, \alpha)$.

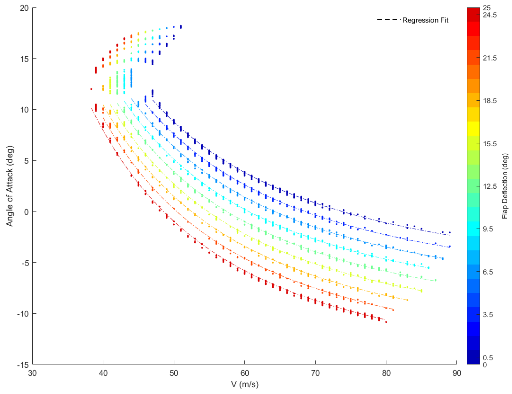

Figure 4.7: Least squares regression fit of angle of attack with low P_{req} as a function of airspeed and flap deflection with DEP and HTU.

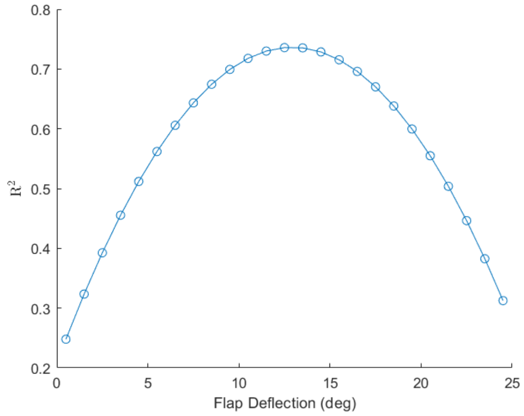

Figure 4.8: Least squares regression fit R^2 for $\alpha(V, \delta_f)$.

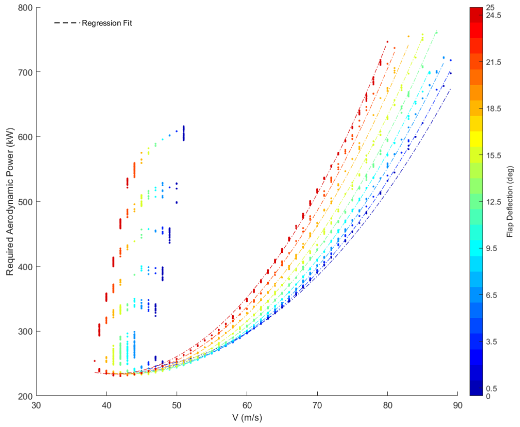

Figure 4.9: Least squares regression fit of low required aerodynamic power as a function of airspeed and flap deflection with DEP and HTU.

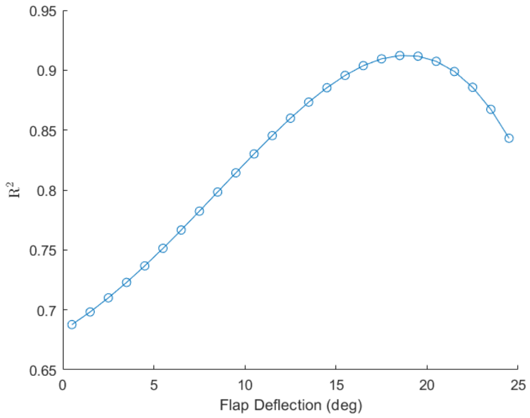

Figure 4.10: Least squares regression fit R^2 for $P_{req}(V, \delta_f)$.

4.1.2. Test Case 2: Only DEP

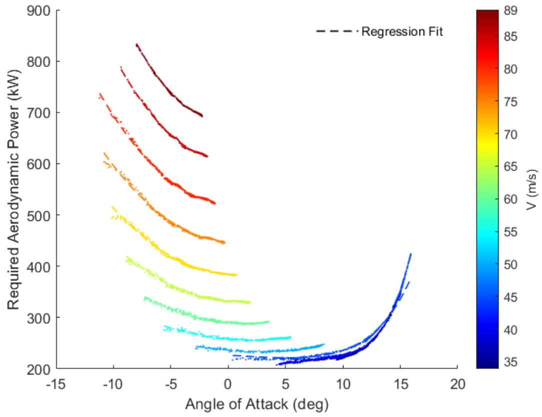

Figure 4.11: Least squares regression fit of low required aerodynamic power as a function of airspeed and angle of attack with only DEP.

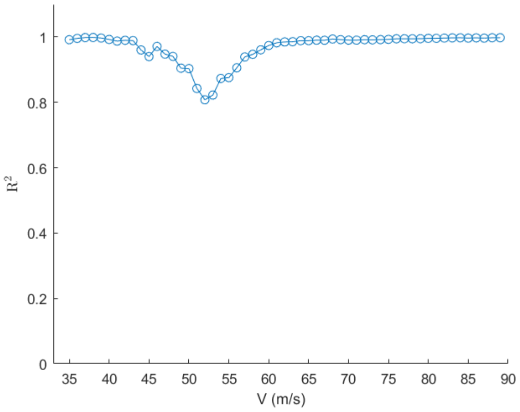

Figure 4.12: Least squares regression fit R^2 for $P_{req}(V, \alpha)$.

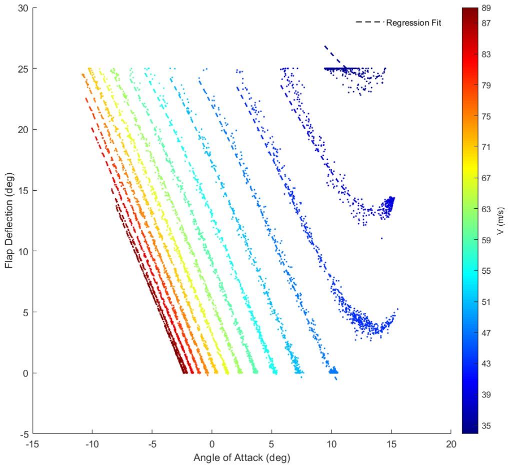

Figure 4.13: Least squares regression fit of flap deflection as a function of airspeed and angle of attack with only DEP.

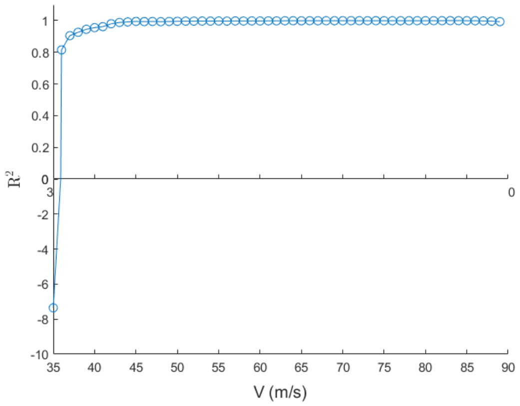

Figure 4.14: Least squares regression fit R^2 for $\delta_f(V, \alpha)$.

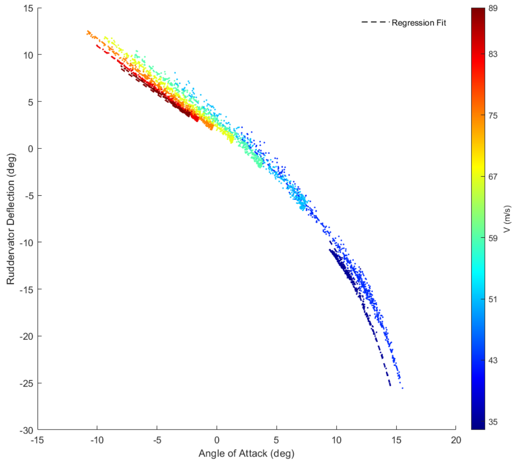

Figure 4.15: Least squares regression fit of ruddervator deflection as a function of airspeed and angle of attack with only DEP.

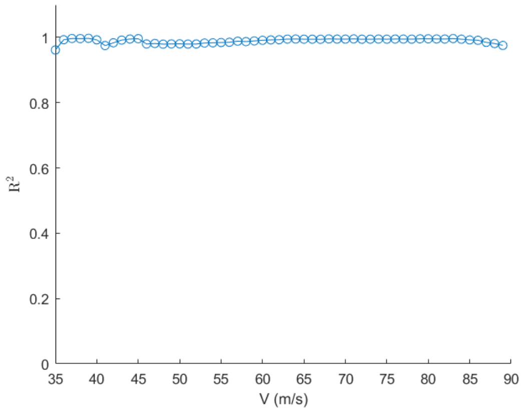

Figure 4.16: Least squares regression fit R^2 for $\delta_r(V, \alpha)$.

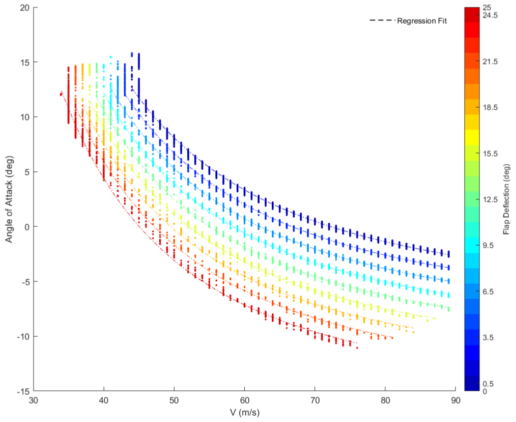

Figure 4.17: Least squares regression fit of angles of attack with low P_{req} as a function of airspeed and flap deflection with only DEP.

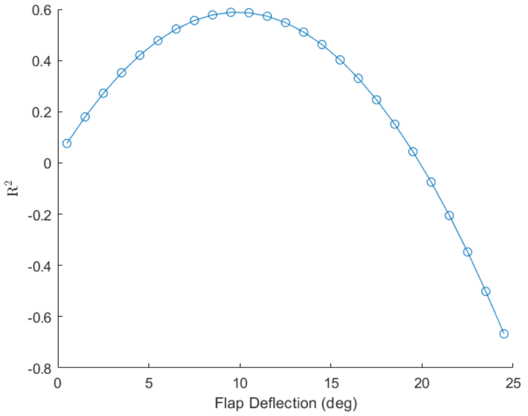

Figure 4.18: Least squares regression fit R^2 for $\alpha(V, \delta_f)$.

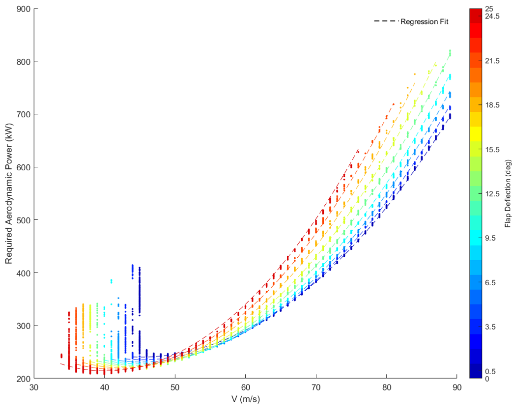

Figure 4.19: Least squares regression fit of low required aerodynamic power as a function of airspeed and flap deflection with only DEP.

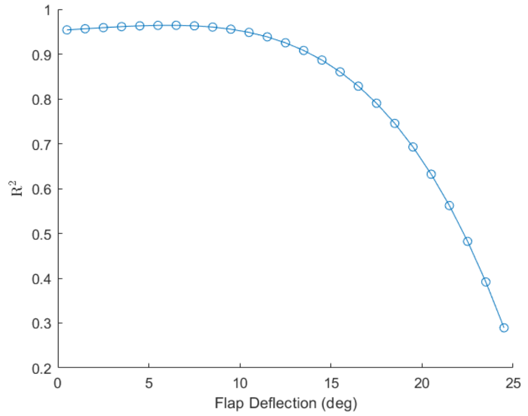

Figure 4.20: Least squares regression fit R^2 for $P_{req}(V, \delta_f)$.

4.1.3. Test Case 3: Only HTU

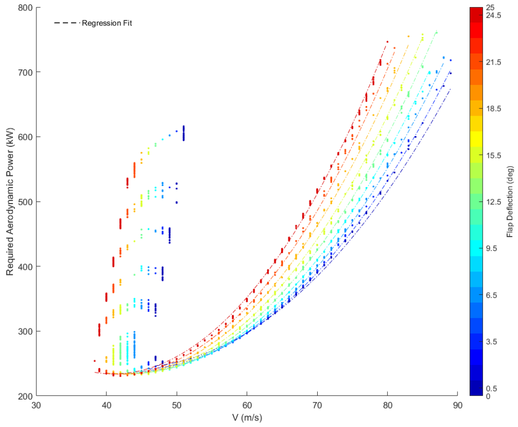

Figure 4.21: Least squares regression fit of low required aerodynamic power as a function of airspeed and flap deflection with only HTU.

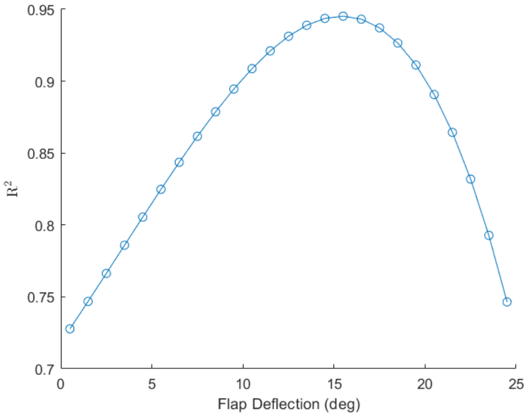

Figure 4.22: Least squares regression fit R^2 for $P_{req}(V, \delta_f)$.

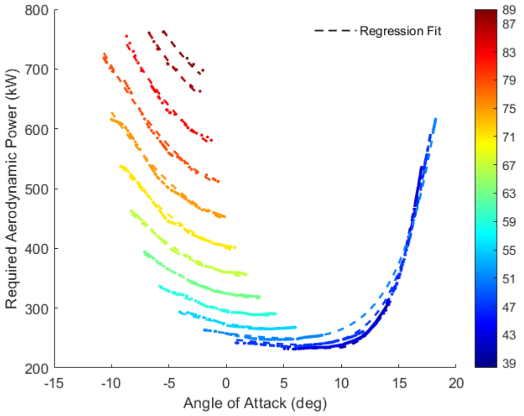

Figure 4.23: Least squares regression fit of low required aerodynamic power as a function of airspeed and angle of attack with only HTU.

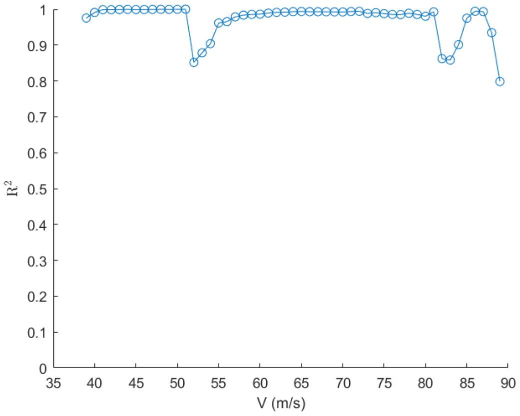

Figure 4.24: Least squares regression fit R^2 for $P_{req}(V, \alpha)$.

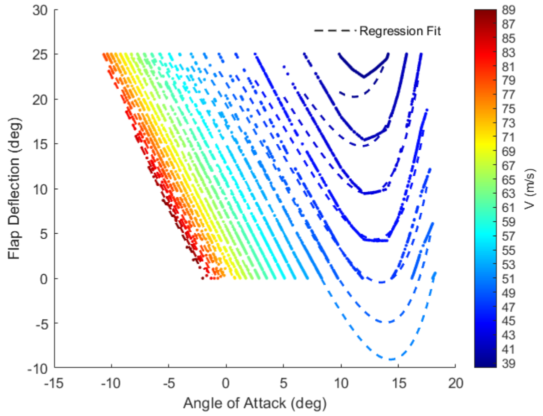

Figure 4.25: Least squares regression fit of flap deflection as a function of airspeed and angle of attack with only HTU.

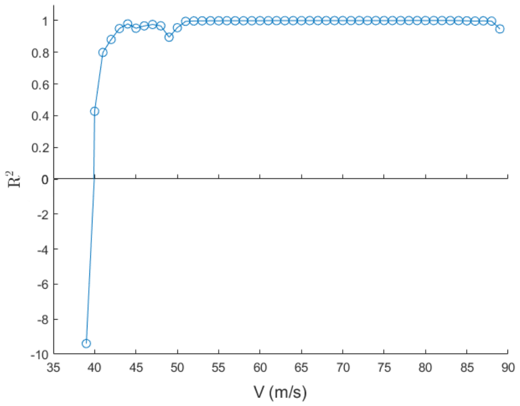

Figure 4.26: Least squares regression fit R^2 for $\delta_f(V, \alpha)$.

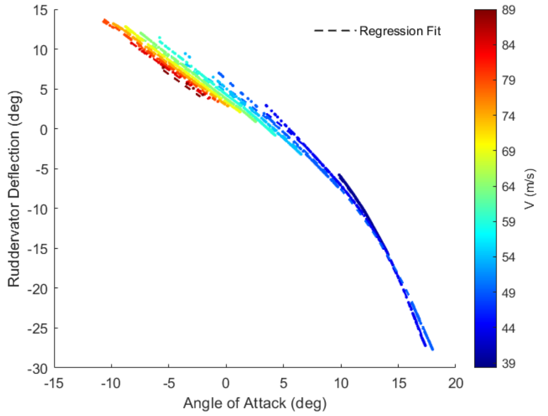

Figure 4.27: Least squares regression fit of ruddervator deflection as a function of airspeed and angle of attack with only HTU.

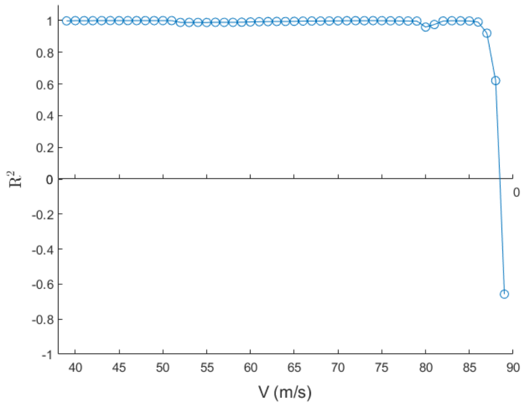

Figure 4.28: Least squares regression fit R^2 for $\delta_r(V, \alpha)$.

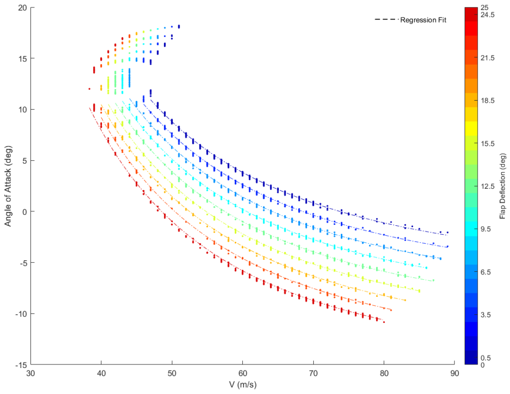

Figure 4.29: Least squares regression fit of ruddervator deflection as a function of airspeed and angle of attack with only HTU.

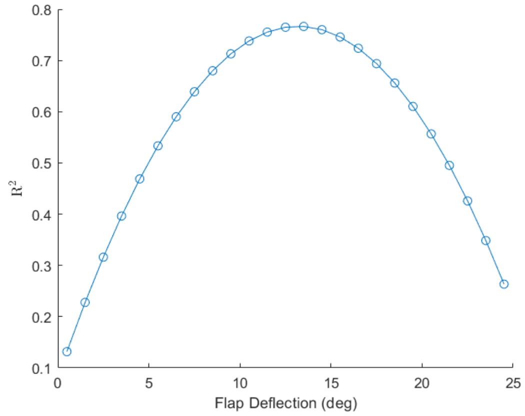

Figure 4.30: Least squares regression fit R^2 for $\alpha(V, \delta_f)$.

Part IV

Appendix

A

Extra Result Figures

In this chapter, there are additional graphs that weren't included in the results section of Part II, due to having similar observations to what had already been analyzed.

A.1. Test Case 2: Only DEP

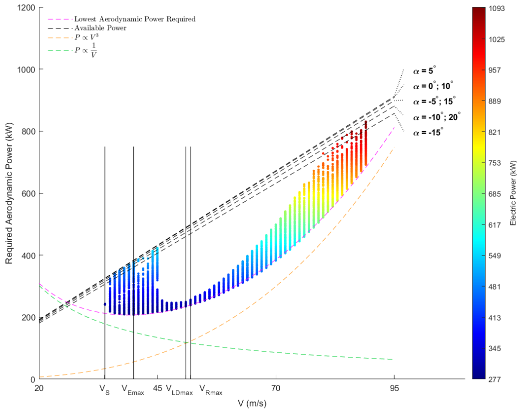

Figure A.1: Required aerodynamic power and electric power consumed in trim as a function of airspeed.

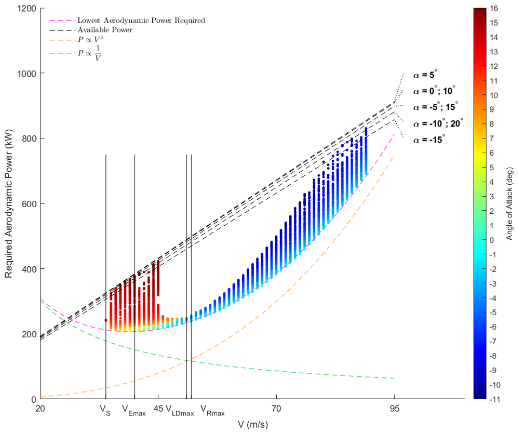

Figure A.2: Required aerodynamic power and angle of attack in trim as a function of airspeed.

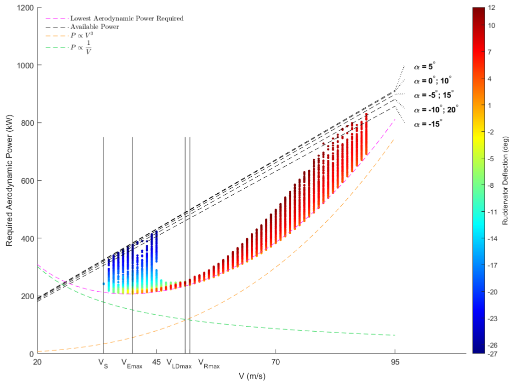

Figure A.3: Required aerodynamic power and ruddervator deflection in trim as a function of airspeed.

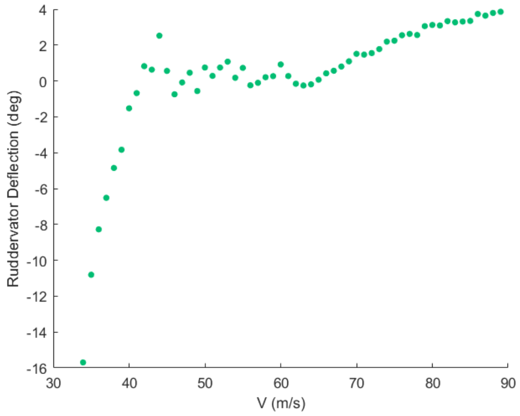

Figure A.4: Ruddervator deflection at the lowest required aerodynamic power in trim as a function of airspeed.

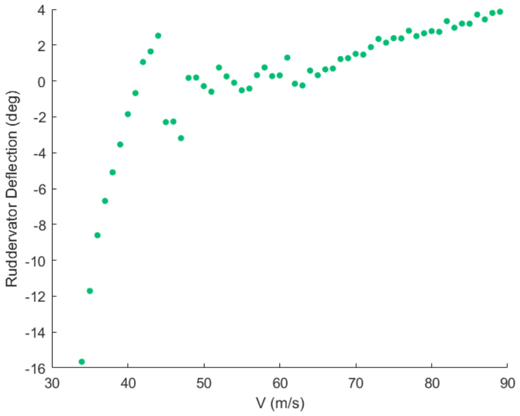

Figure A.5: Ruddervator deflection at the lowest electric power consumption in trim as a function of airspeed.

A.2. Test Case 3: Only HTU

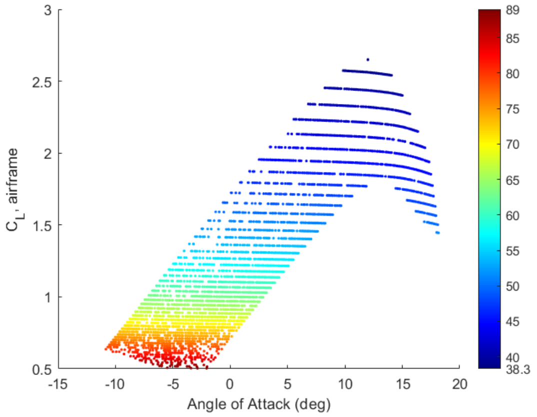

Figure A.6: Trimmed airframe lift coefficient as a function of angle of attack and airspeed.

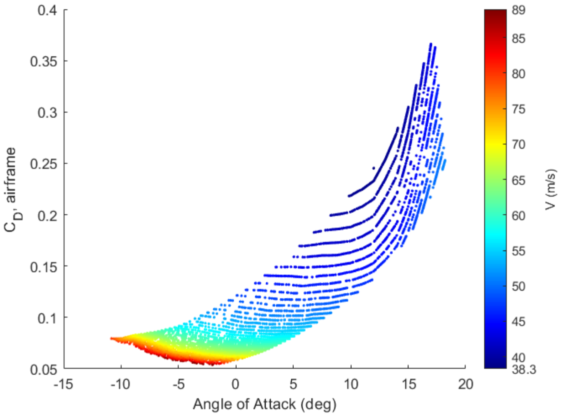

Figure A.7: Trimmed airframe drag coefficient as a function of angle of attack and airspeed.

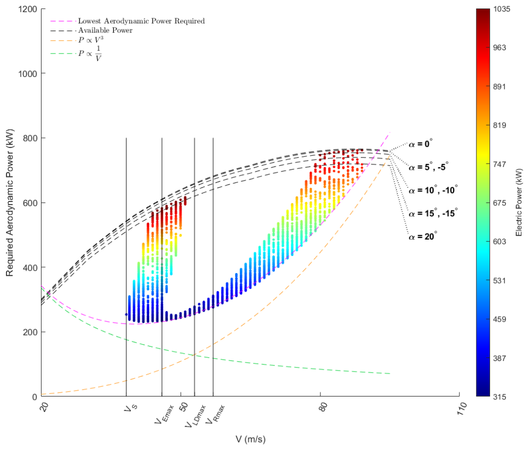

Figure A.8: Required aerodynamic power and electric power consumed in trim as a function of airspeed.

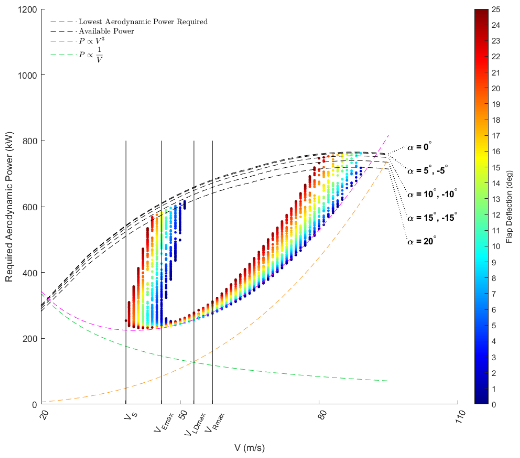

Figure A.9: Required aerodynamic power and flap deflection in trim as a function of airspeed.

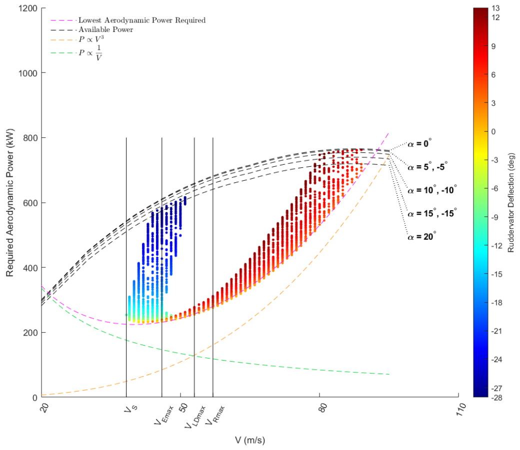

Figure A.10: Required aerodynamic power and ruddervator deflection in trim as a function of airspeed.

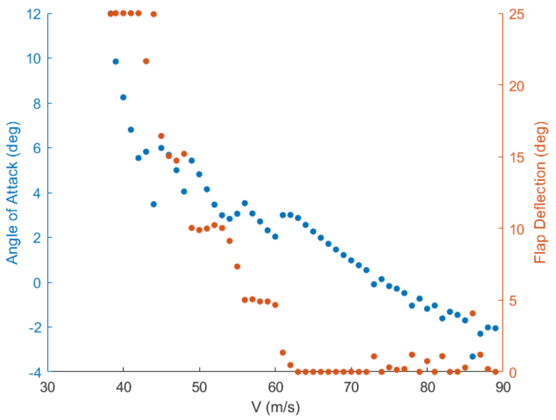

Figure A.11: Angle of attack and flap deflection at the lowest electric power consumed in trim as a function of airspeed.

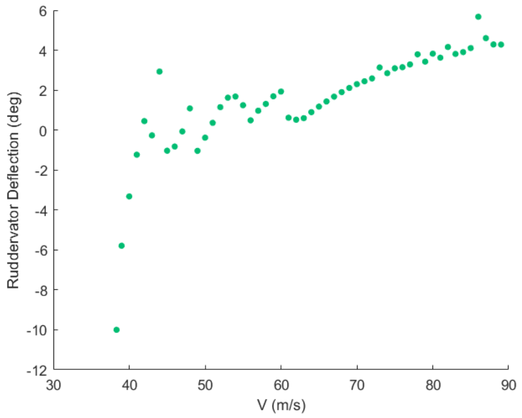

Figure A.12: Ruddervator deflection at the lowest electric power consumed in trim as a function of airspeed.

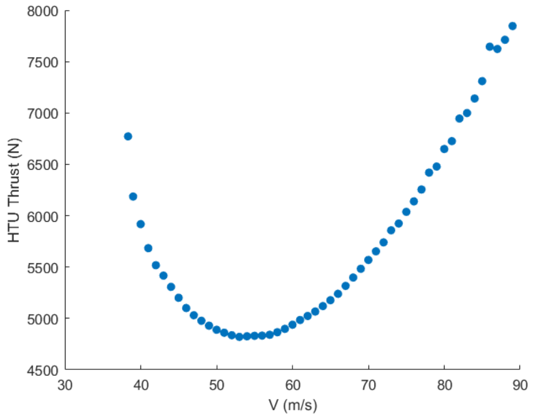

Figure A.13: HTU thrust at the lowest electric power consumed in trim as a function of airspeed.

B

Alternative Aero-Propulsive Models

In this chapter, different approaches to aero-propulsive modeling are presented, as well as some data of the failed attempt to use these approaches in this project.

B.1. Propeller Modeling

B.1.1. Momentum Theory

One of the simplest ways to model a propeller is by assuming it is a thin porous disk with an infinite number of blades that imposes a static pressure jump on the flow, therefore referred to as an actuator disk [70].

Momentum theory does a one dimensional analysis of the flow in the axial direction and assumes steady, irrotational, inviscid, incompressible and isentropic flow. A schematic of the momentum theory formulation is shown in Figure B.1.

Considering uniform flow, the principles of conservation of mass and energy are applied to the continuous streamtube that extends to infinity both upstream and downstream of the disk.

Thrust can be seen either as a pressure force acting on the actuator disk or as a consequence of the change in the momentum of the flow:

$$T = S_d \cdot \Delta p_s \tag{B.1}$$

$$T = \dot{m} \cdot (V_e - V_\infty) = \rho \cdot S_d \cdot V_d \cdot (V_e - V_\infty) \tag{B.2}$$

By applying Bernnoulli's equation, the pressure jump can be expressed as:

$$\Delta p_s = \frac{1}{2}\rho(V_e^2 - V_\infty^2) \tag{B.3}$$

Equating the two equations results in:

$$V_d = \frac{V_e + V_\infty}{2} \tag{B.4}$$

The flow velocity at the disk V_d can be described as the sum of an axial velocity increment to the freestream flow velocity:

$$V_d = V_\infty + v_a = 1 + \frac{v_a}{V_\infty} = 1 + a \tag{B.5}$$

with the axial induction factor $a = -\frac{1}{2} + \frac{1}{2} \cdot \sqrt{1 + \frac{8}{\pi} \cdot T_C}$.

The main limitations of this method is that it only allows the determination of velocity and static pressure jump at the disk location and doesn't take into account the effect of slipstream tangential and radial velocity components or blade characteristics such as geometric features, viscous effects, and interaction effects between each other, which will over predict thrust force, especially for highly loaded propellers.

Even so, this method provides a simple way to determine propeller thrust and can be useful in very early conceptual design phases. Additionally, by making the same assumptions, the downstream distribution of pressure p_s, induced axial velocity v_a and contraction ratio R_s/R_d of the streamtube can be determined by solving the Navier Stokes equations for invisicid and incompressible under an unidirectional external force [44], therefore providing a better understanding of the flow field.

$$\frac{R_s(x_a)}{R_d} = \sqrt{\frac{1+a}{1 + a \cdot (1 + \frac{x_a}{\sqrt{x_a^2 + R_d^2}})}} \tag{B.6}$$

$$p_s(x_a) = \frac{\Delta p_s}{2} \cdot (1 - \frac{x_a}{\sqrt{x_a^2 + R_d^2}}) \tag{B.7}$$

$$v_a(x_a) = a \cdot V_\infty \cdot (1 + \frac{x_a}{\sqrt{x_a^2 + R_d^2}}) \tag{B.8}$$

where $x_a = 0$ at the disk location.

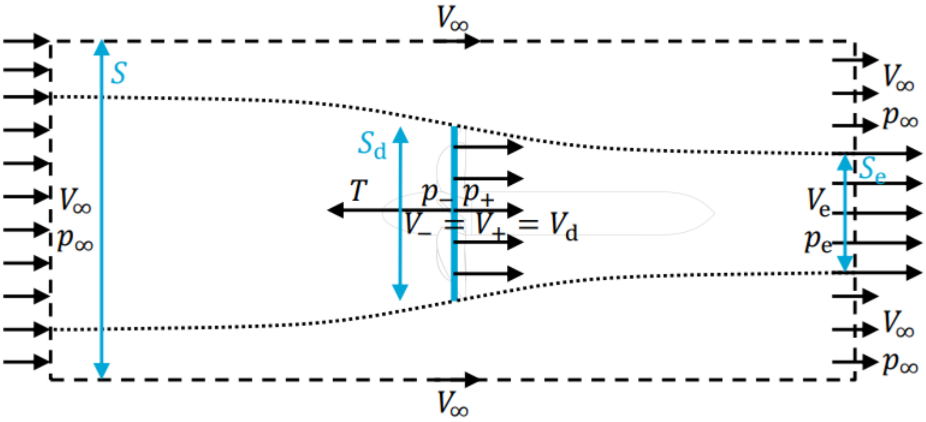

Figure B.1: Momentum theory formulation [71].

.

B.1.2. Blade Element Momentum Theory

The Blade Element Momentum Theory (BEM) combines Blade Element Theory with Momentum Theory, which results in a more robust analysis method of propellers [72].

In Blade Element Theory (BET), the propeller's blades are discretized into infinitesimal spanwise sections which can be analysed with two dimensional methods to determine the lift and drag distributions of each slice, that can then be transformed into a thrust force component, in the axial direction, and a torque component, in the tangential direction.

It follows that incorporating this perspective into the actuator disk model of momentum theory is essentially discretizing the rotor into a set of annuli and, in order to guarantee matching results with both theories, the axial induction factor must match for both methods, so an iterative process is required.

From momentum theory, Equation B.2 can be expressed as:

$$T = \frac{1}{2} \cdot \rho \cdot V_\infty^2 \cdot 2\pi R_d \cdot 4a(1-a) \tag{B.9}$$

Starting with an initial guess for both the axial a and the tangential a_t induction factors, the local angle of attack α and local relative wind speed of a blade section can be determined if the pitch angle β is known:

$$V_{rel} = \sqrt{(V_\infty(1+a))^2 + (\Omega r_i(1-a_t))^2} \tag{B.10}$$

$$\theta_b = \tan^{-1}\left(\frac{V_\infty(1+a)}{\Omega r_i(1-a_t)}\right) \tag{B.11}$$

$$\alpha = \beta - \theta_b \tag{B.12}$$

Using numerical methods or interpolating from lookup tables allows the determination of the local airfoil lift and drag coefficients, which can then be used to determine thrust and torque for each blade section:

$$dT = \frac{1}{2}\rho \cdot V_{\text{eff}}^2 \cdot c \cdot (c_l \cdot \cos\theta - c_d \cdot \sin\theta) dr_i \tag{B.13}$$

$$dQ = \frac{1}{2}\rho \cdot V_{\text{eff}}^2 \cdot c \cdot r_i \cdot (c_l \cdot \sin\theta + c_d \cdot \cos\theta) dr_i \tag{B.14}$$

Integrating Equation B.13 over the radial coordinate of each blade and multiplying by the number of blades in the propeller gives the total thrust force from BET, which is inputted into Equation B.9 to extract the equivalent axial induction factor in the momentum theory, that is used as the new guess for the convergence loop.

The advantages over momentum theory is that by taking into account their local flow characteristics and geometry, viscous effects can be included in the performance results and tangential velocities can be studied.

However, it doesn't take into spanwise blade flow, in the radial direction, which may be significant in highly loaded propellers; doesn't model hub and tip vortex effects on the induced velocities, but it is common to include Glauert's tip induction correction factor to manage this limitation; and is limited to a maximum tangential induction factor of 0.5, beyond which BEM's assumption that the slipstream angular velocity is small when compared tot he propeller rotation is not valid anymore [73].

A variant of this theory is the Unsteady Blade Element Momentum Theory (UBEMT) [74], which adds a time-variation degree of freedom to the inflow conditions. This adaptation is useful when considering unsteady aerodynamic phenomena, such as gusts, or performance variations during a manoeuvrer, which is not within the scope of this project.

B.2. Wing Modeling

B.2.1. Lifting Line Method

Proposed by Prandtl [75], the classical lifting line theory models a straight finite wing as a horseshoe vortex filament, as shown in Figure B.2, given that, for lift to be generated, circulation must be present and is representable by a bound vortex filament at the local aerodynamic centre location, which is approximately at the quarter chord location, along the wing's span and, according to Helmholtz's theorem, circulation moves with the fluid and a vortex filament cannot end within the fluid and must form a closed loop, resulting in the trailing vortices representation at the wing, and considering that the effect of the vortex that closes the loop at infinity is negligible.

The flow is assumed to be steady, inviscid, incompressible and irrotational, so it ignores any viscous effects, which constrains the feasibility of this method to low speeds and low angles of attack, where their contribution to the total force generated is reduced.

A single horseshoe vortex will result in a uniform spanwise lift distribution, so a superposition of horseshoe vortices in the same lifting line location, but with different spanwise lengths and circulation strengths is required to model a realistic wing lift distribution.

Assuming that the spanwise circulation distribution is known, the force distribution in the freestream direction is given by the Kutta–Joukowski theorem:

$$L(y) = \rho V \Gamma \tag{B.15}$$

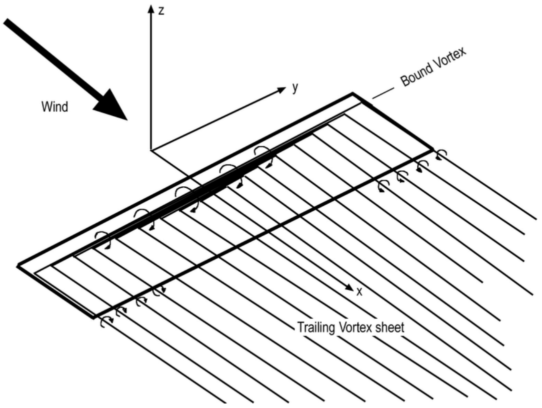

Figure B.2: Lifting line method formulation [76].

B.2.2. Vortex Lattice Method

The previous formulation of the classical lifting line theory is not adequate for swept wings, so there are some adapted implementations [77, 78] theoretically adequate for wings with a more general geometry, such as with dihedral and sweep, by modeling them with a finite number of consecutive horseshoe vortices, where the bound vortex is aligned with the quarter chord line of each wing section and the semi-infinite trailing vortices are aligned with the local flow, but the approach taken to calculate the circulation distribution is different.

This methodology is a simple vortex lattice method where there is panel discretization of the wing only in the spanwise direction, which is adequate for wings with high aspect ratios.

For a certain control point i and horseshoe vortex j, the induced velocity vector can be determined using the Biot-Savart law. Looking at Figure B.3 and considering the contributions of bound vortex and the two trailing vortices, the induced velocity strength at the control point is given by:

$$\boldsymbol{\nu}_{ij} = \frac{1}{4\pi}\left[\frac{\mathbf{u}_\infty \times \mathbf{r}_{i_2 j}}{r_{i_2 j}\left(r_{i_2 j} - \mathbf{u}_\infty \cdot \mathbf{r_{i_2 j}}\right)} + \frac{(r_{i_1 j} + r_{i_2 j})(\mathbf{r}_{i_1 j} \times \mathbf{r}_{i_2 j})}{r_{i_1 j} r_{i_2 j}\left(r_{i_1 j} r_{i_2 j} + \mathbf{r}_{i_1 j} \cdot \mathbf{r}_{i_2 j}\right)} - \frac{\mathbf{u}_\infty \times \mathbf{r}_{i_1 j}}{r_{i_1 j}\left(r_{i_1 j} - \mathbf{u}_\infty \cdot \mathbf{r}_{i_1 j}\right)}\right] \tag{B.16}$$

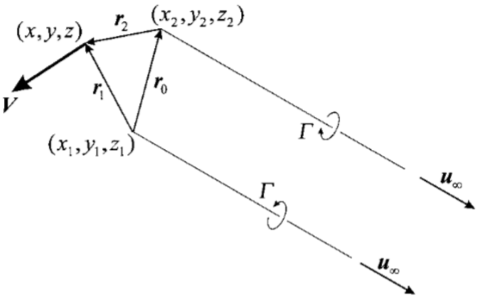

Figure B.3: Induced velocity strength calculation schematic [78].

Phillips determines the non-dimensional circulation strength G_i distribution for each horseshoe vortex, by compiling the full problem into matrix form and using Newton's method to solve the resultant non-linear equation system.

On the left side of Equation B.17, there is the lift force generated in a differential section of the lifting surface located at a chosen control point i, which is placed in the bound vortex, and, in the right side, is the equivalent lift force at the same differential section of the wing, but through the local airfoil section aerodynamic characteristics, obtained using other analytical or empirical methods and needs to be known a priori.

$$\rho\Gamma_i\left(\mathbf{V}_\infty + \sum_{j=1}^{N}\frac{\Gamma_j}{\overline{c}_j}\boldsymbol{\nu}_{ji}\right) \times \mathbf{d}\ell_i = \frac{1}{2}\rho V_\infty^2 C_{\ell_i}(\alpha_i) dA_i \tag{B.17}$$

This can then be non-dimensionalized to:

$$2\left|\left(\boldsymbol{\nu}_\infty + \sum_{j=1}^{N}\boldsymbol{\nu}_{ji} G_j\right) \times \boldsymbol{\xi}_i\right| G_i - C_{\ell_i}(\alpha_i) = 0 \tag{B.18}$$

with

$$\nu_\infty \equiv \frac{\mathbf{V}_\infty}{V_\infty} \quad \text{(B.19)} \qquad G_i \equiv \frac{\Gamma_i}{\overline{c}_i V_\infty} \quad \text{(B.20)} \qquad \nu_\infty \equiv \frac{\mathbf{V}_\infty}{V_\infty} \quad \text{(B.21)}$$

On the other hand, Weissinger places the control points at the third quarter chordwise position and determines the circulation of each horseshoe vortex by solving for the non-penetration condition at these points:

$$w_{ij}\Gamma_i = -V_{n_i} \tag{B.22}$$

Therefore, this method does not require knowing any local aerodynamic properties beforehand like Phillips' method did.

Despite taking advantage of computational power for the calculations of the non-linear system, it has been shown that Philips' approach is not able to accurately predict lift and suffers from convergence problems, where a higher spanwise discretization level doesn't result in more precise results. In his publication, he also suggests that using a curved line representation of the local aerodynamic centers, which has a more noticeable offset from the quarter chord line near the root and tips, could improve the results.

More recent research [79] demonstrates analytically that this violates the requirement of zero-concavity for a finite induced velocity and proposed, instead, the formulation of a conditional local concavity for the bound vortex and jointed trailing vortices, with a finite portion perpendicular to the local bound vortex and another portion aligned with the local freestream. This formulation, in addition to some local aerodynamic coefficient corrections of thin airfoil theory due to sweep effects, results in a better convergence behavior of the numerical model with more accurate results, but may be sensitive to the jointed trailing vortices lengths.

The high computational speed of vortex lattice methods, which give reasonably accurate results for conceptual design phases, makes them desirable to use and some attempts have been made to extend their validity to operating conditions close to stall, with the most common approach being a coupling of the VLM with 2D sectional aerodynamic polars that take into account boundary layer effects or even coupling with 2.5D polars, which have been corrected for the spanwise flow due to sweep [80]. Others use empirical corrections, such as [81], to try to estimate the region of the wing with detached flow and determine new values for the circulation distribution.

B.3. Modeling of Propeller-Wing Interactions

Considering that there isn't an established consensus on what the limits of the effects of propeller-wing interactions are, researchers have been trying to develop low order models to quickly investigate their impact on aircraft performance. However, there is a limited amount of available experimental data obtained for a wide range of operating conditions, which also prevents the validation of these methods more extensively.

One research paper [82], uses blade element momentum theory to determine the propeller performance and the blade section aerodynamic characteristics are obtained through RFOIL, which includes the centrifugal effects of the flow on the results. From the shed vorticity by the propeller blades, the time-averaged slipstream induced velocities are calculated by considering a continuous distribution of axial vorticity and the tangential vorticity in a slipstream tube with constant radius that is discretized in the radial and azimuthal directions, instead of the more realistic helicoidal vortex sheet.

The wing is modelled with the Weissinger VLM and, to account for the effect of the increase in axial velocity in the 2D sections engulfed by the propeller slipstream, a circulation correction factor is calculated using the method of images for the finite height small jets that compose the slipstream axial velocity profile. The effect of the propeller swirl component on this 2D correction is only included in the velocity magnitude normal to the camberline at the control point when solving the no-penetration condition, for lack of a better alternative. A similar correction is done in the 3D space to account for the different jets of increasing radius used to describe the 3D axial velocity profile.

By solving the no-penetration condition at each control point, the circulation distribution is determined and the lift and induced drag are calculated, the latter recurring to a Trefftz plane analysis. The method was validated against CFD results of a wing with a tip mounted propeller operating at $T_C = 0.045$, which showed an excellent similarity between the lift distribution data points and demonstrated that, without the corrections applied, local lift values were overpredicted by up to 25%.

With a similar method, but without any corrections applied, the wing can also be modelled with Weissinger VLM and the propeller performance can be modelled with blade performance theory, a modified version of the blade element momentum theory that calculates both the induced velocities in the propeller plane and in the slipstream, for a given thrust value [83]. In this case, the slipstream is modelled using a vortex ring method and its contraction is also taken into account. The model was validated against CFD data of a NACA 0012 wing with 3 propellers and captured the lift distribution shape well, but underpredicted the lift in the regions with a downgoing propeller blade rotation, which was attributed to the inviscid assumption of the method and doesn't have a turbulence model like the CFD simulations did.

B.4. Numerical Model

With the goal of identifying a numerical model capable of estimating the performance of different aircraft, and given the accurate results obtained in [82], the tool described in this paper was subject to further validation with a different test case. Since the goal is to study flight conditions at high angles of attack, with propellers operating at high thrust settings, a viscous correction would be needed to capture the stall angle and the maximum lift coefficient, which are critical at low speed conditions.

Therefore, the geometry of the experimental setup presented in [84] was reproduced to be used as an input to the tool.

With the purpose of studying the effect of propeller-wing interactions, wind tunnel tests were performed on a a straight, untapered wing with a single-slotted flap with a TUD-XPROP-S propeller installed ahead of the leading edge of the wing root. There are two pressure taps placed on each side of the propeller, inside the slipstream region and the tests were conducted for a freestream velocity of 30 m/s and propeller advance ratios of $J = 0.8$ and $J = 1.0$, which correspond to high thrust coefficients.

The comparison of results between the numerical model and the experimental results are show in Figure B.4a and Figure B.4b.

In both figures, the trends are the same: while both the clean wing results and the upgoing blade side values of lift coefficient have a good correlation in the linear regime at lower angles of attack, the tool underpredicts the values of local lift coefficient in the downgoing blade side. This behaviour is consistent with what was found in [83].

This will have a strong impact in the total wing lift coefficient calculated by the tool, which will be lower than in real conditions and have a lower linear slope. Without a good match between the numerical model's results for the lift coefficient linear regime, it is not possible to confidently make an observation and derive a formula to apply a correction to the curve slope at high angles of attack that may apply to different flow conditions.

One can conclude that this tool is not adequate for studying low speed aerodynamics of blown-lift wings and, so, another numerical model was chosen to serve as the base for the analysis in this project.

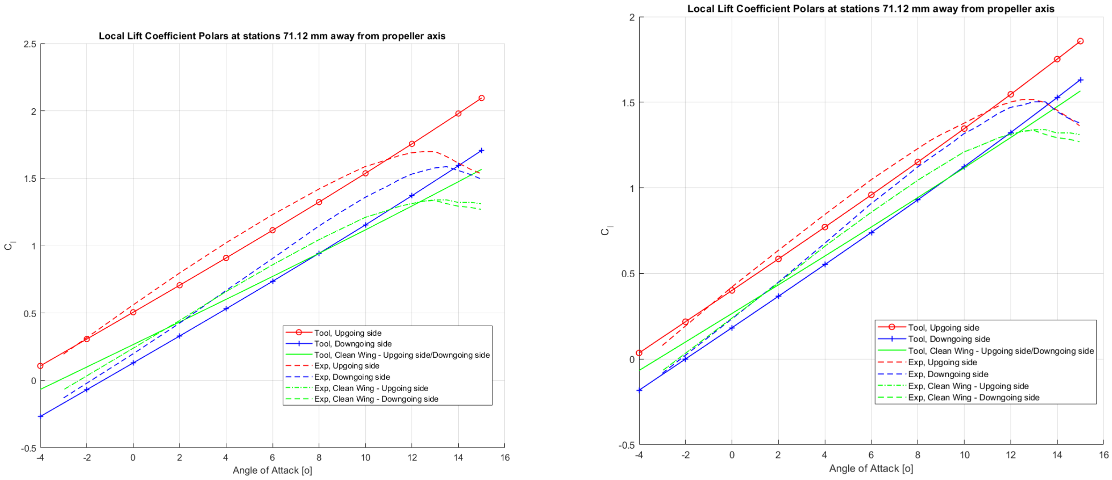

a) $J = 0.8$

b) $J = 1.0$

Figure B.4: Comparison of lift coefficient at the pressure taps location versus angle of attack for different propeller advance ratios.

References

[1] A. M. Stoll, J. Bevirt, M. D. Moore, et al. *Drag Reduction Through Distributed Electric Propulsion*. 2014. DOI: `10.2514/6.2014-2851`.

[2] R. M. Erhard, M. A. Clarke, and J. J. Alonso. “A Low-Cost Aero-Propulsive Analysis of Distributed Electric Propulsion Aircraft”. In: *AIAA Scitech 2021 Forum* (Jan. 2021). DOI: `10.2514/6.2021-1200`.

[3] C. Courtin, A. Mahseredjian, A. J. Dewald, et al. “A Performance Comparison of eSTOL and eVTOL Aircraft”. In: *AIAA AVIATION 2021 FORUM* (2021). DOI: `10.2514/6.2021-3220`.

[4] M. Schollenberger, B. Kirsch, T. Lutz, et al. “Aerodynamic interactions between distributed propellers and the wing of an electric commuter aircraft at cruise conditions”. In: *CEAS Aeronautical Journal* 15 (2024), pp. 255–267. DOI: `10.1007/s13272-023-00706-6`.

[5] R. de Vries, N. van Arnhem, F. Avallone, et al. “Experimental Investigation of Over-the-Wing Propeller–Boundary-Layer Interaction”. In: *AIAA Journal* 59.6 (2021), pp. 2169–2182. DOI: `10.2514/1.J059770`.

[6] J. S. Gray and J. R. R. A. Martins. “Coupled aeropropulsive design optimisation of a boundary-layer ingestion propulsor”. In: *The Aeronautical Journal* 123 (2019), pp. 121–137. DOI: `10.1017/aer.2018.120`.

[7] K. A. Deere, J. K. Viken, S. Viken, et al. “Computational Analysis of a Wing Designed for the X-57 Distributed Electric Propulsion Aircraft”. In: *35th AIAA Applied Aerodynamics Conference* (June 2017). DOI: `10.2514/6.2017-3923`.

[8] M. A. Gallani, L. C. S. Góes, and L. A. R. Nerosky. “Implementation of Distributed Electric Propulsion on a General Aviation Aircraft”. In: *32nd ICAS Congress* (Sept. 2021). URL: `https://www.icas.org/icas_archive/ICAS2020/data/papers/ICAS2020_1025_paper.pdf`.

[9] A. D. Marco, E. Duke, and J. Berndt. “A General Solution to the Aircraft Trim Problem”. In: *AIAA Modeling and Simulation Technologies Conference and Exhibit*. DOI: `10.2514/6.2007-6703`.

[10] C. Varriale and M. Voskuijl. “A trim problem formulation for maximum control authority using the Attainable Moment Set geometry”. In: *CEAS Aeronautical Journal* 13.1 (Nov. 2021), pp. 251–266. ISSN: 1869-5590. DOI: `10.1007/s13272-021-00560-4`.

[11] T. Woldhuis, S. Asaro, and X. Wang. “Online Data-Driven Optimization of Aerodynamic Performance for an Unconventional Morphing Aircraft”. In: *AIAA SCITECH 2025 Forum* (Jan. 2025). DOI: `10.2514/6.2025-2804`.

[12] C. E. D. Riboldi, S. Cacciola, and L. Ceffa. “Studying and Optimizing the Take-Off Performance of Three-Surface Aircraft”. In: *Aerospace* 9.3 (2022). ISSN: 2226-4310. DOI: `10.3390/aerospace9030139`.

[13] B. Moulton, C. Bolander, and D. F. Hunsaker. “Evaluation of Stability and Controllability of the Multiple Trim Solutions for a Bio-Inspired Rotating Empennage Fighter Aircraft”. In: *AIAA SCITECH 2025 Forum* (Jan. 2025). DOI: `10.2514/6.2025-0662`.

[14] D. Keller. “Numerical study on lift augmentation via distributed propulsion for a propeller-driven regional transport aircraft in landing configuration”. In: *CEAS Aeronautical Journal* (2025). DOI: `10.1007/s13272-025-00863-w`.

[15] D. Planas, C. Döll, and P. Pastor. “Handling Qualities of a Distributed Electric Propulsion Aircraft”. In: *International Council of the Aeronautical Sciences* (2022). URL: `https://hal.science/hal-03980312v1`.

[16] D. Planas, C. Döll, P. Pastor, et al. "Design optimization for improved HQ and performance of a DEP aircraft". In: *AIAA AVIATION 2023 Forum* (2023). DOI: `10.2514/6.2023-4049`.

[17] UNIFIER19 Consortium. *D2.2 Final Concurrent Design Report*. Deliverable. UNIFIER19, 2021. URL: `https://unifier19.eu/www.unifier19.eu/wp-content/uploads/2021/07/D2.2_Final_concurrent_design_report_Open.pdf` (visited on 01/07/2025).

[18] UNIFIER19 Consortium. *D3.3.: Conceptual design report including LCA - open*. Deliverable. UNIFIER19, 2022. DOI: `10.3030/864901`. (Visited on 01/07/2025).

[19] L. Trainelli, C. E. Riboldi, A. Rolando, et al. "Methodologies for the initial design studies of an innovative community-friendly miniliner". In: *IOP Conference Series: Materials Science and Engineering* 1024.1 (Jan. 2021), p. 012109. ISSN: 1757-899X. DOI: `10.1088/1757-899x/1024/1/012109`.

[20] D. Meade. *Wind On for 50 Years*. NASA Langley Research Center. Dec. 2020. URL: `https://www.nasa.gov/aeronautics/wind-on-for-50-years/`.

[21] S. B. Anderson. *Historical Overview of V/STOL Aircraft Technology*. Technical Memorandum NASA-TM-81280. NASA, Mar. 1981. URL: `https://ntrs.nasa.gov/api/citations/19810010574/downloads/19810010574.pdf`.

[22] F. May and C. A. Widdison. *STOL High-Lift Design Study Volume I. State-of-the-Art Review of STOL Aerodynamic Technology*. The Boeing Company. 1971. URL: `https://apps.dtic.mil/sti/tr/pdf/AD0724185.pdf`.

[23] T. Dansby, W. C. J. Garrard, D. Ryle, et al. *V/stol development of the c-130 hercules*. General Aviation Aircraft Design and Operations Meeting. 1964. URL: `https://doi.org/10.2514/6.1964-184`.

[24] T. S. H. Blair. *Lockheed C-130 Hercules*. 2014. URL: `https://pt.wikipedia.org/wiki/Lockheed_C-130_Hercules`.

[25] H. C. Quigley, R. C. Innis, and C. A. Holzhauser. *A Flight Investigation of the Performance, Handling Qualities, and Operational Characteristics of a Deflected Slipstream STOL Transport Airplane Having Four Interconnected Propellers*. NASA Ames Research Center. 1964. URL: `https://ntrs.nasa.gov/api/citations/19640007812/downloads/19640007812.pdf`.

[26] D. S. Miller. *Report on the accident to Fokker F27-500, G-BNCY at Guernsey Airport, Channel Islands on 7 December 1997*. Department of the Environment, Transport and the Regions - Air Accidents Investigation Branch. 1999. URL: `https://assets.publishing.service.gov.uk/media/5422f96be5274a13140006fb/4-99_G-BNCY.pdf`.

[27] S. Williams. *Breguet 941S - France - Air Force*. 2002. URL: `https://www.airliners.net/photo/France-Air-Force/Breguet-941S/247380`.

[28] C. Lubert. "On Some Recent Applications of the Coanda Effect to Acoustics". In: *Proceedings of Meetings on Acoustics* 11.1 (Feb. 2012), p. 040006. ISSN: 1939-800X. DOI: `10.1121/1.3694201`.

[29] C. B. Courtin. *Performance, Stability and Control of Electric Short Takeoff and Landing Aircraft*. MIT Massachusetts Institute of Technology. 2024. URL: `https://dspace.mit.edu/handle/1721.1/155476`.

[30] A. E. P. III, J. Joseph L. Johnson, and R. J. Margason. *Summary of Low-Speed Aerodynamic Characteristics of Upper-Surface-Blown Jet-Flap Configurations*. NASA. 1976. URL: `https://ntrs.nasa.gov/api/citations/19780016107/downloads/19780016107.pdf`.

[31] A. E. Phelps III and C. C. Smith Jr. *Wind-Tunnel Investigation of an Upper Surface BLown Jet-Flap Powered-Lift Configuration*. NASA Langley Research Center. 1973. URL: `https://ntrs.nasa.gov/api/citations/19740003719/downloads/19740003719.pdf`.

[32] E. R. Heald. *External Blowing Flap Technology on the USAF McDonnell Douglas YC-15*. Tech. rep. Douglas Aircraft Company, McDonnell Douglas Corporation, 1973. DOI: `10.4271/730915`.

[33] R. K. Saxer. *Buying the C-17 A Case Study*. National Defense University. 1995. URL: `https://apps.dtic.mil/sti/tr/pdf/ADA294085.pdf`.

[34] R. K. Heffley, R. L. Stapleford, and R. C. Rumold. *Airworthiness Criteria Development for Powered-Lift Aircraft - A Program Summary*. Systems Technology, Inc. 1977. URL: `https://ntrs.nasa.gov/citations/19770016153`.

[35] C. Pornet. *Conceptual Design Methods for Sizing and Performance of Hybrid-Electric Transport Aircraft*. PhD Dissertation, Technical University of Munich. 2018. URL: `https://mediatum.ub.tum.de/doc/1399547/1399547.pdf`.

[36] M. Hepperle. "Electric Flight - Potential and Limitations". In: *Energy Efficient Technologies and Concepts of Operation*. Oct. 2012. URL: `https://elib.dlr.de/78726/`.

[37] Electra.Aero. *Electra's Hybrid-Electric Test Aircraft Achieves First Ultra-Short eSTOL Takeoff and Landing in Piloted Test Flights*. 2024. URL: `https://www.electra.aero/news/electras-test-aircraft-achieves-first-ultra-short-estol-flights`.

[38] M. A. Frederick, M. S. Smith, S. Y. Yoo, et al. *Development of the X-57 Aerodynamic Database*. NASA Armstrong Flight Research Center. 2025. URL: `https://ntrs.nasa.gov/citations/20250001715`.

[39] C. D. Jean Hermetz Michael Ridel. "Distributed electric propulsion for small business aircraft a concept-plane for key-technologies investigations". In: *ICAS 2016* (2016). URL: `https://hal.science/hal-01408988v1`.

[40] P. Schmollgruber, C. Döll, J. Hermetz, et al. "Multidisciplinary Exploration of DRAGON: an ONERA Hybrid Electric Distributed Propulsion Concept". In: *AIAA Scitech 2019* (2019). URL: `https://hal.science/hal-02068597/file/DTIS19036.1552317536_preprint.pdf`.

[41] Electra. *Electra EL-2 Goldfinch*. Dec. 2025. URL: `https://en.wikipedia.org/wiki/Electra_EL-2_Goldfinch`.

[42] ONERA. *How can we reduce fuel consumption? Dragon*. URL: `https://www.onera.fr/en/news/how-can-we-reduce-fuel-consumption%3F-dragon`.

[43] T. C. A. Stokkermans. *Aerodynamics of Propellers in Interaction Dominated Flowfields: An Application to Novel Aerospace Vehicles*. Delft University of Technology. 2020. DOI: `10.4233/uuid:46178824-bb80-4247-83f1-dc8a9ca7d8e3`.

[44] L. Veldhuis. *Propeller Wing Aerodynamic Interference*. Delft University of Technology. 2005. URL: `https://repository.tudelft.nl/record/uuid:8ffbde9c-b483-40de-90e0-97095202fbe3`.

[45] S. Corcione, V. Cusati, D. Ciliberti, et al. "Experimental Assessment of Aero-Propulsive Effects on a Large Turboprop Aircraft with Rear-Engine Installation". In: *Aerospace Journal* 10.1 (2023), p. 85. DOI: `10.3390/aerospace10010085`.

[46] R. de Vries, T. Sinnige, and L. L. M. Veldhuis. "Aerodynamic Performance and Interaction Effects of an Over-The-Wing Distributed-Propeller System in Cruise Conditions". In: *34th ICAS Congress* (Sept. 2024). URL: `https://www.icas.org/icas_archive/icas2024/data/papers/icas2024_0632_paper.pdf`.

[47] J. Goyal, T. Sinnige, F. Avallone, et al. "Benchmarking of Aerodynamic Models for Isolated Propellers Operating at Positive and Negative Thrust". In: *AIAA Journal* 62.10 (2024), pp. 3758–3775. DOI: `10.2514/1.J064093`.

[48] L. S. Diehl and J. G. Coelho. "Assessment of the effectiveness of stall delay and tip loss corrections for the simulation of small propeller performance with Virtual Blade Model". In: *European Journal of Mechanics - B/Fluids* 105 (2024), pp. 34–43. ISSN: 0997-7546. DOI: `10.1016/j.euromechflu.2023.12.013`.

[49] G. R. Pirrung and M. P. van der Laan. "A simple improvement of a tip loss model for actuator disc and actuator line simulations". In: *Wind Energy Science Discussions* 2018 (2018), pp. 1–13. DOI: `10.5194/wes-2018-59`.

[50] Y. Leng, H. Yoo, T. Jardin, et al. “Aerodynamic Modeling of Propeller Forces and Moments at High Angle of Incidence”. In: *AIAA Scitech 2019 Forum*. AIAA Scitech 2019 Forum. San Diego, United States: AIAA, Jan. 2019. DOI: `10.2514/6.2019-1332`.

[51] R. Nederlof, D. Ragni, and T. Sinnige. *Experimental Investigation of the Aerodynamic Performance of a Propeller at Positive and Negative Thrust and Power*. AIAA Aviation 2022. 2022. DOI: `10.2514/6.2022-3893`.

[52] R. J. Jeracki and G. A. Mitchell. *Low and High Speed Propellers for General Aviation - Performance Potential and Recent Wind Tunnel Test Results*. NASA Lewis Research Center. 1981. URL: `https://ntrs.nasa.gov/citations/19810012499`.

[53] W. S. Gearhart. *Efficiency Improved Turboprop*. Pennsylvania State University. 1983. DOI: `10.2514/6.1983-59`.

[54] D. Biermann and E. P. Hartman. *The Effect of Compressibility on Eight Full-Scale Propellers Operating in the Take-Off and Climbing Range*. National Advisory Committee For Aeronautics. 1942. URL: `https://ntrs.nasa.gov/citations/19930091714`.

[55] C. J. Miller. *Euler Analysis of a Swirl Recovery Vane Design for Use With an Advanced Single-Rotation Propfan*. NASA Lewis Research Center. 1988. URL: `https://ntrs.nasa.gov/citations/19880020387`.

[56] L. Veldhuis, T. Stokkermans, T. Sinnige, et al. *Analysis of swirl recovery vanes for increased propulsive efficiency in tractor propeller aircraft*. 30th Congress ICAS 2016. 2016. URL: `https://www.icas.org/icas_archive/ICAS2016/data/papers/2016_0060_paper.pdf`.

[57] A. Pacilli. *Computational Fluid Dynamics Study of and Advance High-Speed NASA Propeller*. Master Thesis, Università Degli Studi Di Padova - Dipartimento di Ingegneria Industriale DII. 2023. URL: `https://thesis.unipd.it/handle/20.500.12608/62225`.

[58] A. Zanotti, L. Menini, A. Savino, et al. “Experimental investigation of wing-propeller aerodynamic interaction in eVTOL configurations”. In: *Aerospace Science and Technology* 152 (2024), p. 109348. ISSN: 1270-9638. DOI: `10.1016/j.ast.2024.109348`.

[59] C. Moreira, N. Herzog, and C. Breitsamter. “Wind Tunnel Investigation of Transient Propeller Loads for Non-Axial Inflow Conditions”. In: *Aerospace* 11.4 (2024). ISSN: 2226-4310. DOI: `10.3390/aerospace11040274`.

[60] T. Sinnige and B. Della Corte. *Aerodynamic Performance of a Tip-Mounted Propeller-Wing System at Positive and Negative Thrust*. AIAA Aviation Forum and ASCEND 2024. 2024. DOI: `10.2514/6.2024-3520`.

[61] T. Long. *An Experimental Investigation of Blown-Flap Airfoils*. Massachusetts Institute of Technology. 2021. URL: `https://dspace.mit.edu/handle/1721.1/139918`.

[62] D. Keller. “Aerodynamic Investigation of the High-Lift Performance of a Propeller-Driven Regional Transport Aircraft with Distributed Propulsion”. In: *Journal of Physics: Conference Series* 2526 (2023), p. 012007. DOI: `10.1088/1742-6596/2526/1/012007`.

[63] R. Vos and S. Farokhi. *Introduction to Transonic Aerodynamics*. Vol. Fluid Mechanics and Its Applications. Springer, 2015. ISBN: 978-94-017-9746-7. DOI: `10.1007/978-94-017-9747-4`.

[64] T. A. Harris. *Reduction of Hinge Moments of Airplane Control Surfaces By Tabs*. Tech. rep. National Advisory Committee for Aeronautics, 1935. URL: `https://ntrs.nasa.gov/api/citations/19930091601/downloads/19930091601.pdf`.

[65] D. D. Bueno and E. H. Dowell. “Revisiting the Fundamentals of Control Surface Reversal Including Nonlinear Effects”. In: *Journal of Aircraft* 57.6 (2020), pp. 1212–1219. DOI: `10.2514/1.C035885`.

[66] B. Chudoba and M. Cook. “Trim Equations of Motion for Aircraft Design: Steady State Straight Line Flight”. In: AIAA Atmospheric Flight Mechanics Conference and Exhibit, 2003. DOI: `10.2514/6.2003-5691`.

[67] D. C. Garmendia and D. N. Mavris. “Alternative Trim Analysis Formulations for Vehicles with Redundant Multi-Axis Control Surfaces”. In: *Journal of Aircraft* 53.1 (2016), pp. 60–72. DOI: `10.2514/1.C033184`.

[68] A. R. Moretti. *Mid-Fidelity Modeling of the Aero-Propulsive Interaction for the Initial Design of Distributed Propulsion Aircraft*. Politecnico di Milano. 2022. URL: `https://www.politesi.polimi.it/handle/10589/191677`.

[69] J. S. Soikkeli. *Unifier C7A-HARW Flight Dynamics Simulator on Github*. 2024. URL: `https://github.com/soikkelij/unifier_fds`.

[70] G. A. M. van Kuik. “The Actuator Disc Concept”. In: *Handbook of Wind Energy Aerodynamics*. Springer, 2022, pp. 47–94. ISBN: 9783030313067. DOI: `10.1007/978-3-030-31307-4\_2`.

[71] T. Sinnige. *Propeller slipstream characteristics*. Lecture slides, AE4135 Rotor/Wake Aerodynamics, TU Delft. 2024. URL: `https://brightspace.tudelft.nl/d2l/le/content/593401/viewContent/3263349/View`.

[72] J. Ledoux, S. Riffo, and J. Salomon. “Analysis of the Blade Element Momentum Theory”. In: *SIAM Journal on Applied Mathematics* 81.6 (Dec. 2021), pp. 2596–2621. DOI: `10.1137/20M133542X`.

[73] M. D. Patterson. *Conceptual Design of High-Lift Propeller Systems for Small Electric Aircraft*. Georgia Institute of Technology. 2016. URL: `https://repository.gatech.edu/entities/publication/58067d91-5837-4a2f-a461-370817609ade`.

[74] T. Wang, W. Zhong, Y. Qian, et al. “Unsteady Blade Element Momentum Method”. In: *Wind Turbine Aerodynamic Performance Calculation*. Singapore: Springer Nature Singapore, 2023, pp. 99–112. ISBN: 978-981-99-3509-3. DOI: `10.1007/978-981-99-3509-3_6`.

[75] L. Prandtl. *Applications of Modern Hydrodynamics to Aeronautics*. Tech. rep. National Advisory Committee for Aeronautics, 1923. URL: `https://ntrs.nasa.gov/api/citations/19930091180/downloads/19930091180.pdf`.

[76] T. Melin. “Using Internet interactions in developing vortex lattice software for conceptual design”. Licentiate Thesis. KTH Royal Institute of Technology, Dec. 2003. URL: `https://www.researchgate.net/publication/260198739_Using_Internet_interactions_in_developing_vortex_lattice_software_for_conceptual_design`.

[77] J. Weissinger. *The Lift Distribution of Swept-Back Wings*. Tech. rep. National Advisory Committee for Aeronautics, 1947. URL: `https://ntrs.nasa.gov/api/citations/20030064148/downloads/20030064148.pdf`.

[78] W. F. Phillips and D. O. Snyder. “Modern Adaptation of Prandtl’s Classic Lifting-Line Theory”. In: *Journal of Aircraft* 37.4 (2000), pp. 662–670. DOI: `10.2514/2.2649`.

[79] J. T. Reid and D. F. Hunsaker. “A General Approach to Lifting-Line Theory, Applied to Wings with Sweep”. In: *AIAA Scitech 2020 Forum*. 2020. DOI: `10.2514/6.2020-1287`.

[80] H. Goitia and R. Llamas. “Nonlinear vortex lattice method for stall prediction”. In: *MATEC Web Conf.* 304 (2019), p. 02006. DOI: `10.1051/matecconf/201930402006`.

[81] C. R. dos Santos and F. D. Marques. “Lift Prediction Including Stall, Using Vortex Lattice Method with Kirchhoff-Based Correction”. In: *Journal of Aircraft* 55.2 (2018), pp. 887–891. DOI: `10.2514/1.C034451`.

[82] R. Nederlof, J. Goyal, T. Sinnige, et al. “Fast Numerical Modeling of Propeller–Wing Aerodynamic Interactions”. In: *AIAA Journal* 63.6 (2025), pp. 2499–2519. DOI: `10.2514/1.J064764`.

[83] B. K. D’Angelo, H. K. Balachandran, and A. Gopalarathnam. “Low-order and Computational Modeling of Propeller-Wing Interaction”. In: AIAA AVIATION 2022 Forum, 2022. DOI: `10.2514/6.2022-3686`.

[84] R. Duivenvoorden. *Aerodynamic Phenomena of Propeller-Wing-Flap Interaction*. TU Delft. 2025. URL: `https://repository.tudelft.nl/record/uuid:1a705c0a-b0aa-4ddd-a350-8c663cf2fdb0`.